

# POLITECNICO DI TORINO



Department of Electronics and Telecommunications  
Master Degree in Electronic Engineering  
Thesis in Electronic Micro and Nanosystems

---

## INVESTIGATION OF CMOS FRONT-END ARCHITECTURES FOR C<sub>60</sub> SINGLE-MOLECULE SENSOR

---

**Supervisors:**

Prof. Mariagrazia GRAZIANO  
Prof. Gianluca PICCININI  
Doct. Fabrizio MO

**Candidate:**

Gabriele BONAVOGLIA

April 2023



# Abstract

Starting from the twentieth century, climate change has progressively become the most dangerous threat to life on Earth. Some of its effects, like air pollution, have led to the development of devices, called gas sensors, that are able to monitor the presence of substances that could be harmful or toxic to human health. From a technological and electrical point of view, a constraint about sensors is their difficult compatibility with CMOS electronic systems which they interact with. Since full integration on CMOS circuits is complicated to achieve, the best compromise consists in designing circuits that have the task of properly conditioning the sensor and converting the detection information into electrical signals. In this manner, one can easily interface the sensor to instruments that will acquire the generated signals and recover the response of the sensor to gas exposure.

In this context, the aim of this thesis is to implement a CMOS interfacing front-end for a molecular gas sensor based on fullerene (in particular  $C_{60}$ ), used as a sensing element, connected to two gold (Au) electrodes. Operating in amperometric mode, the sensor is exposed to a gas whose presence modulates the current that flows through the Au- $C_{60}$ -Au structure with respect to the case in which no gas is present. After electrical simulations of its behavioural model, the  $C_{60}$  sensor has shown the good capability of being selective in the detection of gases like nitric oxide (NO) and nitrogen dioxide ( $NO_2$ ). In order to distinguish between the multitude of gases and their different configurations (molecule orientations etc.), a signature is needed for their acknowledgement. In particular, frequency is a quantity that can be acquired (for example by means of a micro-controller) and measured with good accuracy. For this reason, I have chosen a current-to-frequency converter that can provide a reliable indication about the gas that interacts with the sensor.

In Chapter 1, I will explore the state-of-the-art of gas sensing devices and their interfacing circuitry. In particular, I will highlight the main technologies and applications in which they operate and the various hardware architectures for analog front-ends and gas recognition circuits.

In Chapter 2, I will describe the features and sensing capabilities of  $C_{60}$ -based sensor in order to identify the requirements for the implementation of the analog front-end. According to them, the architecture of the integrated circuit will be

derived and shown by means of block schemes whose characteristics will be briefly described.

In Chapter 3, I will go on with the detailed implementation of each stage of the analog front-end; I will focus on the design choices I have taken to adapt the CMOS architecture to the requirements of the molecular sensor.

In Chapter 4, I will test the electrical behaviour of the circuit by means of simulations that have the purpose of validating the final results.

In Chapter 5, the conclusions of this thesis work will be drawn by discussing final outcomes, showing that the implemented circuit is promising to act as a conditioning circuit for the gold-C<sub>60</sub>-gold gas sensor. In the end, I will provide a brief perspective on future developments.



# Table of Contents

<b>List of Figures</b>	VII
<b>List of Tables</b>	IX
<b>Acronyms</b>	XI
<b>1 Gas sensors and CMOS interfacing circuits: state-of-the-art</b>	<b>1</b>
1.1 Gas sensors' technologies . . . . .	3
1.1.1 Chemiresistive gas sensors . . . . .	4
1.1.2 Electrochemical gas sensors . . . . .	6
1.2 CMOS interfacing circuits for amperometric sensors . . . . .	7
1.2.1 Review of interfacing analog front-ends . . . . .	8
1.2.2 Gas recognition systems . . . . .	14
<b>2 C<sub>60</sub> gas sensor: characteristics and requirements for interfacing circuit</b>	<b>19</b>
2.1 Molecular electronic sensors . . . . .	20
2.2 C <sub>60</sub> -based molecular gas sensor . . . . .	22
2.2.1 Device structure . . . . .	23
2.2.2 Mathematical model of conductivity in Au-C <sub>60</sub> -Au system . . . . .	23
2.2.3 Sensing capabilities . . . . .	26
2.3 C <sub>60</sub> -sensor's requirements and front-end architecture derivation . . . . .	32
2.3.1 Acquiring current from the sensor . . . . .	33
2.3.2 Converting analog quantity in digital domain . . . . .	34
2.3.3 Final architecture of the analog front-end . . . . .	35
<b>3 Characterization of the analog front-end</b>	<b>38</b>
3.1 Readout circuit . . . . .	39
3.1.1 Current conveyor . . . . .	39
3.1.2 Current mirror . . . . .	41
3.1.3 Simulation of the readout circuit . . . . .	43

3.2	Current-to-frequency converter . . . . .	51
3.2.1	Simulation of current-to-frequency converter . . . . .	54
<b>4</b>	<b>Simulation and validation of final results</b>	<b>61</b>
4.1	Exposure to nitric oxide (NO) . . . . .	64
4.2	Exposure to nitrogen dioxide (NO <sub>2</sub> ) . . . . .	71
4.3	Sensitivity of the analog front-end . . . . .	74
4.3.1	Sensitivity with respect to $I_{DS}$ . . . . .	74
4.3.2	Sensitivity with respect to $V_{DS}$ . . . . .	78
<b>5</b>	<b>Conclusions and future works</b>	<b>82</b>
	<b>Bibliography</b>	<b>85</b>

# List of Figures

1.1	Concentration levels of typical gas in atmospheric air [2]. . . . .	2
1.2	Block diagram of readout circuit in [34]. . . . .	9
1.3	Top-level architecture of one channel in [36]. . . . .	10
1.4	Single-channel architecture in [37]. . . . .	11
1.5	Single channel architecture in [39]. . . . .	11
1.6	Single-channel architecture in [40]. . . . .	12
1.7	Front-end architecture in [42]. . . . .	15
1.8	Single-channel scheme in [44]. . . . .	15
1.9	Single-channel scheme in [45]. . . . .	16
2.1	Test bench for C <sub>60</sub> -sensor. . . . .	26
2.2	$I_{DS} - V_{DS}$ trans-characteristic of the C <sub>60</sub> -sensor (with no gas). . . . .	27
2.3	$I_{DS} - V_{DS}$ trans-characteristic of the C <sub>60</sub> -sensor (with NO, in different orientations). . . . .	29
2.4	Response of C <sub>60</sub> -sensor to butane (C <sub>4</sub> H <sub>10</sub> ). . . . .	30
2.5	Response of C <sub>60</sub> -sensor to methane (CH <sub>4</sub> ). . . . .	31
2.6	Response of C <sub>60</sub> -sensor to ammonia (NH <sub>3</sub> ). . . . .	31
2.7	Response of C <sub>60</sub> -sensor to nitric oxide (NO). . . . .	32
2.8	Response of C <sub>60</sub> -sensor to nitrogen dioxide (NO <sub>2</sub> ). . . . .	32
2.9	High-level architecture of gas recognition system for C <sub>60</sub> -sensor. . . . .	35
3.1	Block scheme of the readout circuit connected to the C <sub>60</sub> -sensor. . . . .	40
3.2	Current conveyor (implementation in Cadence Virtuoso). . . . .	40
3.3	Configurations of current mirrors. . . . .	41
3.4	Current mirror (implementation in Cadence Virtuoso). . . . .	43
3.5	Readout circuit (implementation in Cadence Virtuoso). . . . .	44
3.6	Voltages of the current conveyor for different values of $V_{CC}$ . . . . .	45
3.7	Currents in the readout circuit (for $W = 15 \mu\text{m}$ and $L = 1 \mu\text{m}$ ). . . . .	46
3.8	Output current $I_1$ for different values of $W$ . . . . .	47
3.9	Currents in the readout circuit (for $W = 1.5 \mu\text{m}$ and $L = 0.1 \mu\text{m}$ ). . . . .	48

3.10	Time evolution of sensor's control voltage $V_{CTRL}$ and of the currents $I_{DS}$ and $I_1$ . . . . .	50
3.11	Current-to-frequency converter. . . . .	52
3.12	Evolution in time of the quantities of interest in the i-to-f converter, with $C_{int} = 500$ fF and $t_d = 1$ ns. Voltages: $v_{cap}$ (blue), $V_{comp}$ (orange), $V_{spike}$ (yellow), $V_{spike,delayed}$ (violet). . . . .	56
3.13	Evolution in time of the quantities of interest in the i-to-f converter, with $C_{int} = 50$ fF and $t_d = 500$ ps. Voltages: $v_{cap}$ (blue), $V_{comp}$ (orange), $V_{spike}$ (yellow), $V_{spike,delayed}$ (violet). . . . .	58
4.1	Analog front-end for $C_{60}$ gas-sensor (implementation in Cadence Virtuoso). . . . .	62
4.2	Orientations of nitric oxide (NO) with respect to $C_{60}$ -sensor's channel axis. . . . .	65
4.3	Exposure to Ar and NO ("O down"). Time evolution of control voltage ( $V_{CTRL}$ ), current ( $I_{DS}$ ) and output frequency ( $f_{out}$ ). . . . .	66
4.4	Exposure to Ar and NO ("O down"). Voltage across the $C_{60}$ ( $V_{DS}$ ). . . . .	67
4.5	Exposure to Ar and NO ("O down"). Mirror current in input to the i-to-f converter ( $I_{mirr}$ ) and voltage across the integrating capacitor ( $v_{cap}$ ). . . . .	68
4.6	Orientations of nitrogen dioxide ( $NO_2$ ) with respect to $C_{60}$ -sensor's channel axis. . . . .	71
4.7	Interpolation of ( $I_{DS}, f_{out}$ ) ideal data, for NO exposure ( $V_{DS} = 1$ V). . . . .	74
4.8	Interpolation of ( $I_{DS}, f_{out}$ ) ideal data, for $NO_2$ exposure ( $V_{DS} = 1.7$ V). . . . .	75
4.9	Interpolation of ( $I_{DS}, f_{out}$ ) data from simulation, for NO exposure ( $V_{REF} = 1$ V). . . . .	75
4.10	Interpolation of ( $I_{DS}, f_{out}$ ) data from simulation, for $NO_2$ exposure ( $V_{REF} = 1.7$ V). . . . .	76
4.11	Corrected interpolation of ( $I_{DS}, f_{out}$ ) data from simulation, for $NO_2$ exposure ( $V_{REF} = 1.7$ V). . . . .	77
4.12	Interpolation of ( $V_{DS}, f_{out}$ ) data from simulation, for NO exposure ( $V_{REF} = 1$ V). . . . .	78
4.13	Interpolation of ( $V_{DS}, f_{out}$ ) data from simulation, for $NO_2$ exposure ( $V_{REF} = 1.7$ V). . . . .	79

# List of Tables

1.1	Comparison of state-of-the-art for current sensing AFEs. . . . .	13
1.2	Comparison of state-of-the-art for gas recognition circuits. . . . .	16
2.1	Encoding of gas targets detected by C <sub>60</sub> -sensor. . . . .	28
4.1	Fixed design parameters of the analog front-end. . . . .	63
4.2	Atmospheric gases: control voltages, input currents and output frequency values. . . . .	64
4.3	Nitric oxide (NO): control voltages, currents and output frequencies (for $V_{DS} = 1\text{ V}$ ). . . . .	64
4.4	Theoretical and simulation values of currents and frequencies, for exposure to NO (“O down”). . . . .	69
4.5	Theoretical and simulation values of currents and frequencies, for exposure to NO (“N down”). . . . .	70
4.6	Theoretical and simulation values of currents and frequencies, for exposure to NO (“flat”). . . . .	70
4.7	Nitrogen dioxide (NO <sub>2</sub> ): control voltages, input currents and output frequencies (for $V_{DS} = 1.7\text{ V}$ ). . . . .	71
4.8	Theoretical and simulation values of currents and frequencies, for exposure to NO <sub>2</sub> (“O down”). . . . .	72
4.9	Theoretical and simulation values of currents and frequencies, for exposure to NO <sub>2</sub> (“N down”). . . . .	73
4.10	Theoretical and simulation values of currents and frequencies, for exposure to NO <sub>2</sub> (“flat”). . . . .	73
4.11	Values of sensitivity of the analog front-end with respect to $I_{DS}$ . . .	77
4.12	Values of sensitivity of the analog front-end with respect to $V_{DS}$ . . .	80



# Acronyms

**CMOS** Complementary Metal-Oxide-Semiconductor

**MOS** Metal-Oxide-Semiconductor

**MOX** Metal-Oxide

**WE** Working Electrode

**CE** Counter Electrode

**RE** Reference Electrode

**PTFE** Polytetrafluoroethylene

**RTIL** Room Temperature Ionic Liquids

**AFE** Analog Front-End

**AGA** Automatic Gain Adjustment

**ADC** Analog-to-Digital Converter

**SCI** Switched-Capacitor Integrator

**DAC** Digital-to-Analog Converter

**CMFB** Common Feedback

**OTA** Operational Trans-conductance Amplifier

**IIR** Infinite Impulse Response

**PWM** Pulse-Width Modulation

**DR** Dynamic Range

**2D** 2-Dimensional

**SIPO** Serial-In Parallel-Output

**ITRS** International Technology Roadmap for Semiconductors

**IRDS** International Roadmap for Devices and Systems

**MES** Molecular Electronic Sensor

**VOC** Volatile Organic Compound

**molFET** Molecular Field-Effect Transistor

**FCC** Face-Centered Cubic

**0D** 0-Dimensional

**LUT** Look-Up Table

**EHT** Extended Hückel Theory

**NEGF** Non-Equilibrium Green's Function

**HDL** Hardware Description Language

**MOSFET** Metal-Oxide-Semiconductor Field-Effect Transistor



# Chapter 1

## Gas sensors and CMOS interfacing circuits: state-of-the-art

In the last decades, the continuous growth of industrial production and the indiscriminate use of fossil fuels are considered to be some of the climate change's causes. In particular, the higher concentration of greenhouse gases (such as carbon dioxide, methane etc.) in the atmosphere is believed to worsen global warming. Besides, the combination of these phenomena has a significantly negative impact on the quality of life since they concur to feed the air pollution issue on a local scale [1].

The multitude of gases in atmospheric air is depicted in Figure 1.1, in which their concentration has been measured according to different control standards.

For these reasons, there has been a strong development of innovative technologies for sensing the presence of gaseous compounds, especially the ones which are harmful or potentially toxic to human health. Over the years, devices - such as gas sensors and transducers - have been studied, fabricated and optimized in order to adapt their detecting capabilities to the challenges of numerous application fields. In fact, nowadays gas sensors have a huge diffusion that allows them to be used, for instance, in cars cabins, factories and households [2].

The information about the detection of gaseous chemical species requires to be acquired by proper instruments in order to be read and monitored by potential users. In this scenario, integrated electronic devices are useful to “translate” the information provided by a sensor into electrical signals (current, resistance, frequency etc.) that can be measured and analyzed. Nowadays, integrated electronics are mostly fabricated in Complementary Metal-Oxide-Semiconductor (CMOS) technology. Low power consumption, great noise tolerance, a wide operating voltage range

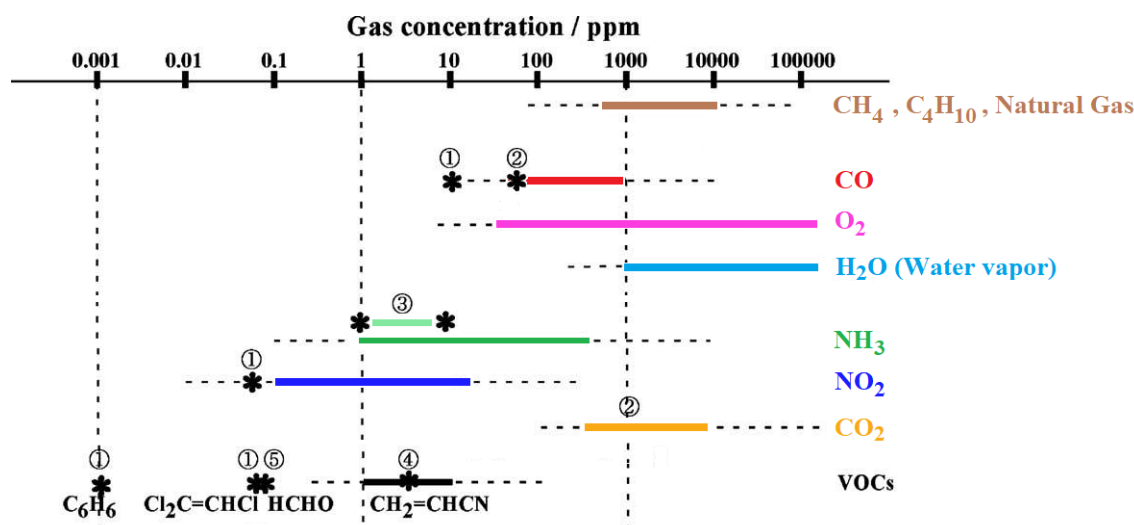


Figure 1.1: Concentration levels of typical gas in atmospheric air [2].

and a wide operating temperature range are key benefits of this technology. In addition, the intrinsic speed of MOS transistors is predicted to increase due to the scaling down of integrated circuit feature sizes in accordance with Moore's law (the number of transistors on a single chip doubles every 18 months) [3]. This means that with an increasing number of transistors, at fixed silicon area, the fabrication costs result to be optimized. As a result, CMOS technology has unquestionably emerged as one of the most promising and versatile technologies for integrated circuits [4]. Specifically for sensing applications, the main efforts have been focused on designing fully integrated detecting devices in CMOS technology in order to involve the sensor in the same CMOS fabrication process. Nevertheless, one of the most limiting problems of this approach is the fact that a sensor which is embedded in an integrated CMOS circuit increases the overall cost of the chip, restricting its commercial request. Then, to address the trade-off between integration and cost issues, the best solution is to design an effective interfacing circuit. This strategy is known as "More than Moore", i.e. the heterogeneous integration of devices in different technologies for the fulfilment of a multi-functional integrated circuit [5], [6]. In this way, sensors that refer to innovative technologies can be joined to standard CMOS chips. This choice allows both to reduce costs and to prevent the CMOS circuit from being affected by inherent effects in sensors (dependence on temperature and humidity, signal drift etc.) [7].

In this chapter, we will provide a brief overview of gas sensors' state-of-the-art in order to compare different technologies and highlight their advantages and drawbacks (Section 1.1). Secondly, we will focus on the incorporation of these devices

into CMOS interfacing circuitry. In particular, we will examine some literature examples of analog front-ends which have been designed and tested in other works (Section 1.2).

## 1.1 Gas sensors' technologies

A gas sensor can be defined as a device which is capable of detecting the presence of one or more chemical compounds in gaseous form, called targets, in a controlled volume [8]. Once the detection happens, a change in its physical or electrical properties occurs.

This type of device has to meet various requirements in order to be used for many or specific applications. The main characteristics of a gas sensor are the following [2]:

- *Sensitivity*: the capability of the device to sense one or more gaseous compounds. It has to be as large as possible to cover a wide range of gaseous species. This is an advantage from an economic point of view since the costs can be optimized for the fabrication of a single device.
- *Selectivity*: the ability to distinguish between different targets. To counterbalance the large sensitivity to many compounds, the sensor should have a high degree of selectivity in order to discriminate among the multitude of chemical species that can be sensed.
- *Reliability*: the quality of providing correct results under adverse conditions. A gas sensor is likely to face a large and long-time usage that could compromise its correct functioning. So, it has to be as reliable as possible, i.e. capable of enduring issues like ageing and fabrication tolerances over its lifetime.

In order to maximize each of the features described above, the choice of technology and the selection of proper sensing materials are essential for the design of a gas sensor. Two of the most significant types of these devices are highlighted below:

1. *Chemiresistive gas sensors* (Subsection 1.1.1): such devices have been developed mostly by exploiting semiconducting materials (for example  $\text{SnO}_2$ ) whose physical and chemical properties are suitable for gas detection, particularly their sensitivity to different external stimulus (e.g. temperature);
2. *Electrochemical gas sensors* (Subsection 1.1.2): in particular electrochemical cells that, differently from the previous ones, they make use of an electrolyte (in liquid or solid state) to trigger a redox reaction in presence of a gas.

In the following subsections, we will describe these kinds of gas sensors to examine their detection principles and to specify the applications they better fit.

### 1.1.1 Chemiresistive gas sensors

The detection's working principle of a chemiresistor gas sensor consists of a conductivity (then also resistance) change of the sensing layer. The materials that are commonly used are metal-oxide (MOX) semiconductors. The gas sensing mechanism of these devices can be summarised in three basic functions [9], [10]:

- *Receptor function*: capability of the MOX layer surface of “linking” with the target gas. At elevated temperature (typically 200 °C-500 °C), oxygen molecules adsorb onto the surface and ionize negatively (gaining electrons), thus forming an “electronic shell” around the core of sensing material particles that works as a receptor for the incoming targets.
- *Transducer function*: ability to convert the chemical interaction between the semiconducting surface and the target gas into a variation in conductance. When the sensing layer is exposed to the gas, starting a redox reaction, free electrons are injected into the semiconducting core and a depleted layer forms close to the sensor's exposed surface. As a consequence, the conductance increases (i.e. the resistance decreases) proportionally to the concentration of the analyte gas.
- *Utility function*: ease for the gas of passing through inner paths between oxide grains. The response of the sensor depends on the sensing material morphology, for example on the size of grains, the spacing between them and their agglomeration. The influence of these parameters on the effectiveness of the sensor depends on the specific material and case by case they can be tuned to have the best possible outcome.

In analytical terms, the response of a semiconductor gas sensor can be expressed by referring to the resistance value it assumes in presence of the gas ( $R_s$ ) and without being exposed to it ( $R_0$ ). Specifically, the response of the sensor to a target gas can be approximated by the following power law [11]:

$$\frac{R_s}{R_0} = aC^{-\gamma} \quad (1.1)$$

where  $C$  is the gas concentration. In addition, the scaling factor  $a$  and the exponent factor  $\gamma$  represent a specific feature of the gas which the sensor is exposed to. According to Equation 1.1, the resistance of the sensor decreases as the concentration of the target gas increases. This mathematical model is coherent with the physical description of the gas detection mechanism described above.

In literature, there are countless works that examine in depth the use of semiconductor oxides in chemiresistive gas sensors. Then, let us mention some of the most significant materials used in this kind of devices [9], [12]:

- *Tin dioxide* ( $\text{SnO}_2$ ): it is the most widely used semiconductor oxide in commercial gas detecting devices. Tin dioxide is an n-type semiconductor, i.e. electrons are the free charge carriers. So, when a reducing gas is detected (e.g.  $\text{CO}$ ,  $\text{NH}_3$ ,  $\text{CH}_4$  etc.), electrons tend to travel towards the target, thus increasing the conductivity (accumulation condition for the majority carriers). On the contrary, when an oxidizing gas approaches (e.g.  $\text{O}_2$ ,  $\text{O}_3$ ,  $\text{NO}_x$  etc.), the tin dioxide layer withstands a depletion of electrons that reduces its conductivity (depletion condition of majority carriers). Although it shows a good sensitivity for gases at low concentrations, tin dioxide has a lack of selectivity. Many works report that there are different ways to boost this property: for example, by optimizing the deposition technique in the fabrication process, with a focus on stoichiometry [13], the grain size and porosity of film [14] or the thickness of sensing layer [15].
- *Copper oxide* ( $\text{CuO}$ ): it is a p-type semiconductor, employed in sensing of gases like  $\text{NO}_2$  and  $\text{CO}$  [16]. Moreover, copper oxide can be joined to n-type semiconductors to increase the detecting capability of the gas sensor. An example of such heterogeneous materials is the use of  $\text{CuO}$  as a promoter for tin dioxide. Thanks to the electronic interaction that occurs between the two metal-oxides, a developed gas sensor resulted to be very sensitive to  $\text{H}_2\text{S}$  [17].
- *Zinc oxide* ( $\text{ZnO}$ ): it is the first metal-oxide to be exploited in gas sensing applications. In 1962 it was demonstrated that a  $\text{ZnO}$  film, at around  $400^\circ\text{C}$ , was capable of sensing gases like  $\text{CO}_2$ , propane and benzene [18]. More recent studies have highlighted that this material can be manipulated to form nanostructures (particles, wires, rods etc.) that enhance its gas detection capability thanks to an improved surface-to-volume ratio [19], [20].

These kinds of materials are widely used since they ensure advantages in terms of low costs and easy fabrication. On the contrary, metal-oxides present poor selectivity among the sensed gases which limits the performance of the sensor itself. To overcome this issue, a key factor for enhancing the effectiveness of these sensing materials is the temperature which has to be raised up to several hundreds of degrees Celsius. Moreover, high temperatures allow to “trigger” the redox reaction, leading to a variation in the sensor’s conductance. Nevertheless, if the temperature is not well controlled, it could lead to high power consumption. So, in order to locally increase the operating temperature, we could embed a microheater in correspondence of the gas sensor [7]. However, this solution is difficult to fulfil and further complicates the implementation of interfacing circuits (see Section 1.2).

### 1.1.2 Electrochemical gas sensors

An electrochemical gas sensor is defined as “a small device that, as the result of a chemical interaction or process between the analyte gas and the sensor device, transforms chemical or biochemical information of a quantitative or qualitative type into an analytically useful signal” [21].

Typically, such a device is formed by two or more electrodes that interact with an electrolyte<sup>1</sup>. Electrochemical gas sensors can convert the information that a gaseous chemical compound has been detected into different electrical quantities. Specifically, they can operate in the following modes [7], [23]:

- *Voltammetric*: the sensor is stimulated by an electric potential at the electrodes and a current is measured. In particular, it is proportional to the concentration of the gas of interest.
- *Amperometric*: it is a special case of voltammetric mode, for which the potential applied across the sensor remains constant. The measured current follows a function which is the combination of three equations: the first Fick's law, the ideal gas equation and Faraday's law.
- *Potentiometric*: when the gas exposure occurs, a redox chemical reaction occurs at the electrodes-electrolyte interfaces and results in a potential difference between the electrodes as the equilibrium is reached. This working principle is ruled by the Nernst equation.

The electrolyte of an electrochemical gas sensor can be either solid or liquid. The choice of its physical state is taken depending on the structure of the device and the application of use.

Usually, solid electrolytes are used since at high operating temperatures (greater than 300 °C) they are characterized by high conductivity and chemical reactions result to be faster [24]. One of the most used materials for a solid electrolyte is zirconia (ZrO<sub>2</sub>). In literature, there are many works in which zirconia is employed. For example, for detection of water vapour and carbon dioxide [25] and of nitrogen and sulfur oxides in environmental monitoring application [26], where sensors are required to operate in harsh conditions.

Another type of electrochemical sensor is represented by the so-called electrochemical cell. It is characterized by a liquid electrolyte (that can operate at room temperature) and its main operating mode is the amperometric one. This type of

---

<sup>1</sup> “Substance that conducts electric current as a result of a dissociation into positively and negatively charged particles called ions, which migrate toward and ordinarily are discharged at the negative and positive terminals (cathode and anode) of an electric circuit, respectively” [22].

sensor is employed in different applications. In particular, with electrodes made of carbon-based materials, they are suitable for biosensing applications [27]. An electrochemical cell can also act as a gas sensor. Its structure consists of three electrodes [28]:

- *Working electrode* (WE): it is the sensing electrode that must be sensitive to the analyte of interest. For gas sensing applications, it is made of gold (Au) or platinum (Pt), i.e. noble metals that show good stability to constant potentials. Its surface needs to be porous in order to allow the gas to spread onto a larger WE-electrolyte interface and so optimize the redox reaction.
- *Counter electrode* (CE): it is the electrode from which we get the measurement of the faradaic current resulting from the reaction. Usually, it is made of platinum (Pt).
- *Reference electrode* (RE): it has the task of maintaining the WE at a constant potential during the exposure of the gas analyte and the redox reaction. The material of the CE has to be reversible<sup>2</sup>: then, a silver-silver chloride (Ag/AgCl) is commonly used.

Electrochemical cells have been widely studied and optimized for applications that involve environment and air quality monitoring, in particular for oxygen sensing. As an example, in industrial fields, gas sensors' design is based on a pump approach. It consists in letting oxygen enter the sensor via capillary input from the top so that pressure gaps can be prevented. Moreover, to enhance the gas analyte diffusion in the electrochemical cell, layers made of porous polytetrafluoroethylene (PTFE) are employed [30]. Finally, several works have combined the use of PTFE films with room temperature ionic liquids (RTIL) as electrolyte to improve the reaction rate and consequently to ensure also fast measurement times [31], [32], [33].

## 1.2 CMOS interfacing circuits for amperometric sensors

The expansion of sensors in many application fields (e.g. gas sensing, bio-sensing etc.) has increased the need of integrating these devices on CMOS chips. As mentioned before (see Section 1.1), the full integration of sensors on CMOS integrated

---

<sup>2</sup> “Metallic electrode that will dissolve when a current is passed from it into a solution and that will have plated on it metal from the solution when the current is passed in the reverse direction” [29].

electronics is hard to achieve. In fact, although this solution reduces unpredictable parasitic effects, a fault in the sensing element could result in the failure of the entire integrated chip, making the cost of device failure substantially higher [7]. In order to overcome this issue, an alternative solution consists in designing an analog front-end that could be able to interface the sensor to an instrument (e.g. a micro-controller) that is able to interpret the information provided by the sensor. The primary purpose of the analog front-end is to accurately act as a conditioning circuit to ensure the correct functioning of the sensor. Secondly, it has to amplify the electrical signal generated by the sensor itself. In the end, the amplified signal is converted in the digital domain, usually by means of analog-to-digital conversion. In this section, we will explore several of the numerous solutions for the design of analog front-ends that interface sensors in different technologies. We will focus our attention on CMOS conditioning circuits that force the sensor to operate in amperometric mode and that allow an accurate current measurement (Subsection 1.2.1). Special considerations can be made on gas-sensing interfacing circuits; some works also provide a recognition technique for discrimination among various sensed gases (Subsection 1.2.2). Eventually, we will compare the mentioned works with respect to relevant parameters, like current dynamic range, resolution, power consumption and recognition signature.

### 1.2.1 Review of interfacing analog front-ends

Among the various hardware solutions for interfacing circuits, we have collected some of the most relevant works that are present in literature. They have been subdivided according to the principal design technique which they are based on. In this way, the differences between the mentioned front-ends can be better appreciated and a final overview can be done.

#### Analog-to-digital conversion

The analog-to-digital conversion is the key for accurate data acquisition in measurements of electrical signals like voltages and currents. For a good conversion, the main requirements consist of a resolution (minimum measurable quantity) as low as possible and a dynamic range (ratio between the largest and smallest measured values) as large as possible. According to the conversion technique, we can achieve a certain degree of accuracy. Moreover, a well-designed interfacing circuit allows to optimize the project parameters such as silicon area occupation and power consumption.

In many cases, the development of circuits for amperometric measurements is performed by combining analog and digital domains directly on-chip. As an example, in [34], a readout circuit has been designed with a self-adjustment digital block.

The system is shown in Figure 1.2.

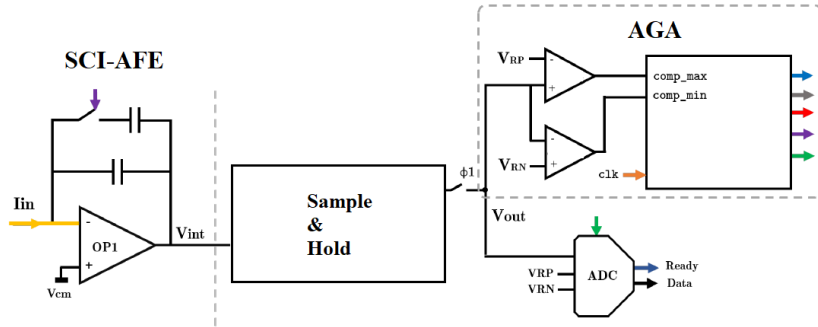


**Figure 1.2:** Block diagram of readout circuit in [34].

The circuit consists of four blocks: an analog front-end (AFE), a sample-and-hold circuit, an automatic gain adjustment (AGA) block and a 10-bit analog-to-digital converter (ADC). The AFE is based on a switched-capacitor integrator (SCI): the input current is turned into a voltage, according to the total capacitance. This is given by the sum of feedback capacitors, that are connected to the op-amp OP1 by means of switches controlled by AGA block. After being sampled, the voltage  $V_{int}$  enters both the AGA block, which tunes the feedback capacitors, and the ADC, where it is digitalized. In this configuration, the input current is subdivided into eight sub-ranges that are automatically set on-chip. This gives the advantage of avoiding manual calibration.

### Use of potentiostat

Other works - that specifically involve electrochemical sensors (see Subsection 1.1.2) - have managed to correctly bias the sensing device by using a potentiostat. It is an instrument that is useful in conditioning an electrochemical three-electrode cell. In particular, it must control the voltage potential between the working (WE) and reference (RE) electrodes. In amperometric mode, the potentiostat forces the voltage between WE and RE to be constant. Then, a current flows from WE to counter electrode (CE) [35]. It is provided to the interfacing circuit so that the main feature of the sensor can be measured.

In [36], an 8x12 array of integrated potentiostats is conditioned by an interfacing circuit depicted in Figure 1.3.

The electrochemical gas sensor is biased by a potentiostat that fixes constant voltage at the reference electrode. In addition, the working electrode is controlled by a current conveyor, i.e. a buffer that maintains a constant voltage. This

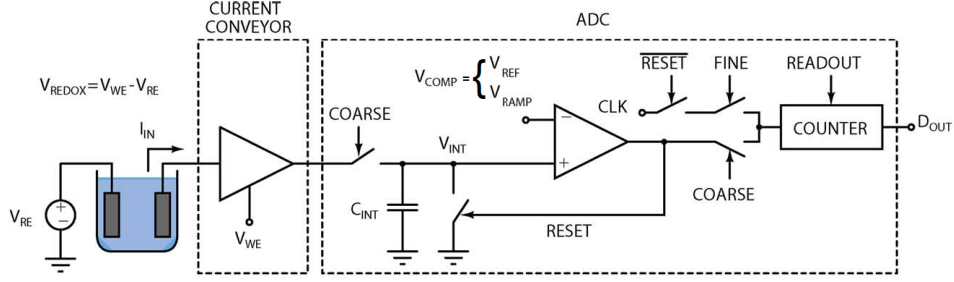


**Figure 1.3:** Top-level architecture of one channel in [36].

circuit is designed to exploit a dual-mode analog-to-digital conversion technique. In particular, the two modes are represented by current-to-frequency conversion and single-slope conversion. In the former phase, the input current charges the integrating capacitor. When the voltage on the capacitor ( $V_{INT}$ ) reaches the threshold ( $V_{REF}$ ), the comparator generates a pulse that discharges the capacitor through the reset switch. A wide input dynamic range is achieved as data conversion is performed in the time domain. This comes at a cost of a longer conversion time. As for a low input current, a long time is needed to charge the integrating capacitor. In the latter phase, a higher sampling rate for small input currents than that of the current-to-frequency ADC is used. The voltage across the capacitor is compared with a ramp voltage ( $V_{RAMP}$ ). Once  $V_{RAMP}$  equals  $V_{INT}$ , the counter stops counting. Then, the dual-mode architecture of the ADC breaks the dynamic range and sampling rate trade-off.

### Sigma-Delta ( $\Sigma\Delta$ ) conversion

In [37], an array of electrochemical gas sensors is connected to a multi-channel CMOS amperometric ADC. The architecture of a single channel is depicted in Figure 1.4.

The electrochemical gas sensor is biased by a potentiostat that fixes constant voltage at the reference electrode. In addition, the working electrode is controlled by a current conveyor, i.e. a buffer that maintains a constant voltage. A modulation switch disconnects the sensor from the circuit input and is used to pre-scale the input current. In the end, the analog-to-digital conversion is made by a simplified current-mode sigma-delta ( $\Sigma\Delta$ ) ADC. An SCI turns the current into a voltage. Then, a hysteretic comparator produces digital pulses that go in negative feedback to modulate the current. So, combining digital modulation of input currents and an incremental  $\Sigma\Delta$  ADC, the circuit achieves a wide dynamic range from sub-picoampere to several tens of microampere depending on the target concentration

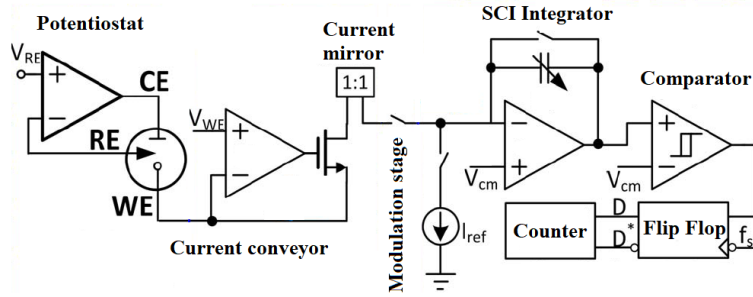


Figure 1.4: Single-channel architecture in [37].

range.

The conversion technique implemented in [37] is widely used for applications like bio-sensing, where the current signal provided by the sensors is typically affected by noise in the kilohertz bandwidth. Sigma-delta ( $\Sigma\Delta$ ) modulation makes use of oversampling to lower the noise contribution (noise shaping). So, with this approach, the resolution results to be improved allowing to reach values in the order of femtoampere [38]. In addition, a wide range of currents calls for multiple scales of measurement, while the long-time constants allow for long integration times. Long integration times call for oversampling and support the use of a lower-order sigma-delta modulator.

In [39] a 16-channel sensor array system for neurotransmitter sensing is linked to a multi-channel interface that exploits  $\Sigma\Delta$  modulation. Each channel employs a potentiostat within a switched-capacitor first-order  $\Sigma\Delta$  modulator, so that an incremental analog-to-digital converter is implemented. A simplified representation of the system is shown in Figure 1.5.

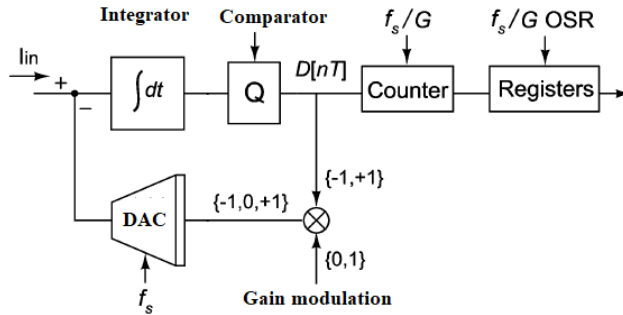
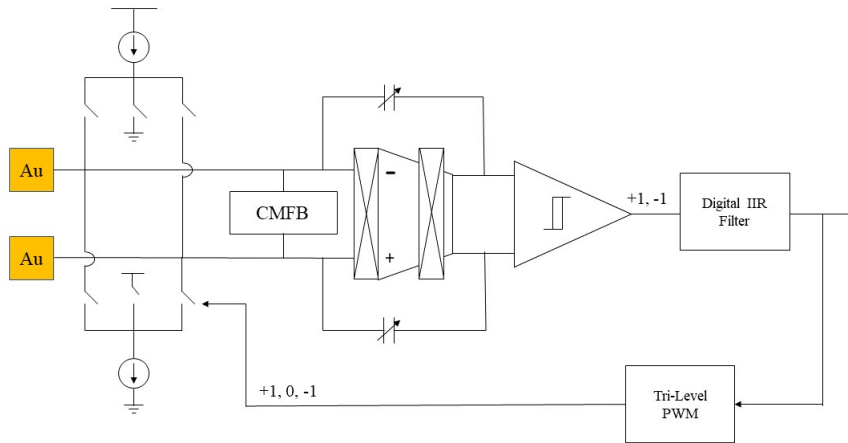


Figure 1.5: Single channel architecture in [39].

The current that a single sensor provides in output is converted into voltage by an integrator. A comparator (Q) is used to have a single-bit quantization of the

input voltage. A gain modulation block turns the binary feedback signal into a three-level signal. A feedback digital-to-analog converter (DAC) adds back to the input an output current. Finally, at the output of the channel, a decimator buffers the digital output with a counter and then oversamples it. Sigma-delta oversampled data conversion avoids the need for low-pass anti-alias filtering in the input, and decimation reduces high-frequency noise present in the current signal along with the shaped quantization noise. The duty-cycle modulation of current feedback and the variable oversampling ratio provide a programmable digital range selection of the input current spanning over six orders of magnitude from picoampere to microampere.

In [40], an 8-channel array of current sensing front-ends is implemented as depicted in Figure 1.6.



**Figure 1.6:** Single-channel architecture in [40].

Differently from the aforementioned works, this architecture is based on a differential measurement approach. The signal that the sensor of interest provides is always compared to the one of a reference sensor, so that it can get rid of slowly varying background current components and measure the component of our interest [41]. The input differential current enters a common-mode feedback (CMFB) circuit. It has the aim of preventing the common-mode contribution in the differential current by cancelling out the common-mode of the differential input voltage. An integrator, implemented with a single-stage folded cascode operational trans-conductance amplifier (OTA), converts the current into a voltage. It is subjected to a single-bit quantization by a comparator. Then, a digital infinite impulse response (IIR) filter transforms the one-bit input signal into a multi-bit one, so that the signal-to-quantization noise is improved. To close the loop, a tri-level pulse-width modulation (PWM) DAC feeds a pulse-modulated current signal back to the input. The analog

front-end consists of an equivalent first-order continuous-time  $\Sigma\Delta$  modulator, in which the digital conversion is performed by a discrete IIR filter. In this way, the same resolution of a  $\Sigma\Delta$  modulator is achieved with an improved area occupation efficiency.

amplifier, which integrates the input current and folds the output voltage within a predefined window;

### Comparison of the abovementioned analog front-ends

In conclusion, in Table 1.1 the main performance parameters of the works we have mentioned are reported to have a comparison.

#	Tech. [ $\mu\text{m}$ ]	$I_{min}$ [pA]	DR [dB]	#Ch	Pwr/ch [ $\mu\text{W}$ ]	Area/ch [ $\text{mm}^2$ ]
[34]	0.35	0.044	169	1	$5.83 \cdot 10^3$	0.31
[36]	0.35	24	95	192	188	0.04
[37]	0.5	0.1	164	50	241	0.157
[39]	0.5	0.1	140	16	3.4	0.25
[40]	0.18	0.123	139	8	50.3	0.11

**Table 1.1:** Comparison of state-of-the-art for current sensing AFEs.

As mentioned previously, the minimum current, or resolution ( $I_{min}$ ), is one of the most important features of an interfacing circuit since it provides an information about the accuracy of current measurements. The lowest minimum current is achieved in [34], in the order of tens of femtoampere. Still, this solution allows to have a quite large dynamic range (DR). It is due to the presence of the AGA block that allows an automatic arrangement of gain setting. Without the AGA block, a “standard” ADC-based circuit (e.g. in [36]) cannot reach a relatively good resolution as well. The choice of the conversion technique in the interfacing circuit affects the values of power consumption and the area occupation. In Table 1.1 the values of the aforementioned parameters are considered as quantity per channel. In general, in the works that are based on “standard” ADC conversion ([34], [36]) the channels of the array occupy a little area. This allows to increase the number of channels to obtain a better resolution. On the other hand, they result to consume more power than the ones based on  $\Sigma\Delta$  technique. The interfacing circuits implemented in [37], [39], [40] show a higher area occupation per channel. Nevertheless, they ones obtain a resolution in the order hundreds of femtofarad. In fact, even though the configuration of an  $\Sigma\Delta$  interfacing circuit is more complex than an ADC-based, it allows to optimize the power consumption per channel and to maintain a small minimum current.

## 1.2.2 Gas recognition systems

In literature there are several works that do not only propose the design of an analog interfacing circuit for sensors. With a particular attention on gas sensors, these works implement also a method for recognising the gas that the sensor is exposed to. The acknowledgement of gaseous species can assume many forms, either in hardware and software domain. In any case, the gas recognition is made on the basis of a so-called signature that acts as a reference for a comparison between different targets. In this way, when the feature of the gas is extracted by the analog front-end, we are able to distinguish between different gases since for each of them the signature is univocal. There are two essential phases for gas recognition:

1. *Calibration*: an electrical signal is generated by the sensor as an initial condition. For example, when it is exposed to air or to a gas with a certain concentration. Then, it is stored, for instance in a memory, and serves as a baseline.
2. *Sensing phase*: the sensor is subjected to gas exposure at specific conditions, so another electrical signal is produced. Then, comparing this signal with the one obtained in previous phase, we can derive the “identity” of the target by analyzing the change in signature.

Different recognition techniques have been developed according to the signature chosen for the gas acknowledgement. As a first example, in [42] a gas identification circuit for tin oxide ( $\text{SnO}_2$ ) gas sensors employs the frequency of an output spike train as signature. The calibration phase consists in exposing the sensors to target at high concentration. In the sensing phase, the concentration of gas changes. In Figure 1.7 the interfacing circuit for each sensor is depicted.

In the readout circuit, the sensor - represented as a varying resistor - is biased by a constant voltage so that a resistance-to-current conversion is performed. Then, a logarithmic compression is obtained using a forward-biased diode, i.e. the voltage across the diode depends on the logarithm of the current flowing through the sensor. Then, the produced voltage enters the spike generation circuit, where it is compared with two reference ( $V_{a1}$  and  $V_{a2}$ ). The first difference is amplified by an op-amp, giving  $V_{out}$ . The second one is converted by a transconductance amplifier into a current that feeds a capacitor, providing  $V_{comp}$ .  $V_{out}$  and  $V_{comp}$  go in input at a comparator. As long as the MOS-switch is off,  $V_{comp}$  increases until it reaches  $V_{out}$ . When it happens, a spike is generated. The pulse width of the spike depends on the propagation delay of the inverter chain. This architecture has been implemented to have a concentration-independent signature. So, in order to identify the target gas, the spike train frequency in sensing phase must correspond to the one measured in calibration phase.

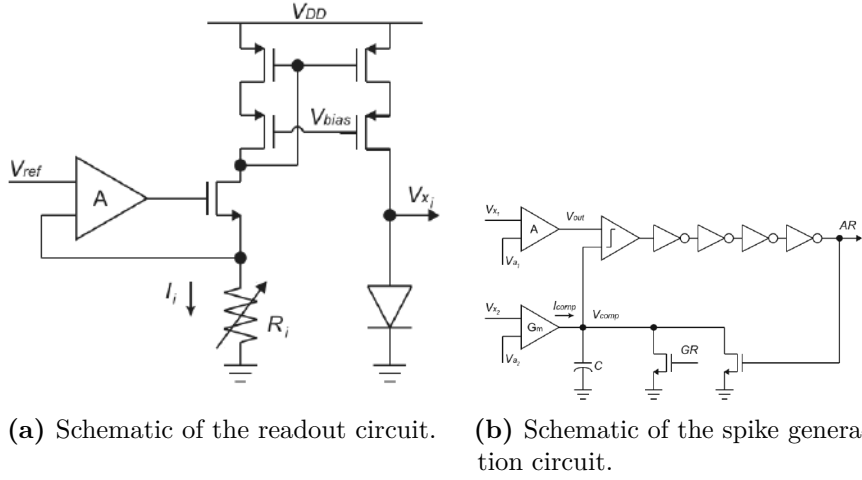


Figure 1.7: Front-end architecture in [42].

In [43] and [44], a  $4 \times 4$   $\text{SnO}_2$  gas sensor array is respectively designed and characterized to encode the gas identification with a unique spike pattern, used as signature. Hydrogen, ethanol and carbon monoxide are used to characterize the gas sensor array. The scheme of a single channel of the system is depicted in Figure 1.8.

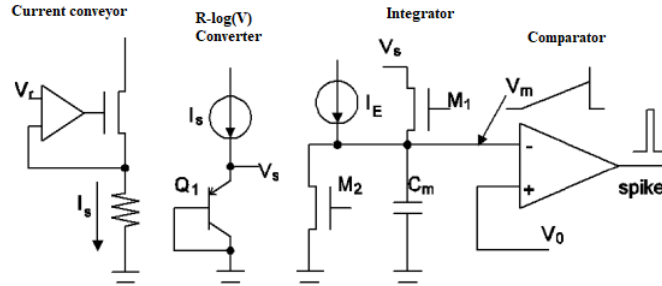
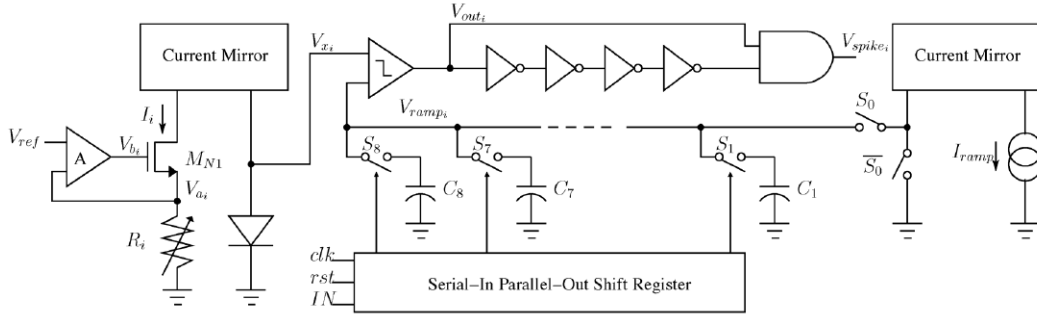


Figure 1.8: Single-channel scheme in [44].

As in [42], the resistance of the sensor is converted in a current. Then, a bipolar transistor in diode configuration makes the measured voltage dependent on the logarithm of the current. In calibration phase, the measurement of the sensor's baseline resistance ( $R_0$ ) without the presence of gas is stored, resulting in a reference voltage  $V_0$ . Later, in sensing phase, the gas exposure takes place and the resistance ( $R_s$ ) is acquired, giving the measured voltage  $V_s$ . After readout, there is a spike neuron circuit that provides the output signature. A clock signal controls a switch ( $M_1$ ). When the clock is high,  $V_m$  is set to  $V_s$ ; when it is low,  $V_m$  starts to integrate until it reaches  $V_0$ . When  $V_m = V_0$ , a spike is generated at the output of the

comparator. Each circuit in the array “fires” a spike at a certain time, but the algorithm has been optimized so that the spike interval between different sensors is concentration-invariant. So, the order of the spike pattern sequence does not change as well as the mutual delay between different spikes but the whole pattern shifts in time according to different concentration values.

In [45], a working principle - similar to previous works, concerning the interfacing of a sensor array - has been implemented, but the main relevant difference relies in the signature. The gas recognition is based on a two-dimensional (2-D) spatio-temporal signature. In Figure 1.9, the front-end of a single sensor is shown.



**Figure 1.9:** Single-channel scheme in [45].

The readout circuit is consistent with the ones designed in [42] and [44]. In the spike generation block, the measured voltage  $V_{x,i}$  is compared to the voltage across a system of switched capacitors. They are fed by a constant reference current  $I_{ramp}$  so that the voltage across the capacitors increases as a ramp ( $I_{ramp}$ ). A different integration capacitance is obtained according to the state of switches that are controlled by a serial-in parallel-output (SIPO) shift register. In this case, the spike patterns present different combinations with variable relative delays between single spikes. So, in the array the order of spike sequence is acquired row-by-row. In the end, a drift-insensitive and concentration-invariant 2-D spatio-temporal signature is obtained, i.e. a 4x4 matrix that is distinctively associated to a gas target.

In Table 1.2 a comparison between the examined gas recognition interfaces is shown.

#	Nr. of sensors	Technology [ $\mu\text{m}$ ]	Signature
[42]	2	0.35	Frequency
[43]-[44]	16	0.35	Unique sequence
[45]	16	0.35	2-D rank order

**Table 1.2:** Comparison of state-of-the-art for gas recognition circuits.

In [42] the choice of using only two sensors relies in the low complexity of gas

recognition. In fact, the implemented configuration allows to address poor selectivity of SnO<sub>2</sub> gas sensors (see Subsection 1.1.1) and to have a trade-off between identification efficiency and fabrication costs. Instead, in the other cited works ([43]-[44], [45]) the interfacing circuits have been developed with an array-based approach in order to increase the selectivity to many gas targets by employing a single device. Referring to the gas recognition mode, the frequency signature is simpler than the other ones. However, it requires a measuring instrument with a good accuracy to achieve a non-ambiguous response. On the other hand, in spite of the complexity of the signature, in [43]-[44], [45] there have been employed techniques that offer a higher reliability about the recognition of the gas target.



## Chapter 2

# **C<sub>60</sub> gas sensor: characteristics and requirements for interfacing circuit**

In Chapter 1 we have explored the state-of-the-art of gas sensors and their technologies. In addition, we have made an overview of several works that illustrate the design of CMOS interfacing circuits. The implementation of such analog front-ends is accomplished according to the type of sensor and the accuracy required for measuring electrical quantities involved in the sensing device. In the end, a brief view of gas recognition circuits has been described.

The aforementioned works are based on CMOS technology that has been spreading widely in the electronic field, thanks to advantages concerning power dissipation and tolerance to noise. In the last years, the demand of smaller devices has led to an unstoppable technological scaling-down, predicted by Moore's Law [3]. This approach, known as "more Moore", has allowed a more accentuated integration on-chip and an improvement in yield. On the other hand, inherent side-effects of smaller devices - like short channel effects, threshold voltage roll-off, heating effect etc. - emerged on nanometric scale. In particular, they affect key parameters of scaled-down transistors, like the intrinsic speed [46]. So, according to the last reviews of International Technology Roadmap for Semiconductors (ITRS) [5] and International Roadmap for Devices and Systems (IRDS) [6], an alternative approach has to be adopted to overcome the technological limits of CMOS technology. This approach has been named "Beyond CMOS", whose definition includes all the innovative technologies that expand beyond the current CMOS scaling constraints,

so that integrated circuits could achieve high speed, high density and low power consumption [6]. One of the most interesting Beyond CMOS technologies is *molecular electronics*, in which the basic “building block” is represented by one or more molecules. This branch of innovative electronic technologies has been spreading in the last few years and represents an interesting alternative solution to CMOS technology.

In this chapter, we will highlight the advantages of employing molecules as main components in such types of electronic devices. Moreover, we will provide a brief overview of molecular electronic sensors (MES), with particular attention on gas sensing applications (Section 2.1). Later, we will focus on the reference MES of this thesis work, i.e. a  $C_{60}$ -based molecular gas sensor. In particular, we will describe its electrical characteristics, starting with its behavioural model and the simulations demonstrating its sensing capabilities. According to them, we will extract the requirements for the implementation of an analog front-end that has the aim of acting as a gas recognition circuit (Section 2.2). In the end, the architecture of the interfacing circuit will be derived and represented at high level with a block scheme (Section 2.3).

## 2.1 Molecular electronic sensors

The features of molecular electronic technology are multiple and result in different advantages with respect to standard CMOS technology [47]:

- Their inherently nanometric sizes allow to compact the structure of devices so that area occupation is minimized and the response speed to external influence results to be fast.
- In fabrication step, molecules are able to self-assemble and rearrange autonomously as consequence of chemical processes (e.g. electromigration, etching etc.).
- According to the choice of molecule as channel between electrodes, the conduction properties change so highlighting the versatility of this technology.
- Generally speaking, the amount of current is lower than in CMOS technology. Currents vary in the order of nanoamperes to a maximum of few microampere, resulting in low power consumption.

On the other hand, molecules present several drawbacks that derive from their marked variability with respect to different factors:

- The synthesis processes of molecular devices, if not well controlled, could compromise the correct formation of channel. This could lead to a wrong

molecule as conductive channel or to a different structure of the molecular channel itself (e.g. more molecules instead of one).

- The bond between molecule and electrodes may be imperfect, so that the conduction in the device can be unpredictable.
- The molecule may have a torsion with respect to its nominal position, so that the conductivity has not the expected behaviour.

Recent studies have demonstrated that devices that refer to molecular electronic technology can be suitable for sensing applications. For this reason, they can be labelled as *molecular electronic sensors* (MES). In these devices the channel conductivity is modulated by the presence of a physical or chemical external stimuli. In this context, the acquisition, the processing and interpretation of the information provided by such devices follow an approach that tend to reproduce the behaviour of olfactory human system. The term associated to this method is *electronic nose*, or e-nose. In literature there are many applications that exploit the features of e-noses for sensing targets that are difficult to detect due to their small sizes. Some of the most significant are the following [48]:

- *Medical care*: diagnosis of diseases that can be revealed in presence of volatile organic compounds (VOCs). These substances are emitted by fluids produced by human body, like exhaled breath, sweat, saliva, urine, feces and so on [49].
- *Food industry*: monitoring of fruit, vegetables, meat and fish for ensuring their edibility. Aging or spoilage processes can be signaled by the presence of detected VOCs in food that have concentrations in the order of parts per million.
- *Agricultural production*: in-field monitoring of plants and soil to prevent diseases, insect infestations and pollution.
- *Public security*: detection of explosives and nerve agents, that have a fundamental importance in anti-terrorism action. Sensors are required to be fast in response and reliable to avoid false warnings.
- *Environment monitoring*: in-situ detection of gaseous targets. As mentioned in Chapter 1, gases present in air (see Figure 1.1) are multiple and some of them are toxic for human health, so an efficient sensing capability is required.

Molecular technology allows to assemble electronic components like resistance, capacitors and diodes [50]. Another electronic device that can be implemented according to this technology is the *molecular transistor*, also known as molecular field-effect transistor (molFET). This device makes use of a molecular compound

as conductive channel between two metal electrodes (typically made of gold or platinum) through which a current flows when the molecular transistor is properly biased. It also exploits one or more additive gate electrodes to improve switching capabilities and behave like an equivalent n-type or p-type MOS transistor [51]. For instance, they are exploited in detection of biological material [52], virus ([53], [54]) and humidity [55].

In gas sensing applications, which this thesis work is focused on, *single-molecule sensors* have gained great interest in last years. In particular, this detection approach allows to reach the ultimate resolution of a single molecule which yields a high sensitivity of the sensor. Moreover, the small dimension of detecting element makes it capable of sensing a large range of target. In addition, the detection of a single molecule allows to discriminate the actual event from noise, unlike in traditional ensemble measurements. Finally, single-molecule sensing implies that there is no need of a calibration phase since with this technique single events can be counted [56].

In the next section, we will study the characteristics of device described in the reference paper of this thesis work [57], i.e. a C<sub>60</sub>-based device employed as single-molecule gas sensor.

## 2.2 C<sub>60</sub>-based molecular gas sensor

In [57], an single-molecule device is analyzed to test its detecting capabilities for gas sensing application. It consists in a molecular junction formed by two gold electrodes and a C<sub>60</sub> molecule as sensing molecule. The sensor operates in amperometric mode, i.e. a constant voltage is applied between the two electrodes so that a current flows between the molecular channel. According to the gas it is exposed to, the current is subjected to a modulation with respect to the case in which no gas is present. As final result, this work achieves a selectivity of the molecular sensor to nitric oxide (NO) and nitrogen dioxide (NO<sub>2</sub>) in the presence of atmospheric gases, such as argon (Ar), nitrogen (N<sub>2</sub>), oxygen (O<sub>2</sub>), water vapor (H<sub>2</sub>O), carbon monoxide (CO) and carbon dioxide (CO<sub>2</sub>).

In Subsection 2.2.1, we will examine the structure of the device highlighting the choice of materials for sensing molecule and electrodes. Then, in Subsection 2.2.2, the mathematical model of modulation of current is provided. In the end, in Subsection 2.2.3, figures of merit that show the sensing capabilities of device will be depicted.

### 2.2.1 Device structure

The molecule that has the aim of detecting the presence of a gaseous target comes from the family of fullerenes. It is a group of carbon-based molecules that count  $2(10+N)$  carbon atoms. The specific compound that has been chosen is the C<sub>60</sub> fullerene that contains 60 carbon atoms forming a spherical shape, organized in alternate pentagons and hexagons. It is characterized by high symmetry and a diameter of 7 Å. In addition, it results to be stable at room temperature and easy to synthesize. This molecule has been proved to be suitable for detection of gases like NH<sub>3</sub>, NO<sub>2</sub>, CO and H<sub>2</sub>O [58]. The C<sub>60</sub> molecule is put between the two electrodes to act as a conductive channel through which the current will flow.

The two electrodes' material is gold (Au), which is a metal that is suitable for molecular sensors. In fact, it is a ductile and flexible material that can be exploited to form controllable nanogaps that can host molecular channels. Some of the techniques mostly used for this purpose are electromigration and mechanically controllable break junction.

The most stable configuration for Au-C<sub>60</sub> junction is the one described in [57]. The gold electrodes present a face-centered cubic lattice (FCC) with (111) orientation, according to Miller notation [59]. The C<sub>60</sub> fullerene is rotated so that the center of external hexagons are aligned to a gold atom in the second layer of the metal structure, i.e. at the center of FCC lattice of both Au electrodes.

The size of nanogap in which the C<sub>60</sub> is inserted takes into account the diameter of the sensing molecule itself (about 7 Å) and the bond length between C<sub>60</sub> and gold electrodes (about 2.4 Å on each side). Eventually, the gas target molecule has been simulated to be at a certain distance to C<sub>60</sub> so that it can be studied to act as a sensing element. In particular, there should be a partial overlap of van der Waals shells in order to establish a strong interaction between sensing and sensed molecules.

### 2.2.2 Mathematical model of conductivity in Au-C<sub>60</sub>-Au system

The conduction in molecular systems can be analytically described according to the model of 0-dimensional (0D) systems, also known as quantum dots [60]. The analytic model is mainly based on the energy levels occupied by electrons in gold electrodes (from now on also named respectively source, S, and drain, D) and the ones of molecular orbitals in C<sub>60</sub>. As regards the electrodes, they are characterized by the so-called Fermi levels. They represent the energy levels at which electrons have 50% of probability to occupy them at thermodynamic equilibrium, according to the Fermi-Dirac distribution in Equation 2.1:

$$f_{\{S,D\}}(E, E_{F\{S,D\}}) = \frac{1}{1 + e^{\left(\frac{E - E_{F\{S,D\}}}{kT}\right)}} \quad (2.1)$$

where  $k$  is the Boltzmann constant,  $T$  is the operating temperature and  $E_{F\{S,D\}}$  are Fermi energy levels for source and drain electrodes.

On the other hand, the molecular dot (in this case C<sub>60</sub>) is characterized by different molecular orbitals that are coupled to the drain and source electrodes. Regarding to the conduction in the C<sub>60</sub> molecular channel, the energy states that contribute to the flow of electrons in the device are the ones that are within the Fermi energy levels.

The bond between the electrodes and the molecular dot is quantified by the so called coupling factor, whose mathematical expression is given by Equation 2.2:

$$\gamma_i = \frac{\hbar}{\tau_i} \quad (2.2)$$

where  $\hbar$  is the reduced Planck constant and  $\tau_i$  is the escape time that an electron takes to cross interface between electrode and the  $i$ -th molecular orbital of the quantum dot. If the escape time is short, then electrons are favoured to “jump” from electrode to dot and viceversa. In this case, we have a strong coupling between the C<sub>60</sub> dot and the electrodes, in which the electron transport is dominated by coherent processes. In the opposite case, we have a weak coupling, in which the electron transport is dominated by incoherent processes (i.e. scattering).

The type of coupling influences the density of energy states ( $D_E$ ) of the whole system. In the case of weak coupling, the distribution of energy states follow a Dirac-delta function, for which each state is localized at discrete energy level ( $E_i$ ) corresponding to a molecular orbital energy (Equation 2.3):

$$D_{E_i}^{(w.c.)}(E) = \delta(E - E_i) \quad (2.3)$$

This is due to the fact that for long escape time, the probability that an electron in the dot is located in correspondence of the energy level  $E_i$  can be considered equal to 1. On the contrary, when a strong coupling occurs, the probability of find an electron in the dot at level  $E_i$  decreases exponentially with time because the transition in dot-electrode interface is more favoured with respect to the previous case. Then, the density of energy states follows a Lorentzian distribution, according to Equation 2.4:

$$D_{E_i}^{(s.c.)}(E) = \frac{\frac{\gamma_i}{2\pi}}{(E - E_i)^2 + \left(\frac{\gamma_i}{2}\right)^2}, \quad \text{with } \gamma_i = \gamma_{i,S} + \gamma_{i,D} \quad (2.4)$$

where  $\gamma_{i,\{S,D\}}$  are the coupling factor of the  $i$ -th molecular orbital of the dot with the source and drain electrodes. In this case, we obtain a profile of energy states that is characterized by a broadening of levels.

At this point, we can define transmission function that is associated to the  $i$ -th energy level. It represents the probability of an electron at energy  $E$  to flow from one contact to the other passing through a specific molecular orbital  $E_i$ . Its analytical expression is shown in Equation 2.5:

$$T_i(E) = \frac{\gamma_{i,S} \gamma_{i,D}}{\gamma_{i,S} + \gamma_{i,D}} D_{E_i}(E) \quad (2.5)$$

It depends on the coupling at the interfaces between the molecular dot and the two electrodes and on the density of energy states that they have established in the system. To evaluate the contribution of all energy states, the transmission spectrum of the whole system is given by sum of the transmission functions of each energy level (Equation 2.6):

$$T(E) = \sum_i T_i(E) \quad (2.6)$$

It represents the probability of an electron at energy  $E$  to flow from one contact to the other passing through the molecular channel, considering all the molecular orbitals. Taking into account Equations 2.1 and 2.6, a model of the current flowing from drain to source electrodes through the molecular dot is provided by the simplified Landauer formula (Equation 2.7):

$$I_{DS} = \frac{2q}{h} \int_{-\infty}^{+\infty} T(E) [f_S(E, E_{FS}) - f_D(E, E_{FD})] dE \quad (2.7)$$

where  $q$  is the electron charge.

In particular, the conduction in the molecular system is possible when a voltage potential  $V_{DS}$  is applied between drain and source electrodes. The voltage  $V_{DS}$  acts on the Fermi energy levels of electrodes by opening the so called bias window:

$$E_{FD} - E_{FS} = -qV_{DS} \quad (2.8)$$

For example, for  $V_{DS} > 0$  V, the Fermi level of source ( $E_{FS}$ ) will be higher than the one of the drain ( $E_{FD}$ ), so that electrons will go from source to drain electrode. Under the assumption that the two contacts between the molecule and the electrodes are symmetrical, the bias window will open symmetrically around a reference energy for the C<sub>60</sub> molecule, fixed at 0 eV.

The current flowing through the molecular dot, that is the result of the integration of transmission spectrum, will have the most consistent contribution from the  $T(E)$  peaks involved in the bias window. In this simplified model, the transmission spectrum is considered to be the same as in equilibrium. In fact, in first approximation

effects out of equilibrium (e.g. charging effect) are neglected when a narrow bias window is opened.

The complete analytical model of conduction in quantum dots is explained in [61]. The presence of a gaseous target nearby the  $C_{60}$  sensing molecule introduces a change in its conductivity and then in the current that flows in the sensor with respect to the case in which no gas molecules are present.

In the next subsection, the behaviour of the sensor when it is exposed to different gases will be investigated.

### 2.2.3 Sensing capabilities

As mentioned before, when the Au- $C_{60}$ -Au device is biased in amperometric mode (with a constant positive  $V_{DS}$  across it), a current ( $I_{DS}$ ) flows from drain to source. The tool used for simulation of the electrical behaviour of  $C_{60}$ -sensor is *Cadence Virtuoso*. In Figure 2.1, the schematic of a test bench for the bias of the molecular sensor under examination is depicted.

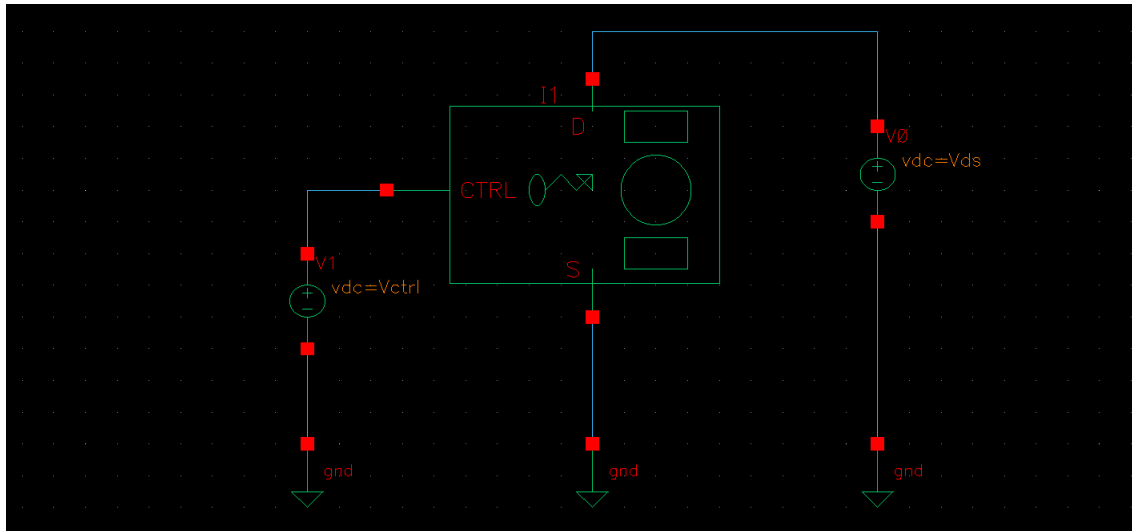


**Figure 2.1:** Test bench for  $C_{60}$ -sensor.

The model of the sensor is provided on the basis of a *Verilog-A* file. In particular, it fetches the values of the current  $I_{DS}$  from a Look-Up Table (LUT) [62]. The data have been obtained from the combination of Extended Hückel Theory (EHT) and Non-Equilibrium Green's Function (NEGF) algorithms [57].

Since in [57] the transmission spectrum of the molecular sensor is considered in  $[-1,1]$  eV range and the bias window is assumed to open symmetrically around 0 eV energy level, the range for drain-source voltage  $V_{DS}$  is  $[0,2]$  V. In total, 11 points -

for each gas target - are considered in correspondence of  $V_{DS}$  range, with a step size of 0.2 V.

Since the sensor is supposed to work in amperometric mode, the sensor has to be biased with a constant voltage generator (instantiated as  $V0$ ) between drain (D) and source (S) terminals. Instead, another generator ( $V1$ ) imposes a constant voltage ( $Vctrl$ ) that encodes the presence of a gas target. Therefore, it is just a fictitious voltage pin aimed in modelling the presence of a specific target gas close to the sensor. In Table 2.1, the gas molecules that can be detected by the C<sub>60</sub>-sensor are reported with the corresponding values of  $Vctrl$ .

In Figure 2.2 the  $I_{DS} - V_{DS}$  trans-characteristic of the sensor, when no gas is detected, is depicted.

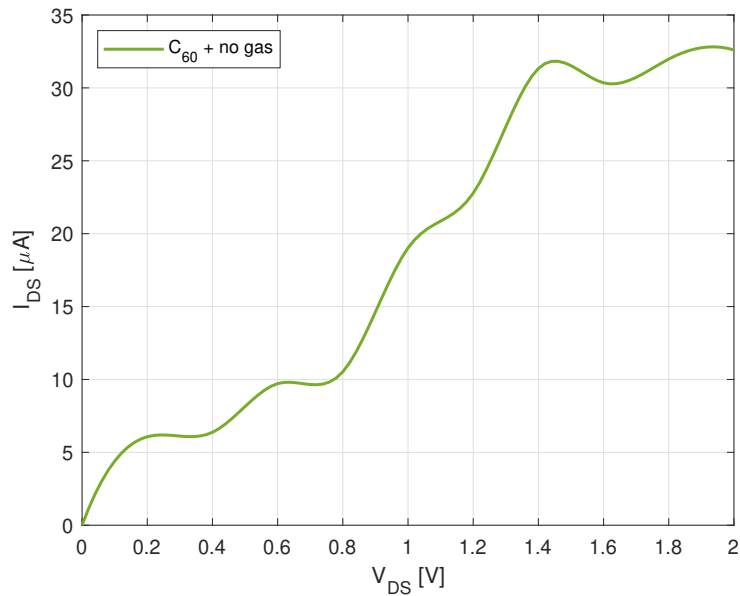


**Figure 2.2:**  $I_{DS} - V_{DS}$  trans-characteristic of the C<sub>60</sub>-sensor (with no gas).

The current is the result of the integration of the transmission spectrum of the C<sub>60</sub> molecular channel that has been coupled with gold electrodes, when a bias window is “opened” (Equations 2.7-2.8). In the plot a cubic spline interpolation of LUT points is used. In this analysis, it has been adopted to have a smooth behaviour between successive samples of current flowing in the sensor. In this work, only cubic spline interpolation of the I-V trans-characteristics will be considered. In particular, they have been performed directly in Cadence starting from the values present in the LUT [57].

When the molecule of a gas species approaches the C<sub>60</sub>, the trans-characteristic is modulated, according to the principle described in Subsection 2.2.2. As an example,

Vctrl [V]	Gas target
0	No target
1	Ammonia (NH <sub>3</sub> ) with “N down” orientation
2	Ammonia (NH <sub>3</sub> ) with “H down” orientation
3	Argon (Ar)
4	Carbon monoxide (CO)
5	Carbon dioxide (CO <sub>2</sub> )
6	Nitrogen (N <sub>2</sub> )
7	Water vapor (H <sub>2</sub> O) with “flat” orientation
8	Water vapor (H <sub>2</sub> O) with “H down” orientation
9	Water vapor (H <sub>2</sub> O) with “O down” orientation
10	Oxygen (O <sub>2</sub> )
11	Methane (CH <sub>4</sub> )
12	Butane (C <sub>4</sub> H <sub>10</sub> )
13	Lead sulfate (PbSO <sub>4</sub> ) with “flat” orientation
14	Lead sulfate (PbSO <sub>4</sub> ) with “flat rotated” orientation
15	Lead sulfate (PbSO <sub>4</sub> ) with “flat up-down” orientation
16	Lead sulfate (PbSO <sub>4</sub> ) with “SO down” orientation
17	Lead sulfate (PbSO <sub>4</sub> ) with “Pb down” orientation
18	Nitric oxide (NO) with “O down” orientation
19	Nitric oxide (NO) with “N down” orientation
20	Nitric oxide (NO) with “flat” orientation
21	Lead oxide (PbO) with “O down” orientation
22	Lead oxide (PbO) with “flat” orientation
23	Lead oxide (PbO) with “Pb down” orientation
24	Lead chloride (PbCl <sub>2</sub> ) with “flat” orientation
25	Lead chloride (PbCl <sub>2</sub> ) with “Cl down” orientation
26	Lead chloride (PbCl <sub>2</sub> ) with “Pb down” orientation
27	Nitrogen dioxide (NO <sub>2</sub> ) with “O down” orientation
28	Nitrogen dioxide (NO <sub>2</sub> ) with “N down” orientation
29	Nitrogen dioxide (NO <sub>2</sub> ) with “flat” orientation

**Table 2.1:** Encoding of gas targets detected by C<sub>60</sub>-sensor.

the modulation of current flowing in the sensor when a molecule of nitric oxide (NO) bonds with the C<sub>60</sub> molecule is depicted in Figure 2.3.

The presence of the NO molecule acts on the conductivity of the sensor since it introduces a change in the transmission spectrum’s peaks [57]. This modulation results in oscillations of current flowing in the sensor in the order of few microamperes. Another factor that is involved in the modulation of current is the orientation of

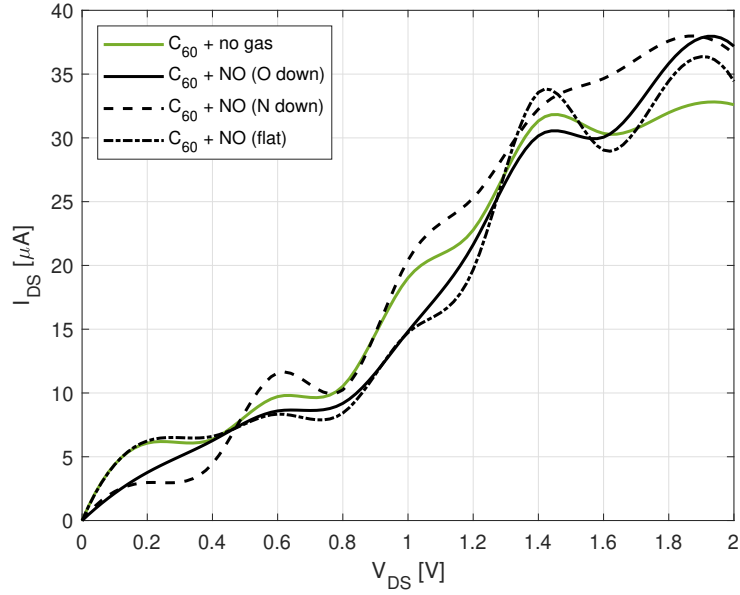


**Figure 2.3:**  $I_{DS} - V_{DS}$  trans-characteristic of the C<sub>60</sub>-sensor (with NO, in different orientations).

the target molecule with respect to the C<sub>60</sub>-axis, along which the current flows. In particular, the word “down” in graphs’ label indicates the nearest atom of the gas target to the sensing molecule of the sensor. Whereas, the word “flat” means that the atoms of target are aligned to the axis of molecular channel, i.e. they are equidistant to it.

As mentioned in Section 1.1, a sensor has to conjugate a good sensitivity to a wide range of gaseous targets and a high selectivity to single targets in order to be able to distinguish between them. In the case of the C<sub>60</sub>-sensor, it is characterized by a quite large sensitivity to gases reported in Table 2.1. To test its selectivity, in [57] there are different simulations of comparison between sensor’s responses to different targets. Specifically, the C<sub>60</sub>-sensor is required to sense molecules of potentially toxic gases (e.g. CH<sub>4</sub>, C<sub>4</sub>H<sub>10</sub>, NH<sub>3</sub>, NO or NO<sub>2</sub>) in presence of common atmospheric gases. The analysis that have been conducted in the reference paper [57] takes into account the responses to molecules of Ar, CO, CO<sub>2</sub>, gaseous H<sub>2</sub>O, N<sub>2</sub> and O<sub>2</sub> to act like atmospheric references gases.

The sensor can be considered selective to a target when I-V trans-characteristic of the sensor - modulated by its presence - shows a significant margin in current values with respect to the responses of the sensor itself to atmospheric gases. Since the I-V curves for different gases have absolute values of  $I_{DS}$  that differ of few microamperes over the  $V_{DS}$  range, it is useful to consider the variation of current (in absolute and percentage terms) with respect to the case in which no gas is

detected by the sensor (Equations 2.9-2.10):

$$\Delta I_{DS} = I_{DS,gas} - I_{DS,0} \quad (2.9)$$

$$\Delta I_{DS,\%} = \left( \frac{I_{DS,gas} - I_{DS,0}}{I_{DS,0}} \right) \cdot 100 \quad (2.10)$$

where  $I_{DS,0}$  and  $I_{DS,gas}$  is the value of current flowing in the sensor, respectively, when no gas is present and when a target is detected.

In Figures 2.4-2.5-2.6-2.7-2.8 the responses of C<sub>60</sub>-sensor (in terms of  $\Delta I_{DS}$ ) to different targets in presence of atmospheric gases are depicted.

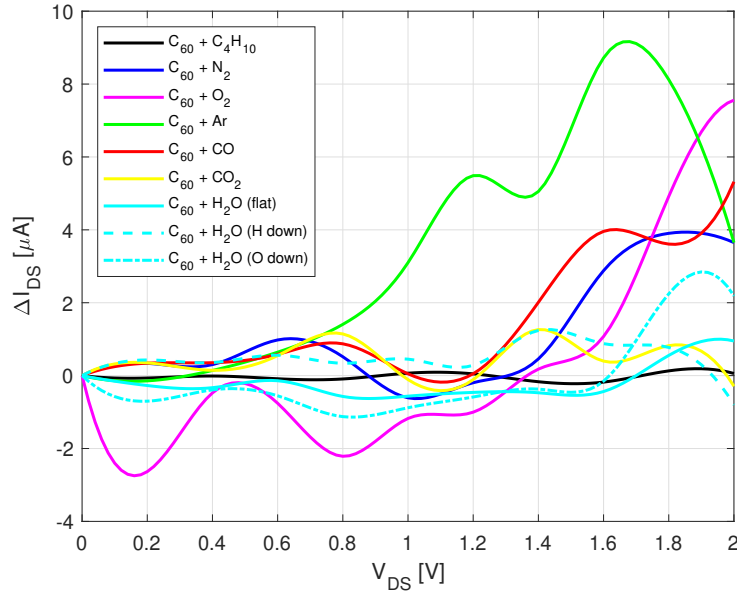


**Figure 2.4:** Response of C<sub>60</sub>-sensor to butane (C<sub>4</sub>H<sub>10</sub>).

They are again the cubic spline interpolation (performed in Cadence Virtuoso) of the LUT ab initio calculations, as described in [57]. The C<sub>60</sub>-sensor presents poor selectivity to C<sub>4</sub>H<sub>10</sub> and CH<sub>4</sub> since their trans-characteristics have a similar behaviour over the considered  $V_{DS}$  range. For NH<sub>3</sub>, the deviation of current with respect to most of atmospheric gases is significant in [1.8,2] V sub-range of bias window. Still, the selectivity cannot be considered reliable. On the contrary, the C<sub>60</sub>-sensor shows a promising detection capability for NO and NO<sub>2</sub> targets. For the former, the trans-characteristics for all its orientations are distinct to the ones of atmospheric gases around  $V_{DS} = 1$  V. For the latter, the bias window has to be opened until [1.6,1.8] V to have a notable deviation from other atmospheric gases. In the next section, the electrical characteristics of C<sub>60</sub>-based gas sensor will be

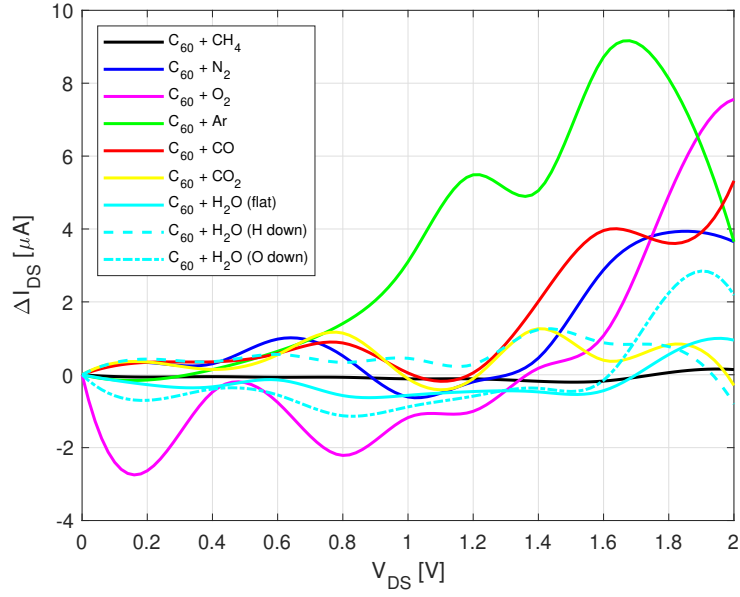


**Figure 2.5:** Response of C<sub>60</sub>-sensor to methane (CH<sub>4</sub>).

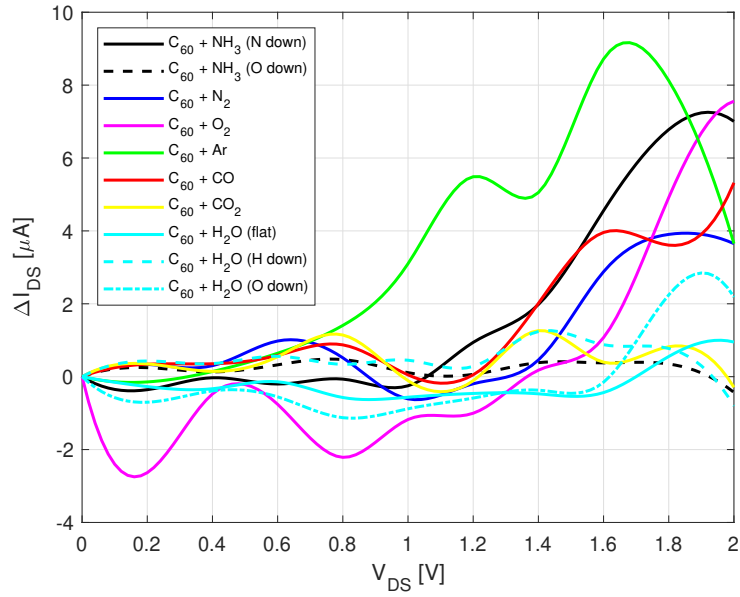


**Figure 2.6:** Response of C<sub>60</sub>-sensor to ammonia (NH<sub>3</sub>).

useful to derive the architecture of a circuit that allows the recognition of a gas target which the sensor is exposed to.

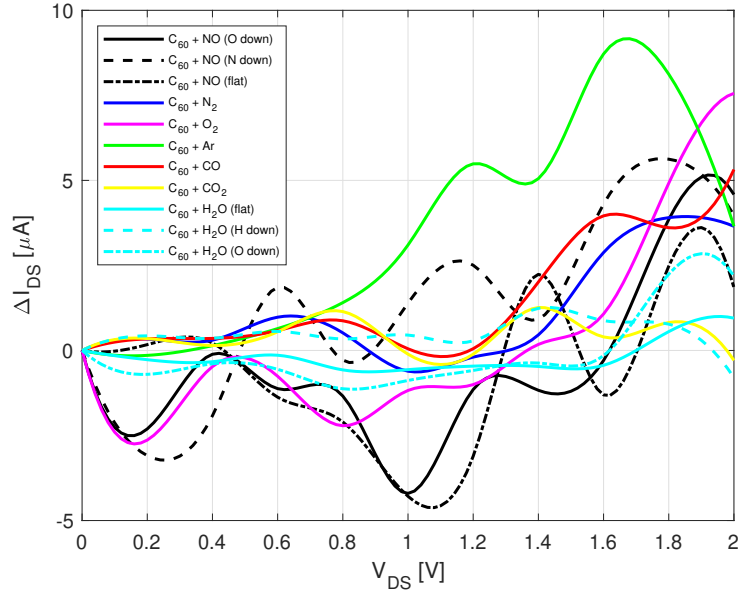


Figure 2.7: Response of  $C_{60}$ -sensor to nitric oxide (NO).

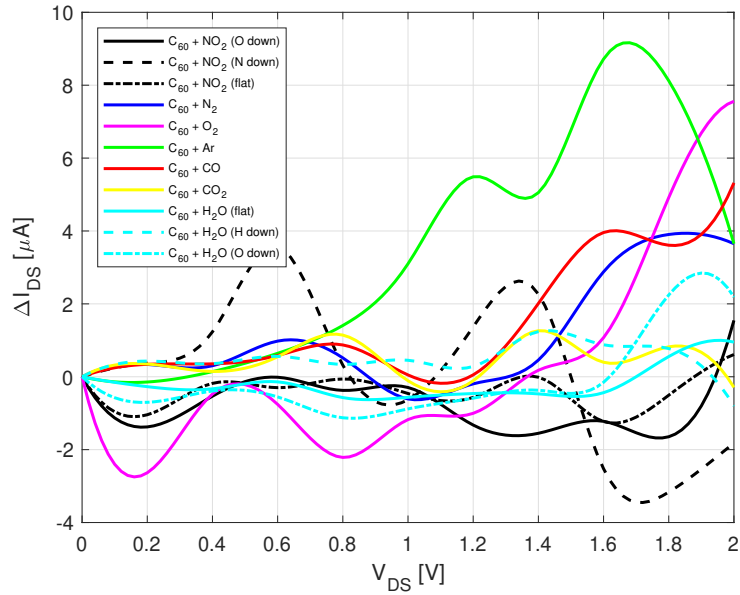


Figure 2.8: Response of  $C_{60}$ -sensor to nitrogen dioxide ( $NO_2$ ).

## 2.3 $C_{60}$ -sensor's requirements and front-end architecture derivation

In previous sections, an overview of innovative technologies for single-molecule gas sensing applications has been provided. In particular, the working principle of the

gas sensor, based on  $C_{60}$  fullerene as sensing molecule, has been deepened. Since its technology is difficult to integrate to electronic boards due to its nanometric sizes, it needs a hardware interface that could act as a conditioning circuit for the sensor and make its electrical characteristics compatible with standard CMOS requirements. Moreover, to fully exploit the sensing capabilities of the sensor, the analog front-end can be designed such that the output of the circuit could allow the identification of the gas detected by the sensor itself.

In the following subsections, the choices for the design of a gas recognition circuit will be discussed by taking into account the requirements of the  $C_{60}$ -sensor that can be extracted from the description in Section 2.2. In the end, a high-level architecture of the analog front-end will be drawn to be used as reference for the detailed design in Chapter 3.

### 2.3.1 Acquiring current from the sensor

The figures of merit that illustrate the behaviour of the  $C_{60}$ -sensor are its I-V trans-characteristics, depicted in Subsection 2.2.3. From them, there can be extracted the electrical requirements that are useful for the design of the conditioning circuit. Besides, the I-V curves provide information on gas sensing capabilities of the device by means of comparison between the different targets that the sensor faces. Then, the electrical quantity that has to be focused is the current that flows through the  $C_{60}$ -sensor.

The conditioning circuit, also named as *readout circuit*, must bias the sensor, so that the conduction occurs in the sensor, and provide the current to a successive stage for the identification of the detected gas. The readout circuit consists in two block stages whose working principles are now described.

#### Biasing the sensor

As explained in Subsection 2.2.3, the  $C_{60}$ -sensor requires to be biased in order to activate its conduction principle. Specifically, a voltage potential has to be applied between the drain and source gold electrodes ( $V_{DS}$ ). This voltage allows to open a bias window in which the transmission spectrum of the system is integrated, resulting in a flowing current ( $I_{DS}$ ).

Since this gas-detecting device should operate in amperometric regime, the requirement about the bias of the sensor is to apply a constant voltage  $V_{DS}$  between drain and source terminals. In particular, the biasing stage should guarantee the correct behaviour of the sensor over all the range of  $V_{DS}$  extending from 0 to 2 V, for all the targets it can be exposed to. In addition, this block should be able to drive the amount of current that flows through the sensor, which reaches a maximum value around 60  $\mu$ A.

A biasing stage that can meet the above-mentioned requirements is a *current conveyor*. It consists in a voltage follower: at the input, a constant voltage  $V_{REF}$  is applied so that its value is imposed across the sensor's electrodes. Then, a current  $I_{DS}$  flows in the sensor according to the I-V trans-characteristics of the  $C_{60}$ -sensor. Moreover, an active element (for example, an n-type MOS), in series with the voltage buffer, is useful to drive the same current  $I_{DS}$  and connect the biasing stage to the rest of the readout circuit.

#### Decoupling the sensor from output

Once the sensor is properly biased, a current flows and it has to be driven from the input to the output branch of the circuit in order to be processed and, if necessary, modulated. Moreover, the input side of the circuit, where the sensor is located, has to be decoupled from the output. This allows to control the electrical quantity in both the sides of the circuit and prevent that the information carried by the current at the output is altered.

A *current mirror* is the most suitable solution to fulfil these tasks. This type of circuits present heterogeneous configurations and each of them is characterized by advantages and drawbacks that have an impact on the accuracy of output current and the performances of the overall front-end. In the reserved section in Chapter 3, the choice of the configuration employed in this thesis work will be explained.

#### 2.3.2 Converting analog quantity in digital domain

The mirrored current keeps carrying the information about detection of gas targets by the  $C_{60}$ -sensor. Nevertheless, as stated in Subsection 2.2.3, the current values - for different sensed gaseous species - are similar over the considered  $V_{DS}$  range. So, a great accuracy is required for a measuring instrument which the sensor has to be interfaced with. In particular, for the recognition of the gas, a signature is needed. It is an electrical quantity or a graphical representation that is used to distinguish between different targets. The signature of a gas target must be univocal so that there is no ambiguity in the labelling.

Measurements of low current might be affected by errors that could compromise the correct recognition of the target [63]. In the application of this thesis work, the deviations of current values - in the case of different gas targets - are in the order of few microamperes, so a reliable recognition could be achieved with solid state electronics like the CMOS-based devices. Nevertheless, possible errors introduced by fabrication tolerances of electronic components in the analog front-end are likely to worsen its reliability. Therefore, chemical and electronic (thermal) noise can strongly affect the output current of the sensor. Usually, to improve the sensing resolution and reliability, the sensor current can be converted in another physical quantity to

be monitored, e.g. a frequency (through a dedicated current-to-frequency converter). In Subsection 1.2.2, the described gas recognition systems follow a common approach to address the reliability of targets' acknowledgement. Specifically, they exploit the conversion of analog electrical quantities (like voltages and currents) into discrete pattern of spikes. This approach is similar to analog-to-digital conversion. Though, this technique has not the aim of acquiring amperometric measurements of the current in the digital domain. The final purpose of this approach is the labelling of the target that the sensor is subjected to by means of a univocal signature.

In the context of this work, and as stated above, single-molecule detection requires a reference output quantity that could ensure a good reliability in distinguishing the gas target that can be detected by  $C_{60}$ -sensor. So, I have chosen the frequency as signature since it can be acquired with high accuracy and resolution and measured by low cost commercial instruments like a micro-controller.

Taking into account all the above-mentioned considerations, I have implemented a *current-to-frequency converter* that inputs the current provided by the current mirror. In the end, it provides an output frequency to be used as indication for the recognition of the target detected by the  $C_{60}$ -based sensor.

### 2.3.3 Final architecture of the analog front-end

Summing up all the functional stages that have been described in previous subsections, Figure 2.9 shows a high-level architecture for the gas recognition system that is proposed in this thesis work.

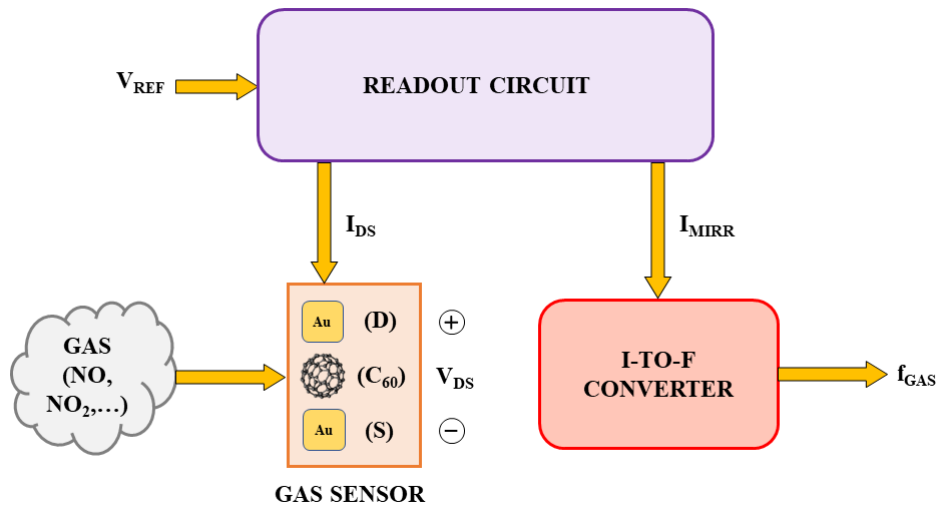


**Figure 2.9:** High-level architecture of gas recognition system for  $C_{60}$ -sensor.

The readout circuit has the purpose of suitably biasing the sensor at the desired

voltage value. Moreover, it decouples the current flowing in the sensor from the one that flows in the reading circuit. Then, the current-to-frequency converter is used to obtain the frequency as signature for the recognition of the gas target, starting from the current provided by the readout circuit.

In the next chapter, the Cadence Virtuoso implementation of each functional block will be described in detail. Then, they will be simulated to test their single electrical behaviour. In this way, once the correct functioning of every stage is validated, they can be joined together to verify the actual recognition capability of gas targets of the designed analog front-end.



## Chapter 3

# Characterization of the analog front-end

In Chapter 2, an electronic device in molecular technology, based on  $C_{60}$  fullerene molecule as conductive channel and gold electrodes, has been studied and described. In [57], the Au- $C_{60}$ -Au molecular junction has been investigated for single-molecule gas sensing application. Biasing the device in amperometric regime and exposing it to different gas targets, it has shown good sensitivity to several gaseous compounds (reported in Table 2.1). Moreover, the  $C_{60}$  sensor has proved to be characterized by a good selectivity to some of them - in particular, to nitric oxide (NO) and nitrogen dioxide ( $NO_2$ ) - in presence of common atmospheric gases.

Taking into account the electrical requirements that have been extracted from the I-V trans-characteristics of the sensor (see Subsection 2.2.3), this chapter is focused on the implementation of a CMOS analog front-end that has the aim of acting both as conditioning circuit for the  $C_{60}$  sensor and as a gas recognition system based on a frequency signature. The definition of the schematic will follow the high-level architecture derived from the above-mentioned requirements (see Figure 2.9) and its functional blocks will be characterized in detail. Then, they will be simulated to verify its correct behaviour.

The tool used for the implementation of the analog front-end and the simulation of its electrical behaviour is Cadence Virtuoso. In the implementation environment, a particular attention will be given to the *hardware description language* (HDL) models of some instances inserted in the schematic, in particular *Verilog-A*. This language permits the handling of analog signal together with digital ones, so that the components can be compliant with their respective functions in the interfacing circuit.

## 3.1 Readout circuit

In the first stage of the CMOS analog front-end, the sensor has to be connected to a readout circuit. Referring to Figure 2.9, a voltage  $V_{REF}$  is applied at the input so that the sensor is properly biased and provides at the output a current  $I_{MIRR}$  that can be either the same one that flows in the sensor ( $I_{DS}$ ) or the modulated  $I_{DS}$ . Then, the current  $I_{MIRR}$  is sent in input to the next stage to be converted in frequency for the recognition of the target.

The implementation of readout circuit is divided in two blocks:

1. a current conveyor, that needs to both bias the sensor and drive the current that flows through the device itself;
2. a current mirror, that allows to replicate the current that flows in the sensor to the output of the readout circuit.

The  $C_{60}$ -sensor needs to be biased with high accuracy since its I-V trans-characteristics show that for little variations of voltage  $V_{DS}$  the current  $I_{DS}$  changes in a significant way. So, a reference should be fixed for the voltage which polarizes the sensor. Then, the source electrode is connected to ground ( $V_S = 0$  V). In such way, the voltage applied to the drain electrode ( $V_D$ ) will result to be equal to the voltage  $V_{DS}$ . In Figure 3.1, the detailed block scheme of the readout circuit is depicted.

Since according to the requirements (see Subsection 2.3.1) the biasing voltage  $V_{DS}$  is positive, the current will flow from drain to source terminal of the sensor, as expected. To maintain this flowing direction in the output branch of the current mirror, it will be placed above the rest of the circuit.

The schematics proposed in the next subsections will be described with respect to the function of each component, so that they can be assembled to simulate the behaviour of the readout circuit.

### 3.1.1 Current conveyor

The implementation of the current conveyor block requires to have two main components that could respect the requirements about the bias of the  $C_{60}$ -sensor. Firstly, the voltage  $V_{REF}$  has to be applied to a voltage buffer. It has to “copy” the input voltage to another node of the circuit, in particular to the drain terminal of the sensor so that  $V_{DS} = V_{REF}$ . In addition, this configuration has the advantage of providing low output impedance and thus impedance decoupling of the circuit from the supply line.

Secondly, the drain terminal of the sensor must be connected to the current mirror, placed above the current conveyor, and the current  $I_{DS}$  must be consistent to the different I-V trans-characteristics of its model.

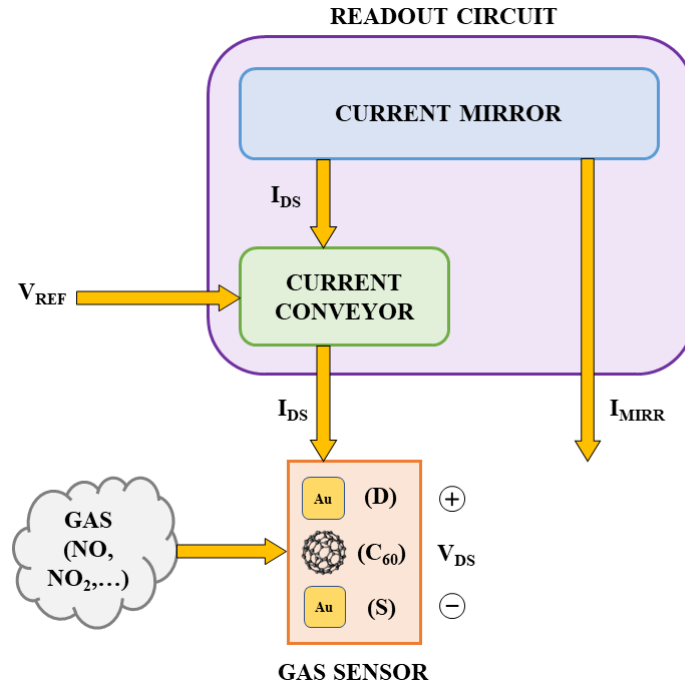


Figure 3.1: Block scheme of the readout circuit connected to the  $C_{60}$ -sensor.

To address the bias of the sensor and the proper flowing of the current, an operational amplifier (op-amp) and an n-type MOSFET are used, as shown in Figure 3.2.

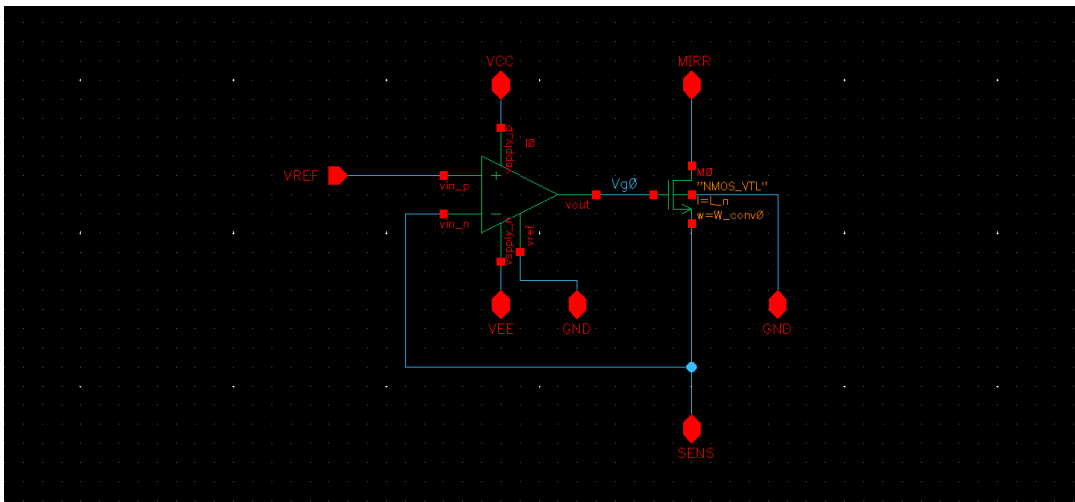
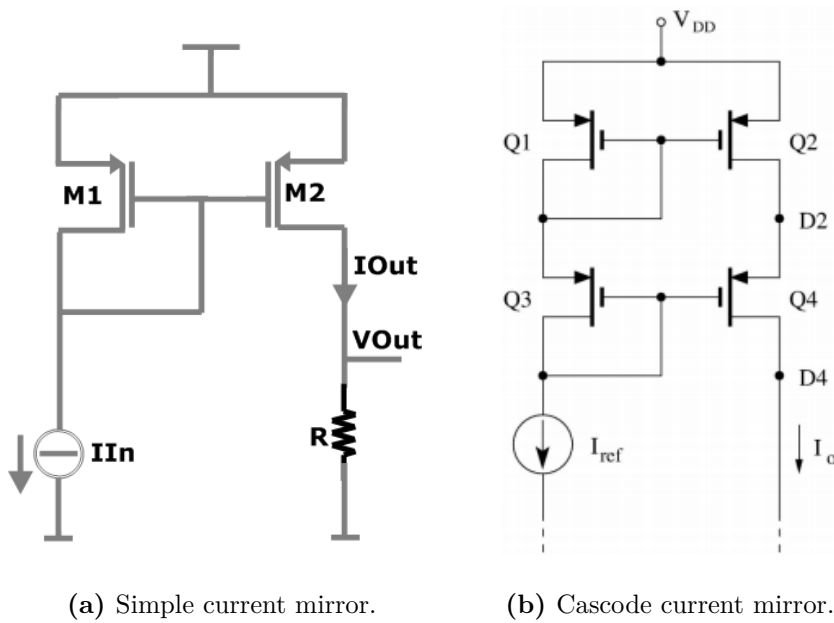


Figure 3.2: Current conveyor (implementation in Cadence Virtuoso).

The output of the op-amp is connected to the gate of the n-MOS so that it can be driven in saturation region. In order to both bias the sensor and let the current flow through it, the negative input of the op-amp is connected to the source of n-MOS and to sensor itself. In this way, the loop of op-amp is closed and in the ideal case, when the inputs of the op-amp are short-circuited, the constant input voltage ( $V_{REF}$ ) is imposed to the drain terminal of the sensor. Then, a current ( $I_{DS}$ ) flows in the sensor and it goes by the n-MOS to be “replicated” by the current mirror.

### 3.1.2 Current mirror

A current mirror is one of the most exploited blocks in analog electronics design [64]. Its aim is to “reflect” or modulate a reference current into another branch of the circuit [65]. There are many variants of a current mirror and, according to their characteristics, they can be matched to find out the most appropriate solution to employ in the circuit. Out of the numerous circuit configurations proposed in works like [66] and [67], the simple current mirror and the cascode current mirror are the most significant ones and are shown in Figure 3.3.



**Figure 3.3:** Configurations of current mirrors.

Firstly, the simple current mirror consists in the connections of two MOSFETs ( $M_1$  and  $M_2$ ) that have to be polarized in saturation region. The one placed in the reference branch of the circuit is in diode configuration, i.e. the drain and gate

terminals are connected, so that  $V_{SD,1} = V_{SG,1}$ . In this way,  $M_1$  works in saturation region and the current that flows through it is expressed in Equation 3.1:

$$I_{ref} = \frac{\mu_p C_{ox}}{2} \left( \frac{W}{L} \right)_1 (V_{SG,1} - V_{TH,1})^2 (1 + \lambda_p V_{SD,1}) \quad (3.1)$$

where  $\mu_p$  is the mobility of free-charge carriers in p-MOS (i.e. holes),  $C_{ox}$  is the gate oxide capacitance,  $W$  and  $L$  are respectively the width of the MOS active area and the channel length,  $V_{TH,1}$  is the threshold voltage and  $\lambda_p$  is the channel length modulation parameter in p-MOS.

In order to have the same current also in the output branch of the circuit, the gate and source terminals of  $M_1$  and  $M_2$  are connected, for which  $V_{SG,1} = V_{SG,2}$ . Assuming that their technological and geometrical parameters ( $\mu_p$ ,  $C_{ox}$ ,  $V_{TH}$  and  $W/L$ ) are the same, the gain of the simple current mirror is equal to:

$$\frac{I_{out}}{I_{ref}} = \frac{\left( \frac{W}{L} \right)_2}{\left( \frac{W}{L} \right)_1} \cdot \frac{(1 + \lambda_p V_{SD,2})}{(1 + \lambda_p V_{SD,1})} \quad (3.2)$$

The ratio of  $(W/L)_1$  and  $(W/L)_2$ , i.e. the aspect ratios of the two MOSFETs, represents the nominal gain of the simple current mirror. It is affected by the so called mirroring mismatch error that is due to the channel length modulation effect since  $V_{SD,1} \neq V_{SD,2}$ . As a result, the output current  $I_{out}$  as function of  $V_{SD,2}$  deviates significantly from the working point fixed by  $I_{ref}$ . This is due to the finite and small value of the output resistance of the current mirror that, instead, has to be as high as possible [66].

In order to get rid of this effect, the cascode current mirror can be introduced. In this case, other two MOSFETs ( $M_3$  and  $M_4$ ) are added in the circuit, as shown in Figure 3.3. If they are properly biased so that  $V_{SG,3} = V_{SG,4}$ , the mismatch mirroring error in Equation 3.2 is cancelled out and the current gain of the mirror is equal to its nominal value. In addition, an advantage of this solution is that the output resistance of the mirror is improved with respect to the case of simple current mirror. In fact, the behaviour of  $I_{out}$  around the working point imposed by  $I_{ref}$  is “flatter” than the previous case [66].

For these reasons, the choice of the current mirror to insert in the readout circuit of the analog front-end of this application fell on the cascode configuration. The implementation of this block in Cadence Virtuoso is depicted in Figure 3.4.

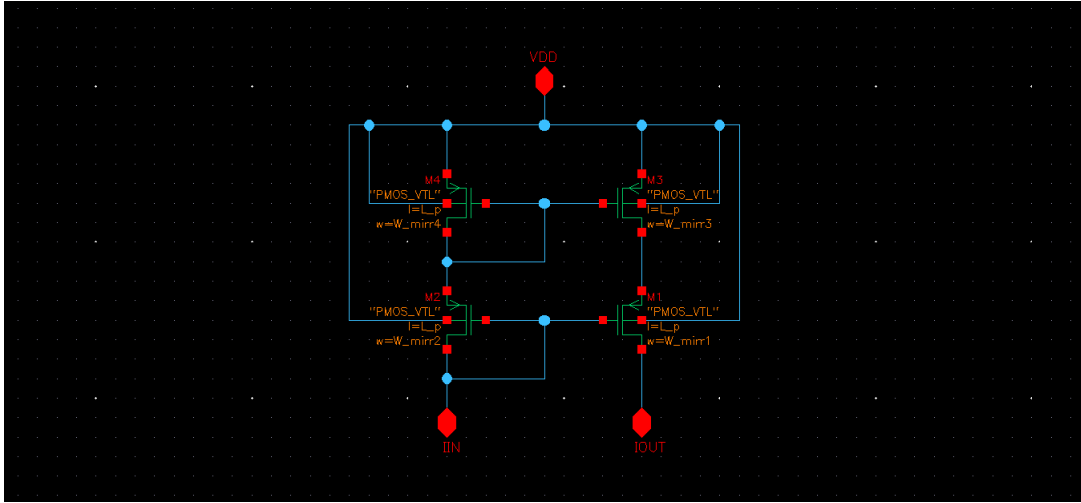


**Figure 3.4:** Current mirror (implementation in Cadence Virtuoso).

### 3.1.3 Simulation of the readout circuit

Once the two blocks of the readout circuit have been described, the current conveyor and the current mirror can be connected so that the electrical behaviour of the readout circuit itself can be tested in the simulation environment of Cadence Virtuoso. In Figure 3.5 the implementation of the readout circuit is shown.

Since the  $C_{60}$ -sensor has to work in amperometric mode, the first constraint that must be met is its correct biasing by imposing a constant voltage between the electrodes of the sensor (see Subsection 2.3.1). As mentioned in Subsection 3.1.1, in this configuration the current conveyor is used as a buffer to impose  $V_{DS} = V_{REF}$ . In particular, the value of the input voltage  $V_{REF}$  has to be compliant with the range used in the characterization of the sensor which is equal to  $[0, 2]$  V. Then, the voltage  $V_{DS}$  should “follow”  $V_{REF}$  over the whole range. In order to verify the proper functioning of the readout circuit, a DC analysis has to be performed by varying the  $V_{REF}$  voltage.

A constant input voltage  $V_{CTRL}$  - which “emulates” the presence of a gas target (see Subsection 2.2.3) - will be imposed to the model of the  $C_{60}$ -sensor like it was continuously exposed to a specific gas target. Doing that, there will be a clear view of its I-V trans-characteristic and the current that is mirrored in the output branch will be better appreciated.

In addition to  $V_{REF}$  and  $V_{CTRL}$ , the supply voltages  $V_{CC}$  and  $V_{DD}$  are two input voltages that influence the functioning of the circuit. The former is the positive power supply of the op-amp, whereas the latter is the supply voltage of the whole front-end circuit.

In this analysis, the positive power supply  $V_{CC}$  of the op-amp has to be tuned to

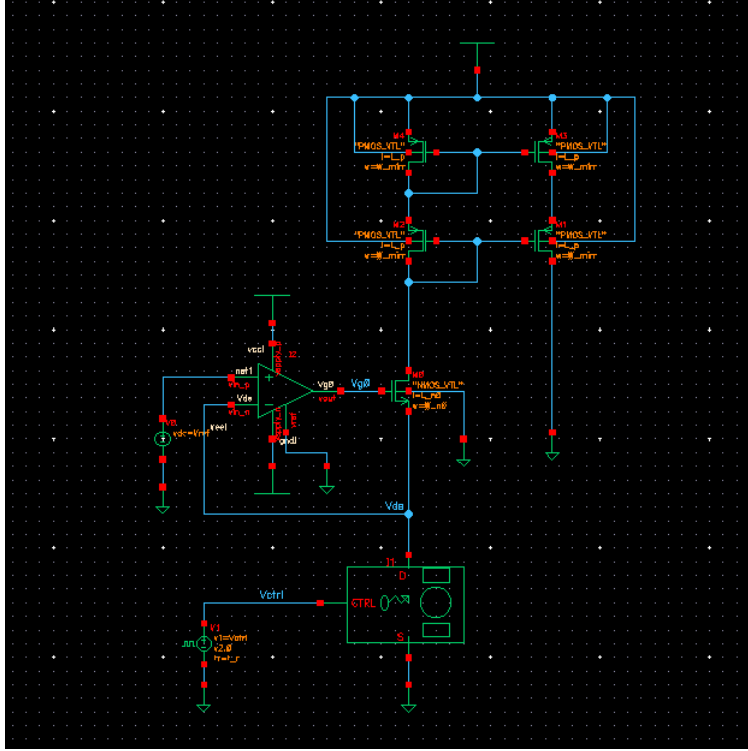


Figure 3.5: Readout circuit (implementation in Cadence Virtuoso).

have the proper behaviour of the current conveyor.

Notice that  $V_{DD}$  supplies the branch of the readout circuit that is connected to the  $C_{60}$ -sensor. According to the biasing requirements, the maximum voltage to be guaranteed across the sensor is equal to 2 V. Therefore, the value of  $V_{DD}$  must be greater than 2 V. Then, I have fixed  $V_{DD} = 3$  V as design parameter. In this way, there is a margin for the correct biasing of the sensor. Besides, the residual voltage in that branch is divided across the terminals of the MOSFETs that are connected to that branch of the readout circuit.

The MOSFETs that are present in the circuit have been preliminarily defined as large-sized devices, i.e. with great values of the width of the active area ( $W$ ) and of the channel length ( $L$ ). In this way, the short channel effects - that affect the MOSFETs with reduced sizes - can be neglected [46]. In particular, I have fixed  $W = 15 \mu\text{m}$  and  $L = 1 \mu\text{m}$ . Later, these geometrical parameters will be optimized in order to obtain a smaller area occupation and to make the overall front-end compliant with the nanometric dimensions of the  $C_{60}$ -sensor.

### Voltages in the current conveyor

The plots in Figure 3.6 represent the behaviour of the voltage across the sensor ( $V_{DS}$ ) and of the gate voltage of  $M_0$  ( $V_{G,0}$ ) as function of the input voltage  $V_{REF}$ , with a parametric sweep of  $V_{CC}$ . For the following simulations, the main examples will be referred to the case in which the sensor is not exposed to any gas, i.e. for  $V_{CTRL} = 0$ .

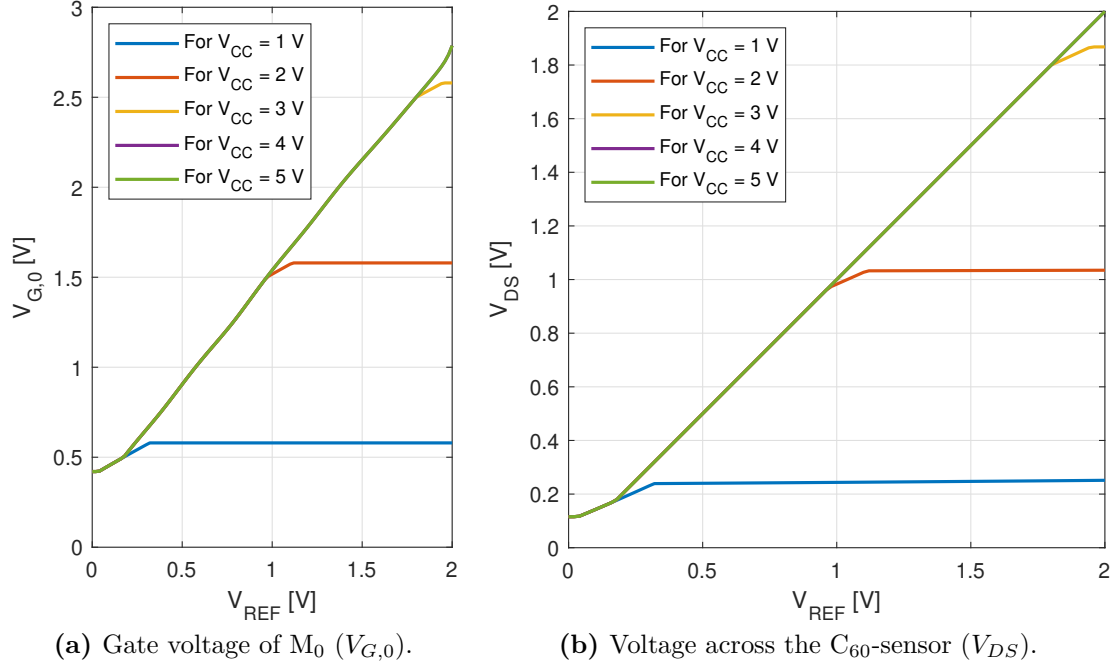


**Figure 3.6:** Voltages of the current conveyor for different values of  $V_{CC}$ .

The behaviour of both  $V_{DS}$  and  $V_{G,0}$  is influenced by the value of  $V_{CC}$ . In addition, the Verilog model of the op-amp is important for the choice of its positive power supply. In particular, the voltage  $V_{G,0}$  - which coincides with the output voltage of the op-amp - increases linearly as  $V_{REF}$  increases. Then, after a certain value of the input voltage,  $V_{G,0}$  saturates to a value which is equal to:

$$V_{G,0,sat} = V_{CC} - V_{sat}$$

where  $V_{sat} \approx 420$  mV. This value is obtained according to the model of the op-amp, defined in the library *ahdLib* in Cadence Virtuoso.

In order to have the proper functioning of the readout circuit, for all the input voltage range,  $V_{G,0}$  and  $V_{DS}$  have to increase linearly with  $V_{REF}$ . For  $V_{CC} \leq 3$  V, the voltages of interest saturate once  $V_{REF}$  overcomes certain values. Then, the

value of  $V_{CC}$  has to be greater than 3 V. In this case, I have chosen  $V_{CC} = 5$  V to have a good margin for the correct functioning of the current conveyor.

### Currents in the current mirror

Once the sensor has been properly biased by imposing  $V_{DS} = V_{REF}$ , some considerations about the analysis of the currents that are involved in the readout circuit can be made. In Figure 3.7 they are shown as functions of the input voltage  $V_{REF}$ .

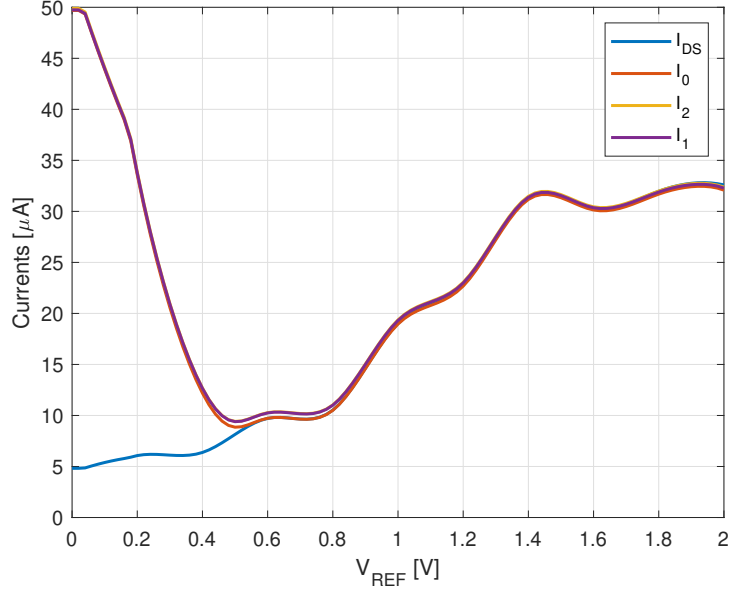


**Figure 3.7:** Currents in the readout circuit (for  $W = 15$   $\mu$ m and  $L = 1$   $\mu$ m).

The current that flows through the gas sensor is labelled as  $I_{DS}$ . Then, the currents  $I_0$ ,  $I_2$  and  $I_1$  are driven respectively by  $M_0$ ,  $M_2$  and  $M_1$ . The last one is the output current of the cascode mirror that will be put in input to the current-to-frequency converter.

In this configuration, the current mirror has been designed to have a 1:1 ratio, i.e. the aspect ratios of the MOSFETs are the same for all the elements. As can be observed, the currents  $I_0$ ,  $I_2$  and  $I_1$  “follow” the behaviour of  $I_{DS}$  for values of  $V_{REF}$  greater than around 0.5 V. This is due to the fact that  $M_0$  starts conducting when the input voltage is around that value. The model of the n-MOSFETs used in this project are characterized by a low threshold voltage, whose nominal value is equal to  $V_{TH} = 0.322$  V.

Considering the input voltage  $V_{REF} = 0.5$  V, the n-MOSFET  $M_0$  results to be in ON state:

$$V_{GS,0} = V_{G,0} - V_{DS} > V_{TH} \quad (3.3)$$

The values of  $V_{G,0}$  and  $V_{DS}$  can be extracted from Figure 3.7 and are equal to:

$$\begin{aligned} V_{G,0} &= 0.905 \text{ V} \\ V_{DS} &= 0.5 \text{ V} \end{aligned}$$

Substituting in Equation 3.3:

$$V_{GS,0} = 0.405 \text{ V} > V_{TH} = 0.322 \text{ V}$$

Then, the readout circuit has been proved to work as expected.

Nevertheless, the sizing of the MOSFETs that make up the first stage of the front-end has to be justified in order to provide a coherent description of the currents' behaviour in the DC analysis. The Verilog model used in this thesis work refers to the *BSIM4* library in Cadence Virtuoso. I have started considering a channel length ( $L$ ) equal to  $1 \mu\text{m}$ , for both n-MOS and p-MOS elements. Then, I have varied the value of the width  $W$  with a parametric sweep. In Figure 3.8 the behaviour of the output current of the mirror  $I_1$  is shown for different values of  $W$ .

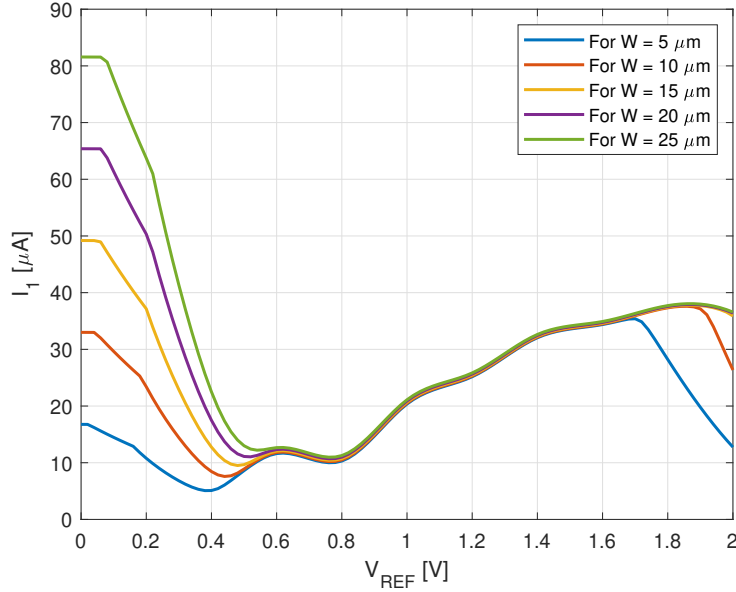


**Figure 3.8:** Output current  $I_1$  for different values of  $W$ .

There can be observed that, for  $W < 15 \mu\text{m}$ , the output current deviates from the current flowing in the sensor for high values of  $V_{REF}$ . This mismatch might cause an incorrect conversion in the frequency domain that would lead to a misguided gas recognition when the sensor is polarized with such values of  $V_{REF}$ . On the contrary, for  $W \geq 15 \mu\text{m}$  the behaviour of  $I_1$  fits with  $I_{DS}$  for values that are useful

for the polarization of the sensor. In addition, the smaller  $W$ , the more reduced is the value of  $I_1$  for small values of  $V_{REF}$ . Therefore, the power consumption - which has to be as low as possible - reduces by scaling-down the size of the MOSFETs in the readout circuit. So, in order to have the best trade-off between accuracy of current mirroring and power consumption, I fixed the width of the MOSFETs equal to  $15\ \mu\text{m}$ .

This analysis has been carried on considering large-sized elements in order to individuate the optimal aspect ratio of the MOSFETs, in this case  $(W/L) = 15/1$ . Nevertheless, the  $C_{60}$ -based gas sensor requires to be interfaced to a conditioning circuit that could minimize as much as possible the area occupation while maintaining the accuracy in the polarization and the successive conversion in frequency domain.

For these reasons, I have scaled down the size of all MOSFETs by a x10 factor, but still keeping their aspect ratio unchanged. In particular, with a channel length  $L = 100\ \text{nm}$  this architecture is consistent with the solutions of interfacing circuits present in literature [42], [43], [44], [45] (see Subsection 1.2.2). In Figure 3.9 the behaviours of the currents involved in the first stage of the analog front-end with small-sized MOSFETs are depicted.

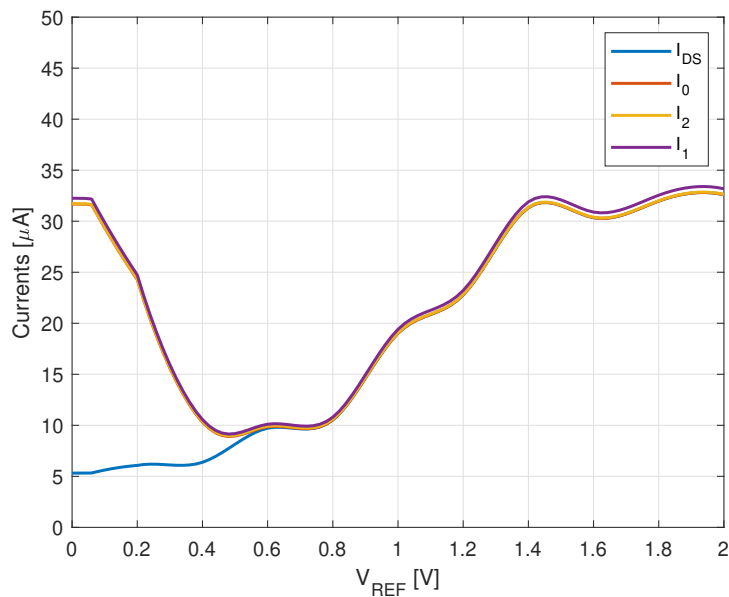


**Figure 3.9:** Currents in the readout circuit (for  $W = 1.5\ \mu\text{m}$  and  $L = 0.1\ \mu\text{m}$ ).

As can be noticed, for small values of  $V_{REF}$  the value of the currents in the current mirror has significantly reduced with respect to the previous case (see Figure 3.7). Still, for  $V_{REF} > 0.6\ \text{V}$ , the currents  $I_0$ ,  $I_2$  and  $I_1$  follow the behaviour of the current  $I_{DS}$ . Hence, the scaling-down of MOSFETs sizes has not affected the

functioning of the readout circuit. Actually, this approach allows to minimize the power consumption and the area occupation of the overall circuit.

### Currents in time domain

The correctness of the polarization in DC domain allows to focus the attention on the behaviour in time of the current that carries the information about the “identity” of the gas detected by the  $C_{60}$ -sensor. By polarizing the sensing device in amperometric mode - by imposing a constant value of  $V_{REF}$  - there can be simulated the detection of different gas targets in successive time phases. According to the sensing capabilities of the  $C_{60}$ -based device (see Subsection 2.2.3), the value of the input voltage  $V_{REF}$  has to be such that the detection of the gas targets can be effective. As an example, by applying  $V_{REF} = 1\text{ V}$ , gases like NO and  $\text{NO}_2$  can be distinguished from common atmospheric gases (e.g. Ar, CO,  $\text{CO}_2$  etc.).

For example, to emulate the sensing of two different targets, the model of the sensor is stimulated by the voltage  $V_{CTRL}$  that, for a sake of simplicity, behaves like a squared-wave signal in time. This approximation can be made under the assumption that the response of the  $C_{60}$ -sensor is instantaneous. This means that the time that a gas molecule takes to approach the sensor is much shorter than the total interaction time. In other words, the model of the sensor provides a very fast response to the exposure of gas targets. To complete the description of the sensor, additional analysis should be performed involving the study of its dynamics. In absence of this type of information, the aforementioned hypothesis are valid in this context.

Regarding the control voltage signal described above, two phases can be distinguished in the two semi-periods:

1. the sensing of a common a atmospheric gas, for example Ar (encoded with  $V_{CTRL} = 3\text{ V}$ );
2. the sensing of a gas target, for example NO with “N down” orientation (encoded with  $V_{CTRL} = 19\text{ V}$ ).

These phases are characterized by a constant voltage value that corresponds to a continuous exposure of the sensor to a specific gas target. The interaction between the sensor and the compound nearby is expected to be short, so it has been chosen in the order of nanoseconds (in this case, each phase lasts 25 ns). As a consequence, the currents under interest (i.e. the one flowing through the sensor and the one that is output of the current mirror) acquire constant values in each of the aforementioned phases.

In Figure 3.10 the evolution in time of the  $V_{CTRL}$  signal and the currents  $I_{DS}$  and  $I_1$  is shown.

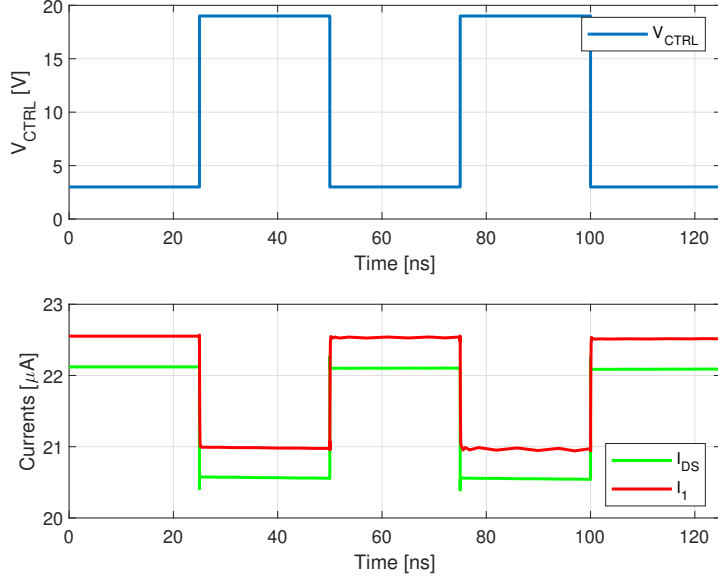


**Figure 3.10:** Time evolution of sensor’s control voltage  $V_{CTRL}$  and of the currents  $I_{DS}$  and  $I_1$ .

As can be noticed, the change in the control voltage value corresponds to a variation in the current that flows through the sensor (in green). Consequently, the mirrored current (in red) follows its behaviour. Then, the average values of the currents can be acquired in the two different phases. In this case, they are equal to:

$$I_{DS} = \begin{cases} 22.1203 \mu A, & \text{when } V_{CTRL} = 3 V \\ 20.5562 \mu A, & \text{when } V_{CTRL} = 19 V \end{cases} \quad (3.4)$$

$$I_1 = \begin{cases} 22.5518 \mu A, & \text{when } V_{CTRL} = 3 V \\ 20.9764 \mu A, & \text{when } V_{CTRL} = 19 V \end{cases} \quad (3.5)$$

The plots in Figure 3.10 show also that an error in the mirroring is occurring. Consequently, there is an “offset” in the current of about 400 nA. Nevertheless, this indication is not an issue for the successive conversion. In fact, since this error is constant all over the considered time window, this offset in current can be corrected later by the instrument that is supposed to acquire the corresponding frequency. In addition, in order to get rid of this error, the difference between the value of the current in presence of the gas target (in this case, NO) and the value assumed when there is the atmospheric gas (i.e. Ar) can be calculated. Therefore, the recognition of the gas will consider the difference in frequency of the two exposure phases. In this way, the offset due to the mirroring is cancelled out and the modulation of the current in the two phases is maintained.

The proposed simulations have proved to be consistent with the purpose of the readout circuit. So, the next step is to provide a characterization of the current-to-frequency converter.

## 3.2 Current-to-frequency converter

Once the  $C_{60}$ -based sensor is properly biased and the current that flows through it is mirrored in the output branch of the readout circuit, the output current has to be manipulated to extract the information about the “identity” of the gas target. The recognition of the gas that the sensor intercepts has to be as reliable as possible. Then, the indication provided by the measure at the output of the analog front-end needs to have a good degree of accuracy. The response of the sensor, based on the I-V trans-characteristics of the sensor, has highlighted that the direct acquisition of values of the current is not accurate for this application (see Subsection 2.2.3). As an alternative approach, the current can be converted into frequency since it is a quantity that can be easily measured with high accuracy. Therefore, a current-to-frequency converter has been implemented. In particular, it provides an output signal given by a periodic pattern of spikes. Then, the frequency of this “train” of spikes represents the signature that permits to discriminate the gas target among other compounds.

In literature, there are many works that propose solutions based on the design of circuits for the conversion of analog quantities into “events” (see Subsection 1.2.2). Even though works like [42], [43], [44], [45] use different signatures for the final recognition of gas targets, the approach for achieving this purpose is similar. Then, this thesis work will follow this trend by implementing a simplified i-to-f converter as proposed in the reference paper [68]. In Figure 3.11, the converter that will be integrated in the analog front-end is depicted.

The i-to-f converter consists of four main components:

1. An *integrating capacitor*, which implements a current-to-voltage conversion, so that it allows a relation between the current and the final frequency.
2. A *voltage comparator*, which matches the value of the voltage across the capacitor to a threshold. When it is overcome, the comparator generates a spike.
3. A *delay line*, which is useful to handle the timing of charge-discharge alternation of the integrating capacitor.
4. A *MOS-switch*, which permits the periodic charge and discharge of the integrator. It is controlled in feedback by the delayed spike pattern in output of the converter.

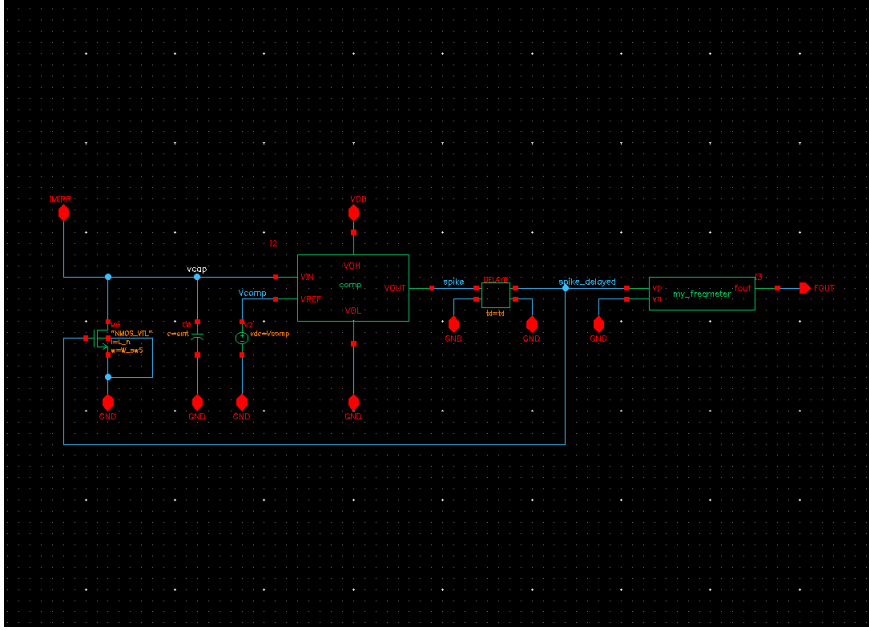


**Figure 3.11:** Current-to-frequency converter.

At the end of the implemented circuit, there is a functional block (named as *frequency meter*) that has the aim of measuring the frequency of the output spike pattern. It can be considered as a symbol representing, for instance, a measuring instrument like a microprocessor.

In order to have a comparison between the theoretical functioning of the implemented circuit and its actual behaviour, an analytic description has to be done. Applying the Kirchhoff's currents law at the input node of the converter, the input current  $I_{mirr}$  splits in two components, i.e. one flowing in the MOS-switch ( $I_{sw}$ ) and the other charging the integrating capacitor ( $I_{cap}$ ), so that:

$$I_{mirr} = I_{sw} + I_{cap} = \frac{v_{cap}}{r_{sw}} + C_{int} \frac{\partial v_{cap}}{\partial t} \quad (3.6)$$

The quantity of interest is the voltage across the integrating capacitor ( $v_{cap}$ ), so Equation 3.6 can be rewritten as follows:

$$\frac{\partial v_{cap}(t)}{\partial t} + \frac{v_{cap}(t)}{r_{sw} C_{int}} = \frac{I_{mirr}}{C_{int}} \quad (3.7)$$

It is a first-order differential equation. Imposing that at  $t_0 = 0$  the voltage across the capacitor is  $v_{cap}(t_0) = 0$ , the solution of Equation 3.7 is:

$$v_{cap}(t) = V_{\infty} \left( 1 - e^{-\frac{t}{\tau}} \right) \quad (3.8)$$

where  $\tau = r_{sw}C_{int}$  is the charging time constant and  $V_\infty = r_{sw}I_{mirr}$  is the maximum voltage value that can be reached in charging phase.

The presence of the comparator puts a limit to the rising of the capacitance voltage. In particular, when  $v_{cap}$  reaches the value of  $V_{comp}$ , the MOS-switch is driven to triode region. In this way the integration capacitor discharges to the low level voltage. To evaluate the time interval of the charging phase up to  $V_{comp}$ , by imposing  $v_{cap} = V_{comp}$ , the charging period of the capacitor can be obtained from Equation 3.8:

$$\Delta t = \tau \ln\left(\frac{V_\infty}{V_\infty - V_{comp}}\right) \quad (3.9)$$

When the threshold ( $V_{comp}$ ) is reached, the comparator will provide the high logic value at the output. Since in the real case the discharge of the integration capacitor is not instantaneous, a delay block at the output of the comparator is needed. This block introduces a delay ( $t_d$ ) that lengthens the time of the spike signal that controls the switch in the feedback path. As soon as the delay is extinguished, a retarded spike signal is generated at the output of the delay line. It drives the switch for the discharge of the capacitor and it acts as the output signal for the final frequency measurement. When also the delayed spike signal is ended, the switch is set off and another charging phase can begin again.

The presence of the delay line affects the period of the output signal. In particular two time contributions are introduced:

1. When  $v_{cap}$  overcomes  $V_{comp}$ , the spike signal is high. The delay line extends the spike in time of a quantity equal to  $t_d$ . In this time interval  $v_{cap}$  keeps increasing.
2. Once the spike signal expires, the retarded spike signal is generated and drives the switch to the OFF state. Also in this case, this signal has a duration equal to  $t_d$ .

Then, taking into account the delay line in the i-to-f converter, Equation 3.9 needs to be corrected with a time term as follows:

$$\Delta t_{out} = \tau \ln\left(\frac{V_\infty}{V_\infty - V_{comp}}\right) + 2t_d \quad (3.10)$$

Since the frequency of the output signal is the quantity of interest as signature for the acknowledgement of the gas, it can be calculated as:

$$f_{out} = \frac{1}{\Delta t_{out}} = \left[ \tau \ln\left(\frac{V_\infty}{V_\infty - V_{comp}}\right) + 2t_d \right]^{-1} \quad (3.11)$$

In the ideal case, the equivalent resistance of the switch when it is in the OFF state is infinite. The capacitor voltage increases linearly in time and proportionally to  $I_{mirr}$ . As a consequence, the output frequency results to be proportional to the current provided by the current mirror.

In mathematical terms, the charging time constant is considered to be very large (i.e.  $t \ll \tau$ ). So, Equation 3.8 can be simplified exploiting the Taylor series of exponential term:

$$e^{-\frac{t}{\tau}} = 1 - \frac{t}{\tau} + \dots$$

By truncating the approximation at the first order, the expression of the voltage across the integrating capacitor becomes:

$$v_{cap}^{(id)}(t) = \frac{I_{mirr} \cdot t}{C_{int}} \quad (3.12)$$

The signal that is generated by the comparator (i.e. the spike pattern) has a period equal to:

$$\Delta t^{(id)} = \frac{C_{int} V_{comp}}{I_{mirr}} \quad (3.13)$$

Taking into account the delay introduced by the delay line, the period of the output spike pattern signal is equal to:

$$\Delta t_{out}^{(id)} = \frac{C_{int} V_{comp}}{I_{mirr}} + 2t_d \quad (3.14)$$

At the end, the frequency of the output signal results to be equal to:

$$f_{out}^{(id)} = \frac{1}{\Delta t_{out}^{(id)}} = \left[ \frac{C_{int} V_{comp}}{I_{mirr}} + 2t_d \right]^{-1} \quad (3.15)$$

In this analysis, the non-idealities of the op-amp (e.g. offset, slew rate etc.) are being neglected to simplify the model of the i-to-f converter.

### 3.2.1 Simulation of current-to-frequency converter

Before the complete simulation of the analog front-end can be performed, the i-to-f converter needs to be validated in its functioning.

The quantity that acts as input for the converter is the output current of the readout circuit. As aforementioned in Subsection 3.1.3, the sensor is controlled by a square-wave signal, so that the current that flows through it - and, consequently, the current in the output branch of the cascode mirror - could follow the shape of the input control voltage  $V_{CTRL}$  (see Figure 3.10). Then, the current that enters

the i-to-f converter results to be constant in different gas exposure phases. The aim of the converter is to provide a corresponding value of frequency that has to be constant in each of the phases of the input current, according to the different values of the current itself. The acquisition of the output frequency requires a multiple alternation in switching of the MOSFET in the converter. When the logical value of the spike pattern at the output is low, the MOSFET is in OFF state. On the other hand, to drive the MOS-switch in triode region (i.e. in ON state), the high logical value of the comparator - that goes to the MOSFET gate - has been put equal to  $V_{CC} = 3\text{ V}$ .

The MOS-switch has been sized as the MOSFETs in the readout circuit. In particular, its geometrical parameters are equal to  $W = 1.5\text{ }\mu\text{m}$  and  $L = 100\text{ nm}$ . Then, the integrating capacitor can be charged and discharged periodically, so that a triangular-wave signal  $v_{cap}$  can be generated. Each triangle corresponds to a single charge-and-discharge cycle of the integrating capacitor. At the output, the frequency meter acquires the value of the spike pattern's time-period and converts it into a frequency value as in Equation 3.11. According to its Verilog description, the frequency of the output signal is detected by measuring the difference between two successive zero-crossings. So, in correspondence of each phase of the input current, there should be at least two spikes generated by the voltage comparator, so that the value of the output frequency could be acquired.

Doing that, the final achievement is the association of a measured physical quantity, i.e. the frequency, to a gas target that has been detected by the  $C_{60}$ -based sensor.

### Setting of simulation

To validate the correct behaviour of the i-to-f converter, the input current has to emulate the one at the output of the readout circuit. In this case, I have instantiated a current source that generates a square-wave with the same period of the  $V_{CTRL}$  signal in Figure 3.10. The current signal takes into account the case analyzed in the Subsection 3.1.2, characterized by two phases with values of current as in Equation 3.5.

Considering an arbitrary comparator's threshold voltage  $V_{comp}$  and being known the current  $I_1$  in the two phases (in the order of tens of  $\mu\text{A}$ ), the integrating capacitance ( $C_{int}$ ) can be extracted according to Equation 3.13. As first approximation, the value of  $C_{int}$  that is obtained will allow one charging cycle. Since the charge of the capacitor occurs in two phases, the current that must be considered for the sizing has to be the greatest one.

Assuming a current signal with a semi-period equal to 25 ns and considering the maximum current in the case analyzed in the Subsection 3.1.2 (i.e. 22.5518  $\mu\text{A}$ ), the maximum value of the integrating capacitance that can be charged up to  $V_{comp} = 1\text{ V}$  is equal to:

$$C_{int,max} = \frac{\Delta t \cdot I_{1,max}}{V_{comp}} = \frac{25 \cdot 10^{-9} [s] \cdot 22.5518 \cdot 10^{-6} [A]}{1 [V]} \approx 564 \text{ fF} \quad (3.16)$$

In this case, I have chosen  $C_{int} = 500 \text{ fF}$ .

Another important parameter is the time  $t_d$  introduced by the delay line to let the capacitor discharge by means of the MOS-switch. This has to be set to a value that has to be as short as possible so that the capacitor can start the next charging cycle. In the first simulation, it has been set equal to  $t_d = 1 \text{ ns}$ .

The evolution in time of the quantities of interest involved in the i-to-f converter are depicted in Figure 3.12.

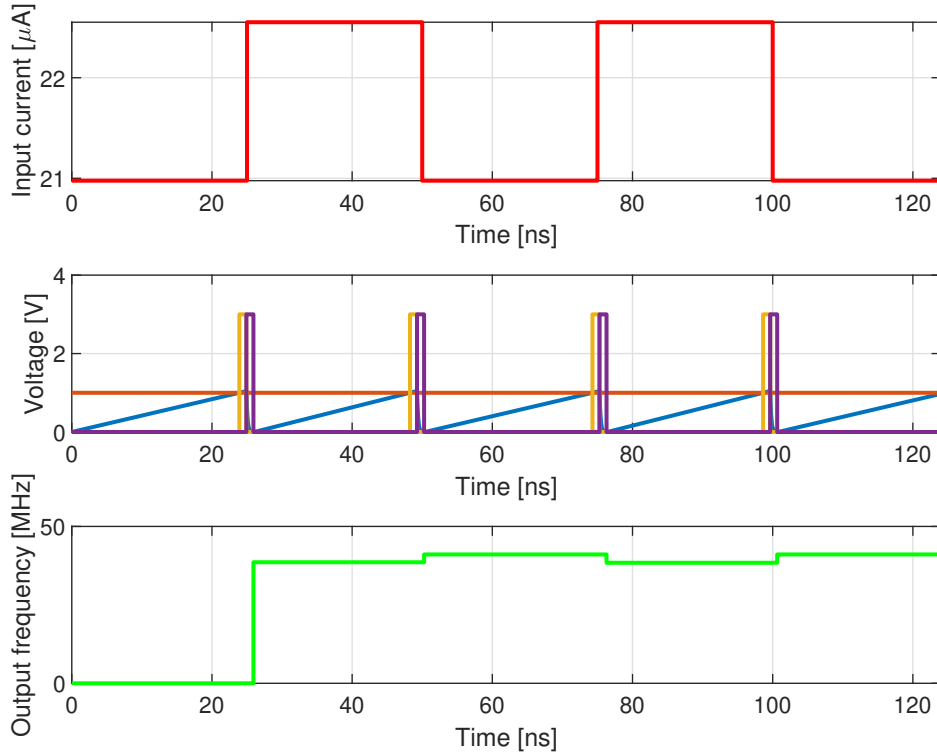


**Figure 3.12:** Evolution in time of the quantities of interest in the i-to-f converter, with  $C_{int} = 500 \text{ fF}$  and  $t_d = 1 \text{ ns}$ . Voltages:  $v_{cap}$  (blue),  $V_{comp}$  (orange),  $V_{spike}$  (yellow),  $V_{spike,delayed}$  (violet).

As can be noticed, the voltage  $v_{cap}$  across the integrating capacitor, when it is charged with constant current, has a triangular waveform. When  $v_{cap}$  becomes greater than  $V_{comp}$ , a spike with a width equal to  $1 \text{ ns}$  arises (in yellow). The discharge of the integrating capacitor occurs when the delayed spike is generated. Then, when this spike extinguish, the next charging phase begins.

However, the behaviour of the output frequency is not consistent with the evolution

of  $I_1$ . In fact, the frequency obtained in the phase with the higher value of the input current results to be lower than the one in the successive phase, where the current's value is higher. The expected behaviour should highlight the direct proportionality of the frequency to the value of the current, according to the Equation. So, the higher the current, the more rapidly the capacitor charges, i.e. the higher the output frequency.

This “phase shift” is due to the Verilog description of the frequency meter. In particular, the frequency of the  $V_{spike,del}$  is provided by considering two successive zero-crossings of the output signal. In fact, in the time interval  $[0, 25]$  ns the frequency results to be equal to zero since the second zero-crossing does not occur until the end of the first phase. Therefore, the frequency that has been measured in the first phase “falls” in the second one (i.e.  $[25, 50]$  ns), and so on.

Then, a different method should be implemented, as described in the next paragraph.

### Optimization of the converter's design

To get a constant frequency value that could be measured in the corresponding time interval of each phase, the charging phase has to be faster. Then, in a single phase, there will be multiple charging cycles. The more the charging cycles, the more precise the measurement of the output frequency. In this way, the behaviour of the voltage comparator could be effective according to its Verilog description. Having the same values of the input current in the same integration time, the design parameters that can be optimized are  $C_{int}$ ,  $V_{comp}$  and  $t_d$ . To achieve a faster charge of the integrator capacitor, all of them can be lowered.

For the sake of simplicity, the threshold voltage of the comparator can be kept constant to the previous value ( $V_{comp} = 1$  V). To fasten the charge-and-discharge cycle, there should be needed a smaller capacitor. For instance, the capacitance can be scaled down by a x10 factor, so imposing  $C_{int} = 50$  fF.

Also the delay time  $t_d$  can be made smaller, so that the discharge of the capacitor could be faster as well and that a major number of charging cycles in a single phase could be obtained. In this example, I have fixed  $t_d = 500$  ps.

In Figure 3.13 the simulation of the converter with optimized parameters is shown. The time evolution of the voltage signals highlights that a faster charge turns into a higher output frequency (in the order of hundreds of megahertz). Moreover, as aforementioned, the behaviour of  $f_{out}$  results to be coherent with the modulation of  $I_1$ . This is due to the increased number of charging cycles due to the decreased value of  $C_{int}$  and  $t_d$  that have optimized the measurement of the output frequency according to the Verilog model of the frequency meter block.

However, the first charging cycle of the first phase provides a higher frequency with respect to the value that stabilize in the next cycles. The reason why it behaves like this is that the first period of the  $v_{cap}$  signal is shorter than the successive

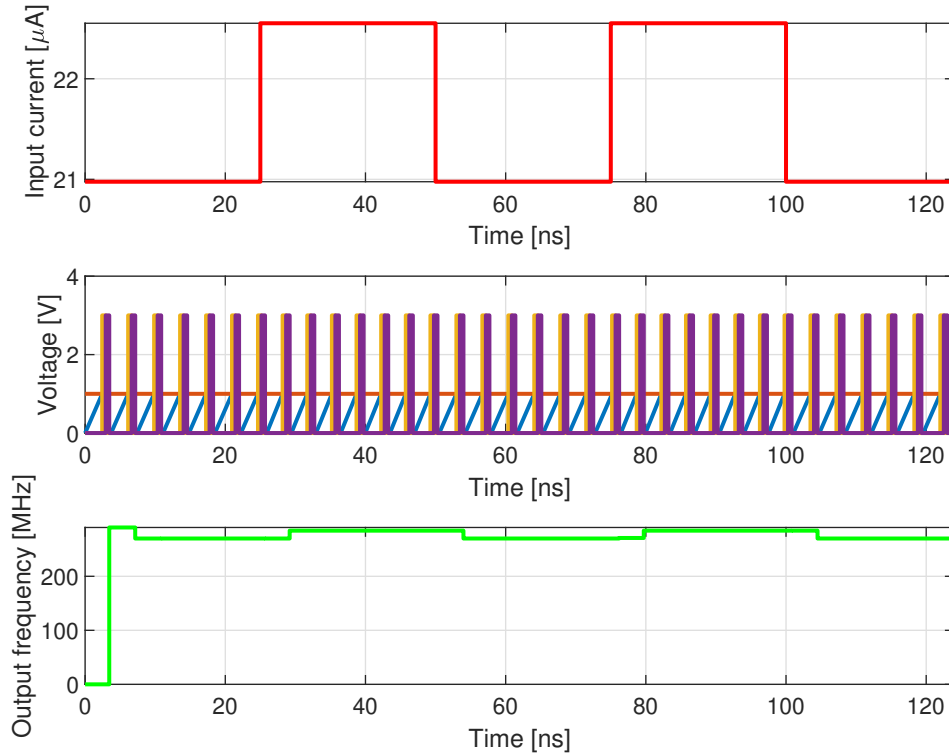


**Figure 3.13:** Evolution in time of the quantities of interest in the i-to-f converter, with  $C_{int} = 50$  fF and  $t_d = 500$  ps. Voltages:  $v_{cap}$  (blue),  $V_{comp}$  (orange),  $V_{spike}$  (yellow),  $V_{spike,delayed}$  (violet).

ones. In fact, the first triangle of the waveform crosses the 0 V and then it charges starting from a slightly negative voltage (in the order of few mV). Later, since the capacitor is charged at constant current, the period of the voltage across  $C_{int}$  - and consequently its frequency - assumes the correct value.

This “measurement error” causes a delay in the measurement of the output frequency for a time interval corresponding to one charging period of the integrating capacitor. Nevertheless, this issue is not such relevant for the final goal of the i-to-f converter since the frequency measurement is consistent to its mathematical model. In addition, in a post-processing stage, this little phase shift can be corrected.

At the end, also the current-to-frequency converter has proved to work properly. Therefore, it can be connected to the readout circuit in order to simulate the functioning of the whole analog front-end.

In the next chapter, all the cases of gas exposure of the  $C_{60}$ -sensor will be analyzed. A particular focus will be dedicated on the targets that the sensor has proved to be selective to (see Subsection 2.2.3). The values of the currents that are driven by the sensor will be matched to the values of the output frequency and the effectiveness

of the front-end will be evaluated.



## Chapter 4

# Simulation and validation of final results

In Chapter 3 the functioning of the analog front-end has been described by characterizing the readout circuit and the current-to-frequency converter separately. Firstly, the readout circuit connects directly to the  $C_{60}$  to bias it and to mirror the current that is driven when the gas exposure occurs. Secondly, the output current of the readout circuit is used as input of the i-to-f converter and provides the frequency of a spike pattern, implementing an conversion from analog domain to discrete domain. In this way, the correctness of their respective purposes have been proved. Then, they could be joined together in order to simulate and validate the implementation of the whole front-end.

In Figure 4.1 the complete structure of the circuit designed in this thesis work is depicted.

In this chapter, there will be simulated the exposure to the gas targets which the sensor is selective to, as described in Subsection 2.2.3. The first assumption to make is that the  $C_{60}$ -sensor is inserted in an environment where it senses the presence of only one atmospheric gas molecule (Ar, CO,  $CO_2$  etc.).

After a certain time interval, another molecule approaches to the sensing molecule ( $C_{60}$ ) and, according to the biasing conditions, the sensor is able to distinguish another type of target. The change in the detected gas causes a modulation in the current that flows through the sensor itself. Then, a difference of the current can be calculated as follows:

$$\Delta I_{DS} = I_{DS,tar} - I_{DS,atm} \quad (4.1)$$

where  $I_{DS,tar}$  is the current flowing in presence of the target of interest (in this case, NO or  $NO_2$ ) and  $I_{DS,atm}$  is the current that the sensor drives when it detects an atmospheric gas (Ar, CO,  $CO_2$  etc.).

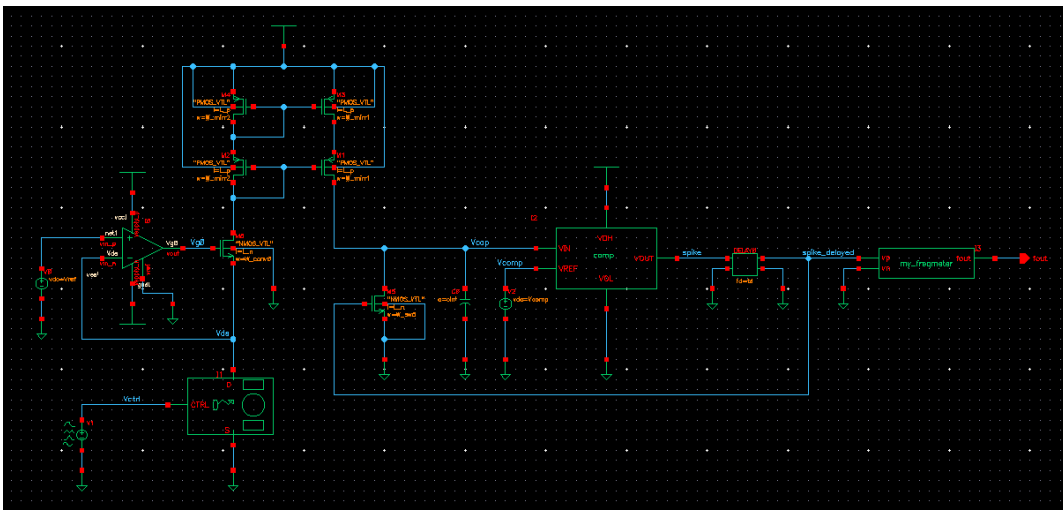


**Figure 4.1:** Analog front-end for  $C_{60}$  gas-sensor (implementation in Cadence Virtuoso).

Thanks to the implemented front-end, the modulation in current corresponds to a modulation in the measured frequency. The output of the interfacing circuit will be used to achieve the identification of the compound of interest by evaluating the difference between the measured frequencies, as expressed in the following equation:

$$\Delta f_{out} = f_{out,tar} - f_{out,atm} \quad (4.2)$$

where  $f_{out,atm}$  and  $f_{out,tar}$  are the frequencies obtained, respectively, before and after the gas target exposure.

In [57] the characterization of the device under analysis has proved that the C<sub>60</sub>-based molecular sensor is effective for the detection of gases like nitric oxide (NO) and nitrogen dioxide (NO<sub>2</sub>). In particular, the former one is detectable when the sensor is biased with  $V_{DS} = 1$  V, whereas the latter requires a biasing voltage included between 1.6 and 1.8 V. In this context, I have chosen to bias the sensor with  $V_{DS} = 1.7$  V for the detection of NO<sub>2</sub>.

Taking into account the characterization of the analog front-end (see Chapter 3), the emulation of the gas exposure and the biasing of the sensor will be implemented by varying the voltages  $V_{CTRL}$  and  $V_{REF}$ . Moreover, the simulations that will be shown in the next sections will be carried out with a circuit configuration including the values of the design parameters listed in Table 4.1.

Design parameter	Name of variable	Value
Circuit's power supply	$V_{DD}$	3 V
Positive power supply of the op-amp	$V_{CC}$	5 V
Gas exposure duration	$T_{ctrl}$	25 ns
Rise/Fall time of control voltage	$t_{r,f}$	1 fs
Width of n- and p-MOS	$W$	1.5 $\mu$ m
Length of n- and p-MOS	$L$	0.1 $\mu$ m
Integrating capacitor	$C_{int}$	50 fF
Comparator's threshold voltage	$V_{comp}$	1 V
Delay introduced by delay block	$t_d$	500 ps

**Table 4.1:** Fixed design parameters of the analog front-end.

In Table 4.2, the values of the current that the sensor drives when it senses the most common atmospheric gases are listed. Moreover, there are reported the values of frequency calculated by means of Equation 3.15, taking into account the values of parameters in Table 4.1.

Atmospheric gas	$V_{CTRL}$ [V]	For $V_{DS} = 1$ V		For $V_{DS} = 1.7$ V	
		$I_{DS,atm}$ [ $\mu$ A]	$f_{out,atm}$ [MHz]	$I_{DS,atm}$ [ $\mu$ A]	$f_{out,atm}$ [MHz]
Ar	3	22.1209	306.7197	39.8354	443.4265
CO	4	19.0702	276.0988	34.6089	409.0456
CO <sub>2</sub>	5	18.9117	274.4338	31.2343	384.4965
N <sub>2</sub>	6	18.4116	269.1298	34.3469	407.2100
H <sub>2</sub> O (“flat”)	7	18.4569	269.6134	30.7233	380.6001
H <sub>2</sub> O (“H down”)	8	19.4726	280.2918	31.5610	386.9619
H <sub>2</sub> O (“O down”)	9	18.1390	266.2058	31.6871	387.9082
O <sub>2</sub>	10	17.8455	263.0314	33.4887	401.1166

**Table 4.2:** Atmospheric gases: control voltages, input currents and output frequency values.

Since the combinations of the various cases are numerous, there will be shown some relevant simulations so that they can be analyzed. In this way, the correctness of the final implementation can be verified and potential drawbacks can be pointed out. At the end, the values of currents and frequencies of each case will be listed in tables so that a comparison can be made.

## 4.1 Exposure to nitric oxide (NO)

As mentioned in Subsection 2.2.3, the nitric oxide (NO) can be detected by the C<sub>60</sub>-based sensor when it is biased with  $V_{DS} = 1$  V. The values of the current that flows through the sensor and the corresponding output frequency calculated with Equation 3.15 are reported in Table 4.3.

Gas target	$V_{CTRL}$ [V]	$I_{DS,tar}$ [ $\mu$ A]	$f_{out,tar}$ [MHz]
NO (“O down”)	18	14.8183	228.6129
NO (“N down”)	19	20.4119	289.8928
NO (“flat”)	20	14.7329	227.5952

**Table 4.3:** Nitric oxide (NO): control voltages, currents and output frequencies (for  $V_{DS} = 1$  V).

There are three different cases according to the orientation of the gas target with respect to the sensing molecule of the conductive channel in the sensor. In particular, the orientation labelled as “down” indicates the atom of the target which is nearest to the C<sub>60</sub> molecule. On the contrary, the “flat” orientation points

out the equidistance of all the atoms to the channel axis. In Figure 4.2, the NO molecule is shown in the different positions with respect to the gas sensor.

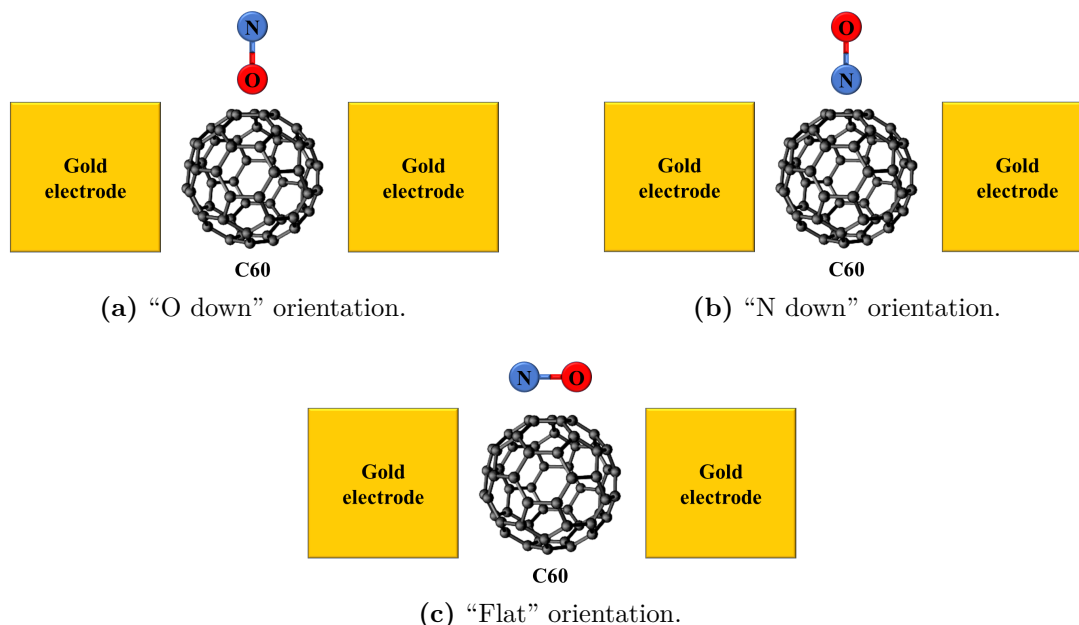


**Figure 4.2:** Orientations of nitric oxide (NO) with respect to  $C_{60}$ -sensor’s channel axis.

Among the different configurations of NO exposure, the case of “O down” orientation can be studied. As an example, this target can be detected after an Ar molecule. Then, to simulate the control voltage is varied from 3 V to 18 V in a time window of 75 ns subdivided in three phases:

1. For [0,25] ns, the sensor detects the presence of an Ar molecule.
2. For [25,50] ns, a gas target molecule of NO approaches to the device.
3. For [50,75] ns, the NO molecule gets away and the sensor restarts the sensing of the Ar molecule.

The quantities of interest for the study of the analog front-end are the current that flows through the sensor ( $I_{DS}$ ) and the output frequency ( $f_{out}$ ) in all the three phases. Then, the input and the output of the implemented circuit can be matched to verify the correctness of the model. In Figure 4.3 the time evolution of  $V_{CTRL}$ ,  $I_{DS}$  and  $f_{out}$  for this particular case is depicted.

The behaviour in time of the current and the output frequency is consistent with the model described in Chapter 3. A detail to notice is the presence of little glitches

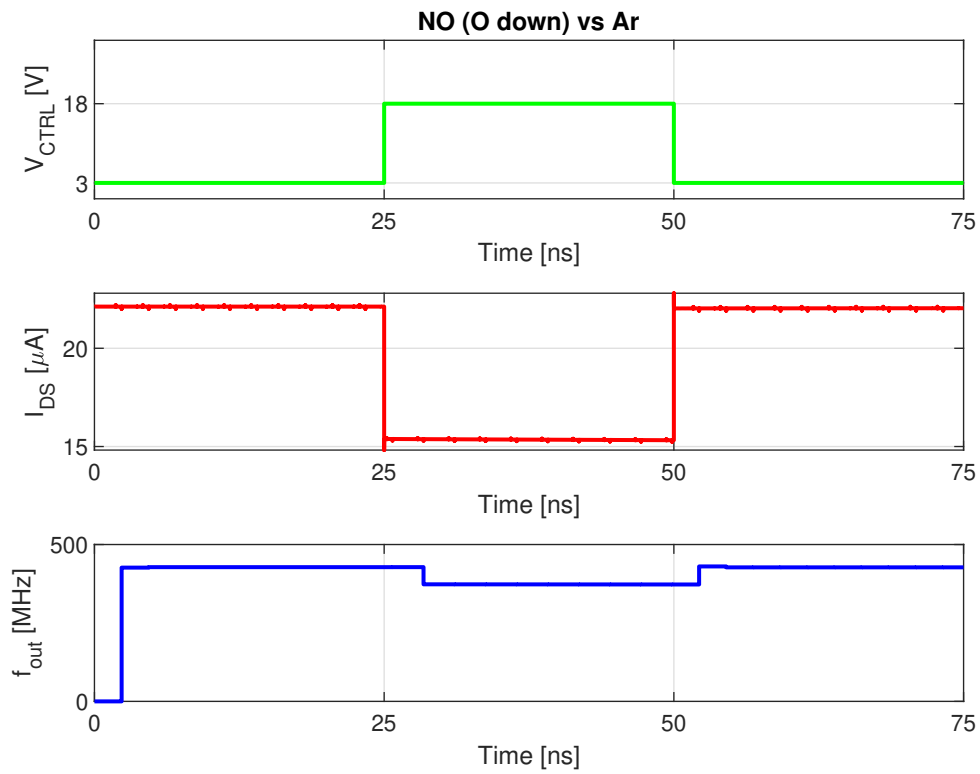


**Figure 4.3:** Exposure to Ar and NO (“O down”). Time evolution of control voltage ( $V_{CTRL}$ ), current ( $I_{DS}$ ) and output frequency ( $f_{out}$ ).

in the  $I_{DS}$  evolution. It is due to the switching of the n-MOS in the i-to-f converter and they occur in the time instant corresponding to the rise and fall edges of the output spike pattern signal.

Because of this little variations, the values of  $I_{DS}$  and  $f_{out}$  can be extracted by calculating the average value of the quantities of interest in the three phases:

$$I_{DS} = \begin{cases} 22.1147 \mu\text{A}, & \text{in } [0,25] \text{ ns time interval} \\ 15.3427 \mu\text{A}, & \text{in } [25,50] \text{ ns time interval} \\ 22.0341 \mu\text{A}, & \text{in } [50,75] \text{ ns time interval} \end{cases} \quad (4.3)$$

$$f_{out} = \begin{cases} 472.7196 \text{ MHz}, & \text{in } [0,25] \text{ ns time interval} \\ 372.8763 \text{ MHz}, & \text{in } [25,50] \text{ ns time interval} \\ 472.5170 \text{ MHz}, & \text{in } [50,75] \text{ ns time interval} \end{cases} \quad (4.4)$$

Notice that the value of current when the sensor detects the NO target molecule (in the second exposure phase) is different from the theoretical value reported in Table 4.3. This issue is due to an imprecise biasing of the drain-source voltage across the sensor. In Figure 4.4 the voltage across the sensor is shown.

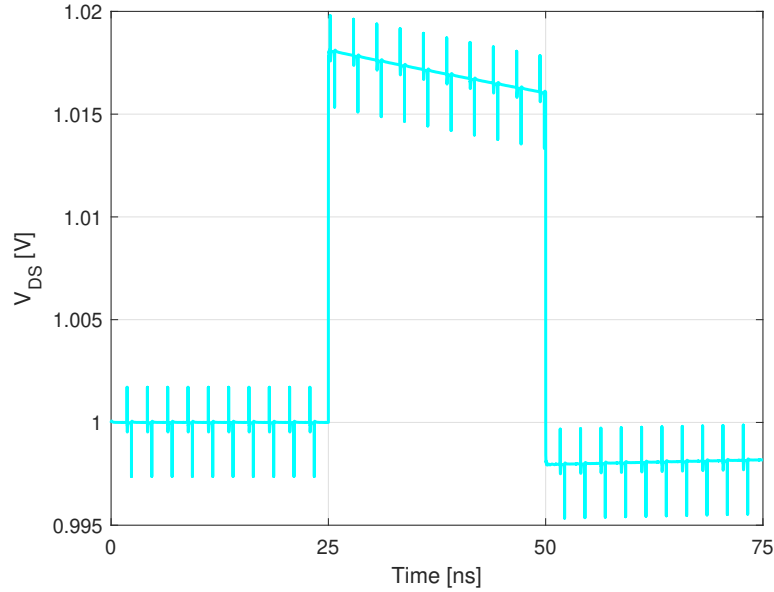


**Figure 4.4:** Exposure to Ar and NO (“O down”). Voltage across the  $C_{60}$  ( $V_{DS}$ ).

As can be observed, the voltage  $V_{DS}$  undergoes small variations in the three phases. Then, the current  $I_{DS}$  changes with respect to the nominal values. In fact, as seen in Chapter 2, the current that flows through the sensor changes significantly also for slight variations of the biasing voltage.

Another consideration involves the values of the output frequency. They result to

be higher than the theoretical values that are computed according to Equation 3.15. Under the ideal assumption that the current in the sensor is equal to the current that is in input to the i-to-f converter ( $I_{DS} = I_{mirr}$ ), the output frequency values of this specific case would be equal to:

$$f_{out,theor} = \begin{cases} 306.6600 \text{ MHz, in } [0,25] \text{ ns time interval} \\ 234.8036 \text{ MHz, in } [25,50] \text{ ns time interval} \\ 305.8843 \text{ MHz, in } [50,75] \text{ ns time interval} \end{cases} \quad (4.5)$$

Comparing the values in Equations 4.4 and 4.5, the gap between the simulation results and the theoretical values of output frequency is due to a faster charging of the integrating capacitor in the implemented circuit. The current that charges the integrating capacitor and the voltage across  $C_{int}$  are depicted in Figure 4.5.

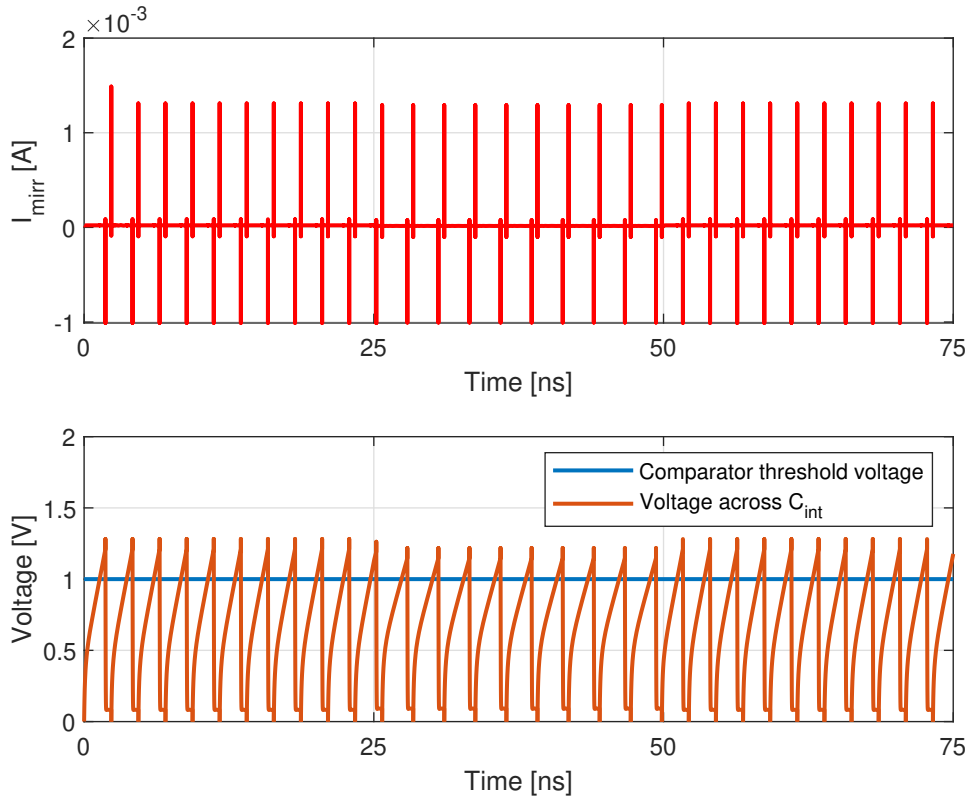


**Figure 4.5:** Exposure to Ar and NO (“O down”). Mirror current in input to the i-to-f converter ( $I_{mirr}$ ) and voltage across the integrating capacitor ( $v_{cap}$ ).

The behaviour of  $I_{mirr}$  shows the presence of peaks of currents corresponding to the transitions of the spike pattern signal at the output of the front-end. In particular, when the charging phase starts, there is a current injection of about mA that

increases rapidly the voltage  $v_{cap}$ . Once the current peak extinguishes, the value of the current stabilizes in the order of  $\mu\text{A}$  and assumes a constant value, according to the gas that the sensor detects. Then, the voltage across  $C_{int}$  increases linearly, as expected.

These considerations can be taken into account for future developments of this application, in order to enhance the performance of the analog front-end.

As for the case of Ar, there can be simulated the exposure of the  $C_{60}$ -sensor to an NO molecule against other atmospheric gases. In Table 4.4, the theoretical and measured values of the output frequency for all the combinations of gas exposures are listed.

Exposure to NO (“O down”) - $V_{tar} = 18\text{ V}$								
$V_{atm}$ [V]	Theoretical values		Simulation values					
	$\Delta I_{DS}$ [ $\mu\text{A}$ ]	$\Delta f_{out}$ [MHz]	Currents [ $\mu\text{A}$ ]			Frequencies [MHz]		
			$I_{DS,tar}$	$I_{DS,atm}$	$\Delta I_{DS}$	$f_{out,tar}$	$f_{out,atm}$	$\Delta f_{out}$
3	-7,30	-78,11	15,34	22,07	-6,73	372,88	427,63	-54,75
4	-4,25	-47,49	15,14	19,05	-3,91	370,72	403,74	-33,02
5	-4,09	-45,82	15,13	18,89	-3,76	370,59	402,62	-32,03
6	-3,59	-40,52	15,09	18,39	-3,30	370,48	398,93	-28,45
7	-3,64	-41,00	15,10	18,44	-3,34	370,49	399,26	-28,78
8	-4,65	-51,68	15,17	19,45	-4,28	372,47	407,75	-35,29
9	-3,32	-37,59	15,07	18,12	-3,04	370,30	396,86	-26,56
10	-3,03	-34,42	15,05	17,83	-2,77	370,10	394,53	-24,43

**Table 4.4:** Theoretical and simulation values of currents and frequencies, for exposure to NO (“O down”).

Since the currents and frequencies measured in the first and third phase differ slightly, the values of  $I_{DS,atm}$  and  $f_{out,atm}$  have been calculated considering the average of their respective values in the  $[0,25]$  and  $[50,75]$  ns time intervals. This approach allows to compute  $\Delta I_{DS}$  and  $\Delta f_{out}$  as the difference of the quantities before and after the gas target exposure. The same calculations can be done for the other configurations of the nitric oxide target, that can be compared to the same atmospheric gases as well. The Tables 4.5 and 4.6 report the results of the same type of simulations performed for the “N down” and “flat” orientations.

In spite of the mismatch between the values that refer to the analytic model and the ones obtained from the simulation, the behaviour of the output frequency is consistent with the modulation of the current that flows through the sensor. In particular, the least difference values of  $I_{DS}$  and  $f_{out}$  (respectively,  $0.84\ \mu\text{A}$  and  $6.68\ \text{MHz}$ ) refer to the sensing of a nitric oxide molecule with “N down” orientation

Exposure to NO (“N down”) - $V_{tar} = 19$ V								
$V_{atm}$ [V]	Theoretical values		Simulation values					
	$\Delta I_{DS}$ [ $\mu$ A]	$\Delta f_{out}$ [MHz]	Currents [ $\mu$ A]			Frequencies [MHz]		
			$I_{DS,tar}$	$I_{DS,atm}$	$\Delta I_{DS}$	$f_{out,tar}$	$f_{out,atm}$	$\Delta f_{out}$
3	-1,71	-16,83	20,56	22,11	-1,55	416,62	427,71	-11,09
4	1,34	13,79	20,27	19,07	1,20	414,20	404,73	9,47
5	1,50	15,46	20,26	18,91	1,35	414,00	403,45	10,55
6	2,00	20,76	20,20	18,41	1,79	413,89	399,65	14,24
7	1,96	20,28	20,21	18,46	1,75	413,97	400,05	13,92
8	0,94	9,60	20,31	19,47	0,84	414,61	407,93	6,68
9	2,27	23,69	20,18	18,14	2,03	413,67	397,33	16,34
10	2,57	26,86	20,14	17,85	2,29	413,43	394,77	18,66

**Table 4.5:** Theoretical and simulation values of currents and frequencies, for exposure to NO (“N down”).

Exposure to NO (“flat”) - $V_{tar} = 20$ V								
$V_{atm}$ [V]	Theoretical values		Simulation values					
	$\Delta I_{DS}$ [ $\mu$ A]	$\Delta f_{out}$ [MHz]	Currents [ $\mu$ A]			Frequencies [MHz]		
			$I_{DS,tar}$	$I_{DS,atm}$	$\Delta I_{DS}$	$f_{out,tar}$	$f_{out,atm}$	$\Delta f_{out}$
3	-7,39	-79,12	15,09	22,07	-6,98	370,51	427,52	-57,01
4	-4,34	-48,50	14,96	19,05	-4,09	369,02	403,89	-34,87
5	-4,18	-46,84	14,96	18,89	-3,94	368,93	402,73	-33,81
6	-3,68	-41,53	14,93	18,39	-3,46	368,93	399,04	-30,11
7	-3,72	-42,02	14,93	18,44	-3,50	368,93	399,37	-30,44
8	-4,74	-52,70	14,98	19,45	-4,47	371,14	407,74	-36,61
9	-3,41	-38,61	14,92	18,12	-3,20	368,82	396,92	-28,10
10	-3,11	-35,44	14,90	17,83	-2,92	368,68	394,56	-25,88

**Table 4.6:** Theoretical and simulation values of currents and frequencies, for exposure to NO (“flat”).

in presence of “H down” oriented water molecule. Instead, the maximum deviation in current and frequency ( $-6.98 \mu$ A and  $-57.01$  MHz) is obtained when the sensor detects a molecule of NO with “flat” orientation after a molecule of Ar.

The cited cases are coherent with the ideal values of  $\Delta I_{DS}$  and  $\Delta f_{out}$ , as well as the other ones. So, the correctness of the functionality of the analog front-end has been proved.

## 4.2 Exposure to nitrogen dioxide (NO<sub>2</sub>)

When the gas sensor is biased with a drain-source voltage in the [1.6,1.8] V interval, it is selective to the nitrogen dioxide (NO<sub>2</sub>). In order to have a good deviation of the current with respect to the exposure of atmospheric gases, the biasing voltage  $V_{DS}$  has been imposed equal to 1.7 V. In Table 4.7 the values of currents and frequencies for different orientation of the gas target are listed.

Gas target	$V_{CTRL}$ [V]	$I_{DS}$ [ $\mu$ A]	$f_{out}$ [MHz]
NO <sub>2</sub> (“O down”)	27	29.1865	368.5792
NO <sub>2</sub> (“N down”)	28	27.2808	353.0088
NO <sub>2</sub> (“flat”)	29	29.6154	371.9808

**Table 4.7:** Nitrogen dioxide (NO<sub>2</sub>): control voltages, input currents and output frequencies (for  $V_{DS} = 1.7$  V).

As for the case of nitric oxide, the exposure of the C<sub>60</sub>-based sensor to nitrogen dioxide is performed considering the “O down”, “N down” and “flat” orientations. In Figure 4.6 they are represented nearby the C<sub>60</sub>-sensor.

The considerations done in Section 4.1 about the approach in the simulation setup

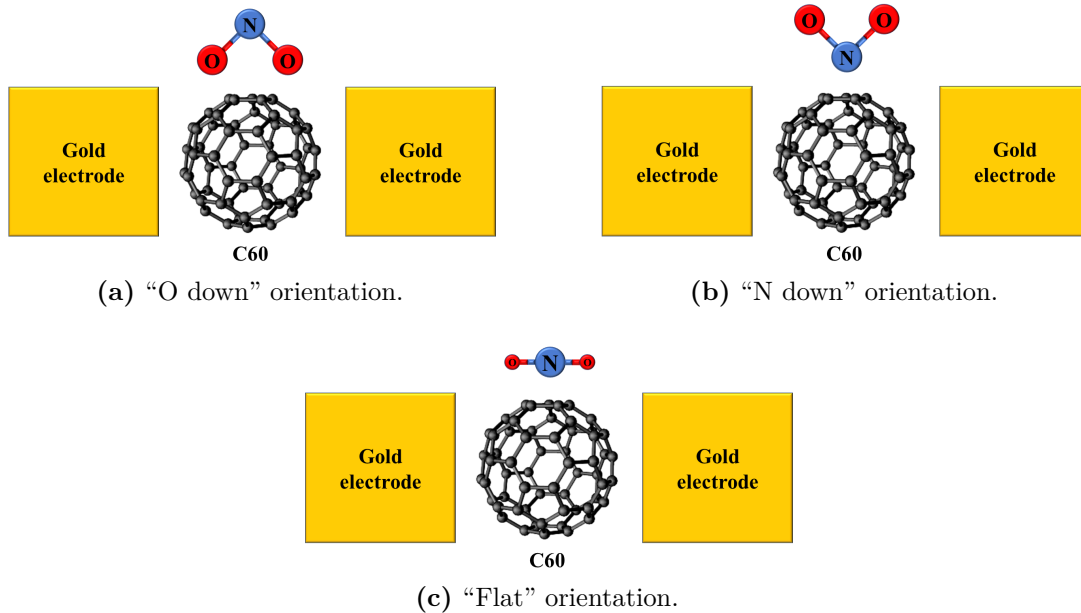


**Figure 4.6:** Orientations of nitrogen dioxide (NO<sub>2</sub>) with respect to C<sub>60</sub>-sensor’s channel axis.

are valid also in this case. The only parameter that is varied is the input voltage  $V_{REF}$ . It is fixed to 1.7 V in order to maximize the selectivity of the sensor to NO<sub>2</sub>, according to the characterization described in Subsection 2.2.3.

The values of current  $I_{DS}$  and frequency  $f_{out}$ , when the sensor is exposed first to the atmospheric gases molecules and then to the gas target in its different orientations, have been extracted. They have been reported in Tables 4.8, 4.9 and 4.10 where the theoretical values of the quantities of interest are listed to have a term of comparison.

Exposure to NO <sub>2</sub> (“O down”) - $V_{tar} = 27$ V								
$V_{atm}$ [V]	Theoretical values		Simulation values					
	$\Delta I_{DS}$ [ $\mu$ A]	$\Delta f_{out}$ [MHz]	Currents [ $\mu$ A]			Frequencies [MHz]		
			$I_{DS,tar}$	$I_{DS,atm}$	$\Delta I_{DS}$	$f_{out,tar}$	$f_{out,atm}$	$\Delta f_{out}$
3	-10,65	-74,85	29,34	39,83	-10,49	474,59	526,06	-51,47
4	-5,42	-40,47	39,57	38,48	1,09	459,57	470,43	-10,86
5	-2,05	-15,92	29,21	31,23	-2,01	473,39	484,48	-11,09
6	-5,16	-38,63	29,26	34,34	-5,08	474,34	500,58	-26,24
7	-1,54	-12,02	29,21	30,72	-1,51	473,32	481,69	-8,37
8	-2,37	-18,38	29,22	31,56	-2,34	473,51	486,24	-12,74
9	-2,50	-19,33	29,22	31,68	-2,46	473,56	486,90	-13,34
10	-4,30	-32,54	29,25	33,47	-4,22	473,61	495,69	-22,09

**Table 4.8:** Theoretical and simulation values of currents and frequencies, for exposure to NO<sub>2</sub> (“O down”).

The reported values are coherent with the expected behaviour of the analog front-end.

However, there can be observed an incongruity in the case of the exposure of NO<sub>2</sub> in presence of carbon oxide (CO). The extracted values of the currents, in particular  $I_{DS,tar}$ , differ significantly with respect to the values reported in Table 4.7. This causes an incorrect conversion in frequency which leads to a misleading recognition of the gas target with respect to the atmospheric gas which is compared to.

This incongruity may be caused by an inaccurate biasing of the sensor itself. Even though the input voltage is fixed at  $V_{REF} = 1.7$  V, the voltage  $V_{DS}$  across the sensor may be assume an unpredictable value for the case of NO<sub>2</sub> exposure and CO as atmospheric gas. Future works can correct this limitation in order to improve the coverage of the gas targets sensing, avoiding to run into wrong interpretations in the i-to-f conversion.

Exposure to NO <sub>2</sub> (“N down”) - V <sub>tar</sub> = 28 V								
V <sub>atm</sub> [V]	Theoretical values		Simulation values					
	$\Delta I_{DS}$ [ $\mu$ A]	$\Delta f_{out}$ [MHz]	Currents [ $\mu$ A]			Frequencies [MHz]		
			$I_{DS,tar}$	$I_{DS,atm}$	$\Delta I_{DS}$	$f_{out,tar}$	$f_{out,atm}$	$\Delta f_{out}$
3	-12,55	-90,42	27,53	39,82	-12,30	464,01	526,03	-62,02
4	-7,33	-56,04	35,22	39,46	-4,24	413,12	470,56	-57,45
5	-3,95	-31,49	27,35	31,23	-3,87	462,59	484,46	-21,87
6	-7,07	-54,20	27,42	34,33	-6,92	463,03	500,45	-37,43
7	-3,44	-27,59	27,34	30,71	-3,37	462,44	481,67	-19,22
8	-4,28	-33,95	27,36	31,55	-4,19	462,77	486,22	-23,45
9	-4,41	-34,90	27,36	31,67	-4,31	462,87	486,86	-23,99
10	-6,21	-48,11	27,40	33,46	-6,06	462,91	495,94	-33,03

**Table 4.9:** Theoretical and simulation values of currents and frequencies, for exposure to NO<sub>2</sub> (“N down”).

Exposure to NO <sub>2</sub> (“flat”) - V <sub>tar</sub> = 29 V								
V <sub>atm</sub> [V]	Theoretical values		Simulation values					
	$\Delta I_{DS}$ [ $\mu$ A]	$\Delta f_{out}$ [MHz]	Currents [ $\mu$ A]			Frequencies [MHz]		
			$I_{DS,tar}$	$I_{DS,atm}$	$\Delta I_{DS}$	$f_{out,tar}$	$f_{out,atm}$	$\Delta f_{out}$
3	-10,22	-71,45	29,89	39,83	-9,93	477,71	526,02	-48,31
4	-4,99	-37,06	36,07	39,46	-3,40	425,45	469,60	-44,15
5	-1,62	-12,52	29,66	31,23	-1,57	475,89	484,49	-8,59
6	-4,73	-35,23	29,75	34,34	-4,59	476,66	500,58	-23,92
7	-1,11	-8,62	29,64	30,72	-1,07	475,78	481,69	-5,91
8	-1,95	-14,98	29,67	31,56	-1,89	476,01	486,25	-10,24
9	-2,07	-15,93	29,67	31,68	-2,01	476,07	486,90	-10,83
10	-3,87	-29,14	29,72	33,47	-3,75	476,99	496,08	-19,09

**Table 4.10:** Theoretical and simulation values of currents and frequencies, for exposure to NO<sub>2</sub> (“flat”).

### 4.3 Sensitivity of the analog front-end

Once all the values of currents and frequencies have been acquired for all the cases of interest, the sensitivity of the implemented analog front-end can be extracted. The sensitivity is a parameter that expresses the expected variation of the output quantity (i.e. the frequency  $f_{out}$ ) with respect to an input quantity (like the current  $I_{DS}$  or the voltage  $V_{DS}$ ).

#### 4.3.1 Sensitivity with respect to $I_{DS}$

To have a reference for the sensitivity of the front-end that has been implemented in this thesis work, the couples of model values  $I_{DS}$  and  $f_{out}$  (listed in Tables 4.3 and 4.7) can be considered as points to interpolate with a straight curve. The angular coefficient of the curve represents the sensitivity that has to be obtained. In Figures 4.7 and 4.8 the extracted data and the interpolation curves for the cases of NO and NO<sub>2</sub> are shown.

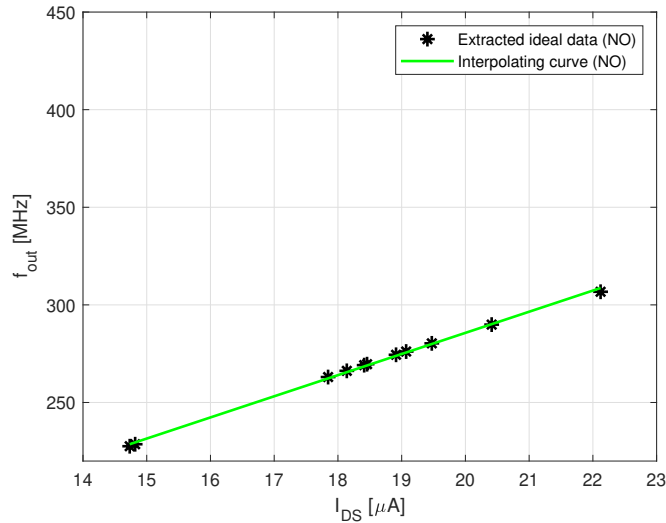


**Figure 4.7:** Interpolation of  $(I_{DS}, f_{out})$  ideal data, for NO exposure ( $V_{DS} = 1$  V).

The same approach can be adopted for the data acquired from the simulation of the analog front-end. In this case, the values of currents and frequencies that have to be used are the ones listed in Tables from 4.4 to 4.10. The simulation data and the interpolation straight lines are depicted in Figures 4.9 and 4.10.

As can be observed from Figure 4.10, there are six points that affect the interpolation. These  $(I_{DS}, f_{out})$  data are related to the exposure to CO as atmospheric gas. As mentioned in Section 4.1, this case represents an exception among the other

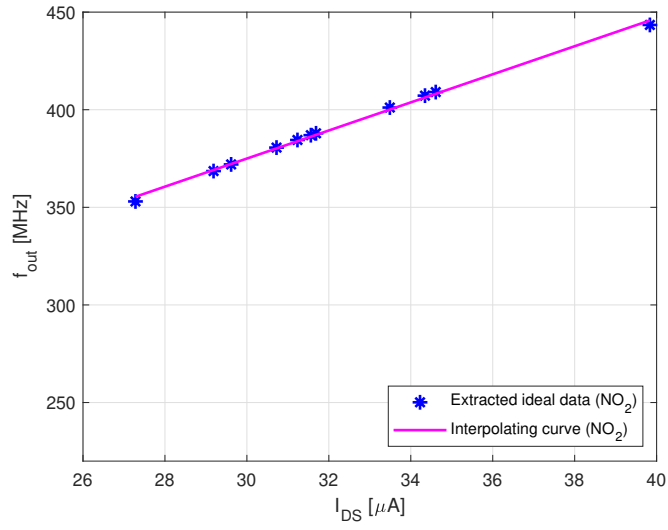


**Figure 4.8:** Interpolation of  $(I_{DS}, f_{out})$  ideal data, for  $\text{NO}_2$  exposure ( $V_{DS} = 1.7\text{ V}$ ).

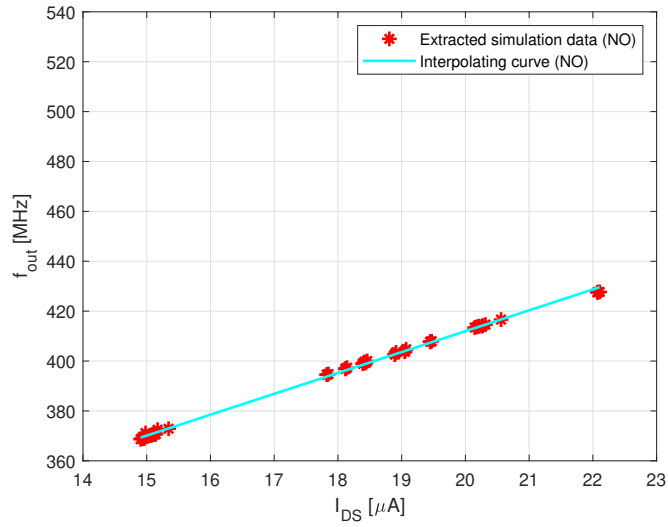


**Figure 4.9:** Interpolation of  $(I_{DS}, f_{out})$  data from simulation, for  $\text{NO}$  exposure ( $V_{REF} = 1\text{ V}$ ).

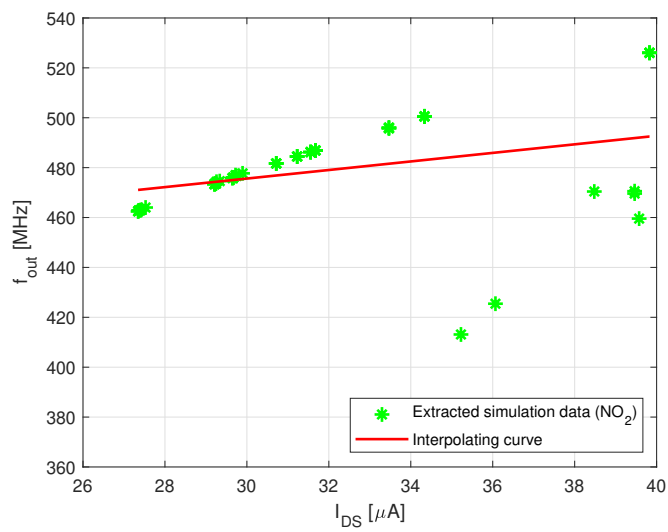


**Figure 4.10:** Interpolation of  $(I_{DS}, f_{out})$  data from simulation, for NO<sub>2</sub> exposure ( $V_{REF} = 1.7\text{ V}$ ).

combinations of targets. Then, these data can be excluded for this type of evaluation in order to have a correct interpolation, as in Figure 4.11.

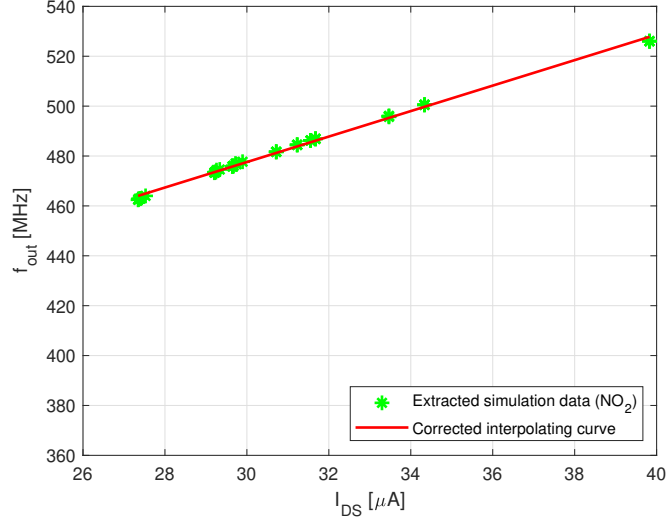


**Figure 4.11:** Corrected interpolation of  $(I_{DS}, f_{out})$  data from simulation, for  $\text{NO}_2$  exposure ( $V_{REF} = 1.7 \text{ V}$ ).

All the shown cases prove the linearity of the current-to-frequency conversion implemented by the analog front-end also in the simulation environment. The sensitivity of the analog front-end with respect to  $I_{DS}$  can be extracted considering the angular coefficients of the interpolating curves. The ideal and simulation values of this quantity are reported in Table 4.11.

Gas target	$V_{REF}$ [V]	Sensitivity with respect to $I_{DS}$ [MHz/ $\mu\text{A}$ ]	
		Ideal value	Simulation value
NO	1	10.8296	8.3693
$\text{NO}_2$	1.7	7.1935	5.1076

**Table 4.11:** Values of sensitivity of the analog front-end with respect to  $I_{DS}$ .

The extracted values of sensitivity show that when the sensor is exposed to NO the analog front-end provides higher frequencies than in the case of exposure to  $\text{NO}_2$ . Moreover, the numerical values of sensitivity in the simulation case result to be smaller than in ideal conditions. This is caused by the fact that the the analog front-end is affected by the tolerances of the components which is composed to (in particular, the MOSFETs). In order to have a precise conversion, design

improvements can be made in order to calibrate the sensitivity towards the ideal curve.

### 4.3.2 Sensitivity with respect to $V_{DS}$

As mentioned in Section 4.1, the voltage across the sensor  $V_{DS}$  is not exactly equal to the input reference voltage  $V_{REF}$ . In fact, it is affected by variations in time that cause undesired little modulations of current.

In order to evaluate the influence of the variation of  $V_{DS}$  on the output frequency, another sensitivity parameter can be extracted taking into account the values of  $V_{DS}$  corresponding to the values of frequency previously acquired.

The  $(V_{DS}, f_{out})$  data points and the curves that interpolate them are shown in Figures 4.12 and 4.13.

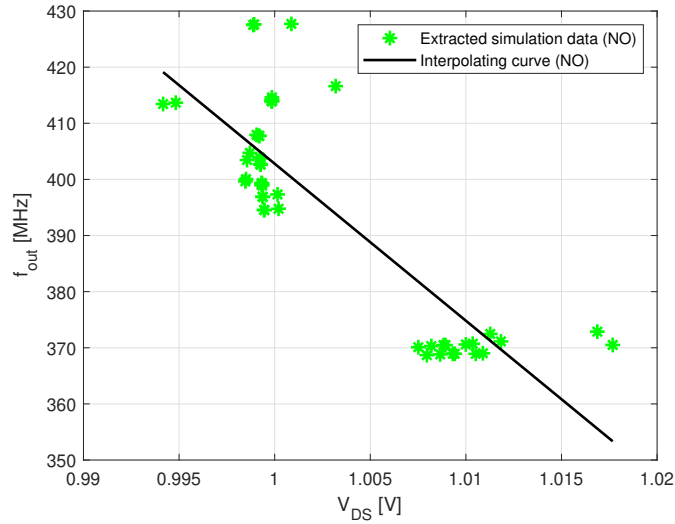


**Figure 4.12:** Interpolation of  $(V_{DS}, f_{out})$  data from simulation, for NO exposure ( $V_{REF} = 1$  V).

The obtained results show a “scattering” of the data points around the reference voltage ( $V_{REF} = 1$  V for NO and  $V_{REF} = 1.7$  V for NO<sub>2</sub>). For this reason, the interpolation of the data is not accurate. Nevertheless, as first approximation, it provides an indication about the modulation of the output frequency due to the variation of the voltage across the sensor.

In fact, according to the detected targets, the voltage  $V_{DS}$  deviates from the value of  $V_{REF}$ . This variation turns into a modulation of the current  $I_{DS}$  and consequently of the frequency  $f_{out}$ .

As well as in the previous subsection, the sensitivity with respect to  $V_{DS}$  is equal to the slope of the interpolating curves and its values for the analyzed gas exposures

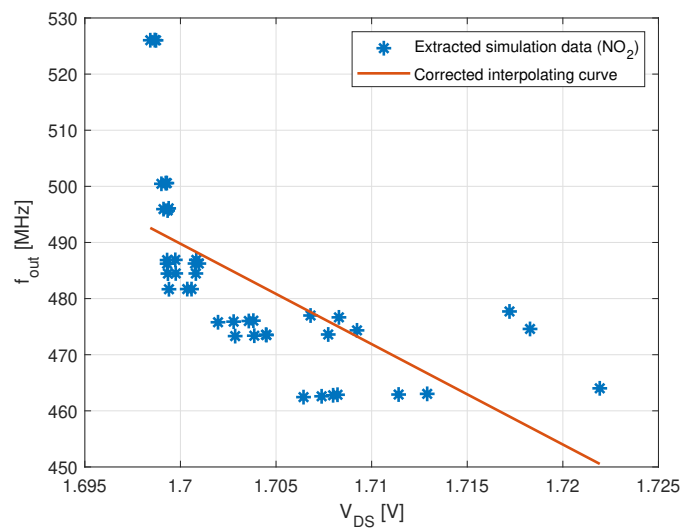


**Figure 4.13:** Interpolation of  $(V_{DS}, f_{out})$  data from simulation, for  $\text{NO}_2$  exposure ( $V_{REF} = 1.7 \text{ V}$ ).

are reported in Table 4.12.

Gas target	$V_{REF}$ [V]	Sensitivity with respect to $V_{DS}$ [MHz/mV]
NO	1	-2.7974
NO <sub>2</sub>	1.7	-1.7888

**Table 4.12:** Values of sensitivity of the analog front-end with respect to  $V_{DS}$ .

The meaning of these results is that for little variations of the voltage across the sensor (in the order of mV), the modulation of frequency is noticeable. Then, the C<sub>60</sub>-based sensor requires to be biased with very high accuracy to avoid a misleading current-to-frequency conversion that, in turn, might cause an erroneous recognition of the gas targets.



## Chapter 5

# Conclusions and future works

The characterization and the design of an analog front-end for a molecular gas sensor, based on  $C_{60}$  fullerene, has been presented in this thesis work. After a recall to the functioning principle and the analytic model of the molecular gas-sensor (fully described in [57]), some requirements useful for the design have been exploited to set up the implementation of the circuit on Cadence Virtuoso.

The main blocks of the front-end - i.e. the readout circuit and the current-to-frequency converter - have been implemented and simulated separately in order to validate their own behaviour.

Afterwards, they have been joined together to simulate the whole circuit and to verify the correctness of its functioning.

This thesis work is the first attempt in sketching a hardware solution for the integration of this device in molecular technology and a CMOS interfacing circuit. The results obtained in the final chapter have proved the respect of the requirements extracted starting from the features of the sensor. In particular, the linear relation between the current flowing through the sensor and the output frequency has been confirmed, in conformity to the presented mathematical model.

The proposed circuit permits the reliable detection of NO and  $NO_2$  in presence of common atmospheric gases. Decreased reliability occurs only in two cases over six (namely for NO with “N down” approaching orientation and for  $NO_2$  with “flat” approaching orientation), for which the frequency sensitivity to small current variations (produced by chemical competitors or noise) leads to only few MHz of margins.

Considerations on drawbacks of the proposed solution can be exploited as starting points for future works and developments. Firstly, the timescale used in this thesis work takes into account the response time of the MOSFETs that are involved in

the circuit, which is in the order of nanoseconds. Since the sensor is able to detect single molecules at room temperature, it is supposed to sense them very fast, with shorter time orders of magnitude. Then, an improvement of MOSFETs from a technological point of view (with respect to geometrical and electrical parameters) is needed to align with the time response of molecular devices as the one analyzed. Architectural changes and ameliorations can be also thought.

Another point is about the performances of the analog front-end in terms of accuracy of the biasing and the successive conversion. The optimization of design choices, along with an improvement of the Verilog models of functional blocks, may enhance the effectiveness of the circuit. An indication of this can be provided by the sensitivity with respect to the current that should be calibrated towards the one obtained in the ideal case.

At the end, the proposed solution may be considered as a basic architecture useful for more complex implementations. As an example, for the detection of more molecules, a large number of molecular sensors can be employed. Then, the working principle of the front-end implemented in this thesis can be exploited to obtain not only the recognition of the gas target. It may be able to extract some information about its concentration in the environment, also at low values.



# Bibliography

- [1] R. K. Pachauri et al. *Climate Change 2014: Synthesis Report. Contribution of Working Groups I, II and III to the Fifth Assessment Report of the Intergovernmental Panel on Climate Change*. Ed. by R.K. Pachauri and L. Meyer. Geneva, Switzerland: IPCC, 2014, p. 151 (cit. on p. 1).
- [2] Noboru Yamazoe. «Toward innovations of gas sensor technology». In: *Sensors and Actuators B: Chemical* 108.1 (2005). Proceedings of the Tenth International Meeting on Chemical Sensors, pp. 2–14. ISSN: 0925-4005. DOI: <https://doi.org/10.1016/j.snb.2004.12.075>. URL: <https://www.sciencedirect.com/science/article/pii/S0925400505000286> (cit. on pp. 1–3).
- [3] Gordon E Moore et al. *Cramming more components onto integrated circuits*. 1965 (cit. on pp. 2, 19).
- [4] Yizhe Liu. «Advantages of CMOS Technology in Very Large Scale Integrated Circuits». In: *2021 2nd International Conference on Artificial Intelligence in Electronics Engineering*. 2021, pp. 82–88 (cit. on p. 2).
- [5] *International Technology Roadmap for Semiconductors 2.0: 2015*. URL: <http://www.itrs2.net/itrs-reports.html> (cit. on pp. 2, 19).
- [6] *International Roadmap for Devices and Semiconductors: 2021 Edition*. URL: <https://irds.ieee.org/editions/2021> (cit. on pp. 2, 19, 20).
- [7] Julian W. Gardner, Prasanta K. Guha, Florin Udrea, and James A. Covington. «CMOS Interfacing for Integrated Gas Sensors: A Review». In: *IEEE Sensors Journal* 10.12 (2010), pp. 1833–1848. DOI: 10.1109/JSEN.2010.2046409 (cit. on pp. 2, 5, 6, 8).
- [8] Shahid Naveed and Zeeshan Nawaz. *Advances in Chemical Engineering*. eng. IntechOpen, 2012. ISBN: 9789535161745 (cit. on p. 3).
- [9] Dinesh K Aswal and Shiv K Gupta. *Science and Technology of Chemiresistor Gas Sensors*. eng. Hauppauge: Nova Science Publishers, Incorporated, 2007. ISBN: 1600215149 (cit. on p. 4).

- [10] Hyo-Joong Kim and Jong-Heun Lee. «Highly sensitive and selective gas sensors using p-type oxide semiconductors: Overview». In: *Sensors and Actuators B: Chemical* 192 (2014), pp. 607–627 (cit. on p. 4).
- [11] Noboru Yamazoe and Kengo Shimano. «Theory of power laws for semiconductor gas sensors». In: *Sensors and Actuators B: Chemical* 128.2 (2008), pp. 566–573 (cit. on p. 4).
- [12] Maria Vesna Nikolic. «An Overview of Oxide Materials for Gas Sensors». In: *2020 23rd International Symposium on Design and Diagnostics of Electronic Circuits & Systems (DDECS)*. 2020, pp. 1–4. DOI: 10.1109/DDECS50862.2020.9095743 (cit. on p. 4).
- [13] J Lančok, A Santoni, M Penza, S Loreti, I Menicucci, C Minarini, and M Jelinek. «Tin oxide thin films prepared by laser-assisted metal–organic CVD: Structural and gas sensing properties». In: *Surface and Coatings Technology* 200.1-4 (2005), pp. 1057–1060 (cit. on p. 5).
- [14] Seok-Kyun Song, Jun-Sik Cho, Won-Kook Choi, Hyung-Jin Jung, Dongsoo Choi, Jeong-Yong Lee, Hong-Koo Baik, and Seok-Keun Koh. «Structure and gas-sensing characteristics of undoped tin oxide thin films fabricated by ion-assisted deposition». In: *Sensors and Actuators B: Chemical* 46.1 (1998), pp. 42–49 (cit. on p. 5).
- [15] Sung-Soon Park and JD Mackenzie. «Thickness and microstructure effects on alcohol sensing of tin oxide thin films». In: *Thin Solid Films* 274.1-2 (1996), pp. 154–159 (cit. on p. 5).
- [16] A. Cruccolini, R. Narducci, and R. Palombari. «Gas adsorption effects on surface conductivity of nonstoichiometric CuO». In: *Sensors and Actuators B: Chemical* 98.2 (2004), pp. 227–232. ISSN: 0925-4005. DOI: <https://doi.org/10.1016/j.snb.2003.10.012>. URL: <https://www.sciencedirect.com/science/article/pii/S0925400503007809> (cit. on p. 5).
- [17] Jinhui Liu, Xingjiu Huang, Gang Ye, Wei Liu, Zheng Jiao, Wnaglian Chao, Zhongbai Zhou, and Zenglian Yu. «H<sub>2</sub>S Detection Sensing Characteristic of CuO/SnO<sub>2</sub> Sensor». In: *Sensors* 3.5 (2003), pp. 110–118. ISSN: 1424-8220. DOI: 10.3390/s30500110. URL: <https://www.mdpi.com/1424-8220/3/5/110> (cit. on p. 5).
- [18] Tetsuro Seiyama, Akio Kato, Kiyoshi Fujiishi, and Masanori Nagatani. «A new detector for gaseous components using semiconductive thin films.» In: *Analytical Chemistry* 34.11 (1962), pp. 1502–1503 (cit. on p. 5).

- [19] L.F. Dong, Z.L. Cui, and Z.K. Zhang. «Gas sensing properties of nano-ZnO prepared by arc plasma method». In: *Nanostructured Materials* 8.7 (1997), pp. 815–823. ISSN: 0965-9773. DOI: [https://doi.org/10.1016/S0965-9773\(98\)00005-1](https://doi.org/10.1016/S0965-9773(98)00005-1). URL: <https://www.sciencedirect.com/science/article/pii/S0965977398000051> (cit. on p. 5).
- [20] Caihong Wang, Xiangfeng Chu, and Mingmei Wu. «Detection of H<sub>2</sub>S down to ppb levels at room temperature using sensors based on ZnO nanorods». In: *Sensors and Actuators B: Chemical* 113.1 (2006), pp. 320–323. ISSN: 0925-4005. DOI: <https://doi.org/10.1016/j.snb.2005.03.011>. URL: <https://www.sciencedirect.com/science/article/pii/S0925400505002790> (cit. on p. 5).
- [21] Joseph R Stetter, William R Penrose, and Sheng Yao. «Sensors, chemical sensors, electrochemical sensors, and ECS». In: *Journal of The Electrochemical Society* 150.2 (2003), S11 (cit. on p. 6).
- [22] *Electrolyte*. URL: <https://www.britannica.com/science/electrolyte> (cit. on p. 6).
- [23] Jeffrey W Fergus. «Materials for high temperature electrochemical NO<sub>x</sub> gas sensors». In: *Sensors and Actuators B: Chemical* 121.2 (2007), pp. 652–663 (cit. on p. 6).
- [24] Piotr Jasiński. «Solid-state electrochemical gas sensors». In: *Materials Science-Poland* 24.1 (2006), pp. 269–278 (cit. on p. 6).
- [25] W.C Maskell and J.A Page. «Detection of water vapour or carbon dioxide using a zirconia pump-gauge sensor». In: *Sensors and Actuators B: Chemical* 57.1 (1999), pp. 99–107. ISSN: 0925-4005. DOI: [https://doi.org/10.1016/S0925-4005\(99\)00139-2](https://doi.org/10.1016/S0925-4005(99)00139-2). URL: <https://www.sciencedirect.com/science/article/pii/S0925400599001392> (cit. on p. 6).
- [26] Duk-Dong Lee and Dae-Sik Lee. «Environmental gas sensors». In: *IEEE sensors journal* 1.3 (2001), pp. 214–224 (cit. on p. 6).
- [27] Sandro Carrara. *Bio/CMOS interfaces and co-design*. eng. New York: Springer, 2013. ISBN: 978-1-4614-4689-7 (cit. on p. 7).
- [28] Joseph R. Stetter and Jing Li. «Amperometric Gas Sensors: A Review». In: *Chemical Reviews* 108.2 (2008). PMID: 18201108, pp. 352–366. DOI: 10.1021/cr0681039. eprint: <https://doi.org/10.1021/cr0681039>. URL: <https://doi.org/10.1021/cr0681039> (cit. on p. 7).
- [29] *Reversible electrode*. URL: <https://www.merriam-webster.com/dictionary/reversible%5C%20electrode> (cit. on p. 7).

- [30] Cristian V. Diaconu, Keith Pratt, Mihai Gologanu, Cazimir G. Bostan, and Martin Willett. «An Electrochemical Oxygen Pump Model – A Tool for Sensor Optimization». In: *Procedia Engineering* 87 (2014). EUROSENSORS 2014, the 28th European Conference on Solid-State Transducers, pp. 1605–1608. ISSN: 1877-7058. DOI: <https://doi.org/10.1016/j.proeng.2014.11.730>. URL: <https://www.sciencedirect.com/science/article/pii/S1877705814028525> (cit. on p. 7).
- [31] Xiaoyi Mu, Zhe Wang, Xiangqun Zeng, and Andrew Mason. «A Robust Flexible Electrochemical Gas Sensor Using Room Temperature Ionic Liquid». In: *Sensors Journal, IEEE* 13 (Oct. 2013), pp. 3976–3981. DOI: 10.1109/JSEN.2013.2262932 (cit. on p. 7).
- [32] Hao Wan, Heyu Yin, and Andrew J. Mason. «Rapid measurement of room temperature ionic liquid electrochemical gas sensor using transient double potential amperometry». In: *Sensors and Actuators B: Chemical* 242 (2017), pp. 658–666. ISSN: 0925-4005. DOI: <https://doi.org/10.1016/j.snb.2016.11.103>. URL: <https://www.sciencedirect.com/science/article/pii/S0925400516319013> (cit. on p. 7).
- [33] Zhe Wang, Peiling Lin, Gary A. Baker, Joseph Stetter, and Xiangqun Zeng. «Ionic Liquids as Electrolytes for the Development of a Robust Amperometric Oxygen Sensor». In: *Analytical Chemistry* 83.18 (2011). PMID: 21848335, pp. 7066–7073. DOI: 10.1021/ac201235w. eprint: <https://doi.org/10.1021/ac201235w>. URL: <https://doi.org/10.1021/ac201235w> (cit. on p. 7).
- [34] Wei Onn Ting and Sara S. Ghoreishizadeh. «Autonomous readout ASIC with 169dB input dynamic range for amperometric measurement». In: *2018 25th IEEE International Conference on Electronics, Circuits and Systems (ICECS)*. Dec. 2018, pp. 869–872. DOI: 10.1109/ICECS.2018.8617875 (cit. on pp. 8, 9, 13).
- [35] *What is a Potentiostat and how does it work?* URL: <https://pineresearch.com/shop/kb/theory/instrumentation/what-potentiostat-does/> (cit. on p. 9).
- [36] Meisam Honarvar Nazari, Hamed Mazhab-Jafari, Lian Leng, Axel Guenther, and Roman Genov. «CMOS Neurotransmitter Microarray: 96-Channel Integrated Potentiostat With On-Die Microsensors». In: *IEEE Transactions on Biomedical Circuits and Systems* 7.3 (June 2013), pp. 338–348. ISSN: 1940-9990. DOI: 10.1109/TBCAS.2012.2203597 (cit. on pp. 9, 10, 13).

- [37] Haitao Li, C. Sam Boling, and Andrew J. Mason. «CMOS Amperometric ADC With High Sensitivity, Dynamic Range and Power Efficiency for Air Quality Monitoring». In: *IEEE Transactions on Biomedical Circuits and Systems* 10.4 (Aug. 2016), pp. 817–827. ISSN: 1940-9990. DOI: 10.1109/TBCAS.2016.2571306 (cit. on pp. 10, 11, 13).
- [38] Marco Crescentini, Marco Bennati, Marco Carminati, and Marco Tartagni. «Noise Limits of CMOS Current Interfaces for Biosensors: A Review». In: *IEEE Transactions on Biomedical Circuits and Systems* 8.2 (Apr. 2014), pp. 278–292. ISSN: 1940-9990. DOI: 10.1109/TBCAS.2013.2262998 (cit. on p. 11).
- [39] Milutin Stanacevic, Kartikeya Murari, Abhishek Rege, Gert Cauwenberghs, and Nitish V. Thakor. «VLSI Potentiostat Array With Oversampling Gain Modulation for Wide-Range Neurotransmitter Sensing». In: *IEEE Transactions on Biomedical Circuits and Systems* 1.1 (Mar. 2007), pp. 63–72. ISSN: 1940-9990. DOI: 10.1109/TBCAS.2007.893176 (cit. on pp. 11, 13).
- [40] Da Ying, Ping-Wei Chen, Chi Tseng, Yu-Hwa Lo, and Drew A. Hall. «A Sub-pA Current Sensing Front-End for Transient Induced Molecular Spectroscopy». In: *2019 Symposium on VLSI Circuits*. June 2019, pp. C316–C317. DOI: 10.23919/VLSIC.2019.8777980 (cit. on pp. 12, 13).
- [41] Sara S. Ghoreishizadeh, Irene Taurino, Giovanni De Micheli, Sandro Carrara, and Pantelis Georgiou. «A Differential Electrochemical Readout ASIC With Heterogeneous Integration of Bio-Nano Sensors for Amperometric Sensing». In: *IEEE Transactions on Biomedical Circuits and Systems* 11.5 (Oct. 2017), pp. 1148–1159. ISSN: 1940-9990. DOI: 10.1109/TBCAS.2017.2733624 (cit. on p. 12).
- [42] Kwan Ting Ng, Farid Boussaid, and Amine Bermak. «A frequency-based signature gas identification circuit for SnO<sub>2</sub> gas sensors». In: *Proceedings of 2010 IEEE International Symposium on Circuits and Systems*. May 2010, pp. 2275–2278. DOI: 10.1109/ISCAS.2010.5536952 (cit. on pp. 14–16, 48, 51).
- [43] Bin Guo, Amine Bermak, Maxime Ambard, and Dominique Martinez. «A  $4 \times 4$  Logarithmic Spike Timing Encoding Scheme for Olfactory Sensor Applications». In: *2007 IEEE International Symposium on Circuits and Systems*. May 2007, pp. 3554–3557. DOI: 10.1109/ISCAS.2007.378450 (cit. on pp. 15–17, 48, 51).
- [44] Kwan Ting Ng, Bin Guo, Amine Bermak, Dominique Martinez, and Farid Boussaid. «Characterization of a logarithmic spike timing encoding scheme for a  $4 \times 4$  tin oxide gas sensor array». In: *SENSORS, 2009 IEEE*. Oct. 2009,

- pp. 731–734. DOI: 10.1109/ICSENS.2009.5398548 (cit. on pp. 15–17, 48, 51).
- [45] Kwan Ting Ng, Farid Boussaid, and Amine Bermak. «A CMOS Single-Chip Gas Recognition Circuit for Metal Oxide Gas Sensor Arrays». In: *IEEE Transactions on Circuits and Systems I: Regular Papers* 58.7 (July 2011), pp. 1569–1580. ISSN: 1558-0806. DOI: 10.1109/TCSI.2011.2143090 (cit. on pp. 16, 17, 48, 51).
- [46] D. J. Frank. «Power-constrained CMOS scaling limits». In: *IBM Journal of Research and Development* 46.2.3 (Mar. 2002), pp. 235–244. ISSN: 0018-8646. DOI: 10.1147/rd.462.0235 (cit. on pp. 19, 44).
- [47] James M. Tour. «Molecular Electronics. Synthesis and Testing of Components». In: *Accounts of Chemical Research* 33.11 (2000). PMID: 11087316, pp. 791–804. DOI: 10.1021/ar0000612. eprint: <https://doi.org/10.1021/ar0000612>. URL: <https://doi.org/10.1021/ar0000612> (cit. on p. 20).
- [48] Wenwen Hu et al. «Electronic Noses: From Advanced Materials to Sensors Aided with Data Processing». In: *Advanced Materials Technologies* 4.2 (2019), p. 1800488. DOI: <https://doi.org/10.1002/admt.201800488>. eprint: <https://onlinelibrary.wiley.com/doi/pdf/10.1002/admt.201800488>. URL: <https://onlinelibrary.wiley.com/doi/abs/10.1002/admt.201800488> (cit. on p. 21).
- [49] Sang-Joon Kim, Seon-Jin Choi, Ji-Soo Jang, Hee-Jin Cho, and Il-Doo Kim. «Innovative Nanosensor for Disease Diagnosis». In: *Accounts of Chemical Research* 50.7 (2017). PMID: 28481075, pp. 1587–1596. DOI: 10.1021/acs.accounts.7b00047. eprint: <https://doi.org/10.1021/acs.accounts.7b00047>. URL: <https://doi.org/10.1021/acs.accounts.7b00047> (cit. on p. 21).
- [50] Paven Thomas Mathew and Fengzhou Fang. «Advances in Molecular Electronics: A Brief Review». In: *Engineering* 4.6 (2018), pp. 760–771. ISSN: 2095-8099. DOI: <https://doi.org/10.1016/j.eng.2018.11.001>. URL: <https://www.sciencedirect.com/science/article/pii/S2095809918306453> (cit. on p. 21).
- [51] A. Zahir, S. A. A. Zaidi, A. Pulimeno, M. Graziano, D. Demarchi, G. Masera, and G. Piccinini. «Molecular transistor circuits: From device model to circuit simulation». In: *2014 IEEE/ACM International Symposium on Nanoscale Architectures (NANOARCH)*. July 2014, pp. 129–134. DOI: 10.1109/NANOARCH.2014.6880492 (cit. on p. 22).

- [52] Louis C. Brousseau. «Label-Free “Digital Detection” of Single-Molecule DNA Hybridization with a Single Electron Transistor». In: *Journal of the American Chemical Society* 128.35 (2006). PMID: 16939245, pp. 11346–11347. DOI: 10.1021/ja063022f. eprint: <https://doi.org/10.1021/ja063022f>. URL: <https://doi.org/10.1021/ja063022f> (cit. on p. 22).
- [53] Savannah Afsahi et al. «Novel graphene-based biosensor for early detection of Zika virus infection». In: *Biosensors and Bioelectronics* 100 (2018), pp. 85–88. ISSN: 0956-5663. DOI: <https://doi.org/10.1016/j.bios.2017.08.051>. URL: <https://www.sciencedirect.com/science/article/pii/S0956566317305869> (cit. on p. 22).
- [54] Giwan Seo et al. «Rapid Detection of COVID-19 Causative Virus (SARS-CoV-2) in Human Nasopharyngeal Swab Specimens Using Field-Effect Transistor-Based Biosensor». In: *ACS Nano* 14.4 (2020). PMID: 32293168, pp. 5135–5142. DOI: 10.1021/acsnano.0c02823. eprint: <https://doi.org/10.1021/acsnano.0c02823>. URL: <https://doi.org/10.1021/acsnano.0c02823> (cit. on p. 22).
- [55] Soumya Ray. «Humidity sensor using a single molecular transistor». In: *Journal of Applied Physics* 118 (July 2015). DOI: 10.1063/1.4927296 (cit. on p. 22).
- [56] J. Justin Gooding and Katharina Gaus. «Single-Molecule Sensors: Challenges and Opportunities for Quantitative Analysis». In: *Angewandte Chemie International Edition* 55.38 (2016), pp. 11354–11366. DOI: <https://doi.org/10.1002/anie.201600495>. eprint: <https://onlinelibrary.wiley.com/doi/pdf/10.1002/anie.201600495>. URL: <https://onlinelibrary.wiley.com/doi/abs/10.1002/anie.201600495> (cit. on p. 22).
- [57] Fabrizio Mo, Yuri Ardesi, Massimo Ruo Roch, Mariagrazia Graziano, and Gianluca Piccinini. «Investigation of Amperometric Sensing Mechanism in Gold–C60–Gold Molecular Dot». In: *IEEE Sensors Journal* 22.20 (Oct. 2022), pp. 19152–19161. ISSN: 1558-1748. DOI: 10.1109/JSEN.2022.3203513 (cit. on pp. 22, 23, 26–30, 38, 63, 82).
- [58] Abdelghaffar Nasri, Aimen Boubaker, Bilel Hafsi, Wassim Khaldi, and Adel Kalboussi. «High-Sensitivity Sensor Using C60-Single Molecule Transistor». In: *IEEE Sensors Journal* 18.1 (Jan. 2018), pp. 248–254. ISSN: 1558-1748. DOI: 10.1109/JSEN.2017.2769803 (cit. on p. 23).
- [59] Simon M Sze. *Semiconductor Devices: Physics and Technology* / Simon Sze, Ming-Kwei Lee. eng. 3rd ed. Hoboken (New Jersey): Wiley, 2013. ISBN: 9780470537947 (cit. on p. 23).
- [60] Supriyo Datta. *Quantum transport: atom to transistor*. Cambridge university press, 2005 (cit. on p. 23).

- [61] Marc Baldo. *Introduction to Nanoelectronics*. MIT OpenCourseWare, 2011 (cit. on p. 26).
- [62] Fabrizio Mo, Chiara Elfi Spano, Yuri Ardesi, Gianluca Piccinini, and Maria-grazia Graziano. «Beyond-CMOS Artificial Neuron: A Simulation- Based Exploration of the Molecular-FET». In: *IEEE Transactions on Nanotechnology* 20 (2021), pp. 903–911. DOI: 10.1109/TNANO.2021.3133728 (cit. on p. 26).
- [63] *How accurate is your low current measurement?* URL: <https://www.qoitech.com/blog/how-accurate-is-your-current-measurement> (cit. on p. 34).
- [64] Behzad Razavi. *Design of analog CMOS integrated circuits / Behzad Razavi*. eng. 2nd ed. New York: McGraw-Hill Education, 2017. ISBN: 9781259255090 (cit. on p. 41).
- [65] Shagun Bajoria. «Precision Current Mirror». PhD thesis. Texas Instruments, 2010 (cit. on p. 41).
- [66] Vivek Pant and Shweta Khurana. «Optimal high performance self cascode cmos current mirror». In: *Global Journal of Computer Science and Technology* 11.15 (2011) (cit. on pp. 41, 42).
- [67] DK Shedge, DA Itole, SB Dhonde, PW Wani, and MS Sutaone. «Comparison of CMOS Current Mirror Sources». In: *International Journal on Recent Trends in Engineering & Technology* 8.2 (2013), p. 73 (cit. on p. 41).
- [68] Simon Baumann, Timo Lausen, and Roland Thewes. «Homogeneity Enhancement of Current-to-Frequency-Converters Operated in Sensor Array Applications». In: *2019 IEEE International Symposium on Circuits and Systems (ISCAS)*. IEEE. 2019, pp. 1–4 (cit. on p. 51).